Diffuse Radio Emission in a Galaxy Cluster Merger at frequency ranging from 150 MHz to 18 GHz

Ph.D. Thesis

By

PRITPAL KAUR SANDHU

DISCIPLINE OF PHYSICS

INDIAN INSTITUTE OF TECHNOLOGY INDORE

July, 2018

Diffuse Radio Emission in a Galaxy Cluster Merger at frequency ranging from 150 MHz to 18 GHz

A THESIS

Submitted in partial fulfillment of the requirements for the award of the degree

of

DOCTOR OF PHILOSOPHY

by

PRITPAL KAUR SANDHU

DISCIPLINE OF PHYSICS

INDIAN INSTITUTE OF TECHNOLOGY INDORE

JULY 2018

INDIAN INSTITUTE OF TECHNOLOGY INDORE

CANDIDATE'S DECLARATION

I hereby certify that the work which is being presented in the thesis entitled **Diffuse Radio Emission in a Galaxy Cluster Merger at frequency ranging from 150 MHz to 18 GHz** in the partial fulfillment of the requirements for the award of the degree of **DOCTOR OF PHILOSOPHY** and submitted in the **DISCIPLINE OF PHYSICS, Indian Institute of Technology Indore**, is an authentic record of my own work carried out during the time period from July 2012 to July 2018 under the supervision of **Dr. Abhirup Datta.**

The matter presented in this thesis has not been submitted by me for the award of any other degree of this or any other institute.

Signature of the student with date
Pritpal Kaur Sandhu

This is to certify that the above statement made by the candidate is correct to the best of my/our knowledge.

Signature of Thesis Supervisor with date

Dr. Abhirup Datta

Pritpal Kaur Sandhu has successfully given his/her Ph.D. Oral Examination held on

Signature of Chairperson (OEB)
Date:

Signature of External Examiner
Date:

Signature(s) of Thesis Supervisor(s)
Date:

Signature of PSPC Member #1
Date:

Signature of PSPC Member #2
Date:

Signature of Convener, DPGC
Date:

Signature of Head of Discipline
Date:

ACKNOWLEDGEMENTS

I would like to extend thanks to the many people, who so generously contributed to the work presented in this thesis.

I would like to express my special appreciation and thanks to my advisor Dr. Abhirup Datta, you have been a tremendous mentor for me. Your advice on both research as well as on my career have been priceless. I would like to thank Dr. Siddharth Malu for contribution in research and publications. I would also like to thank my committee members, Prof. S. Rakshit and Dr. Ram Bilas Pachori for serving as my committee members even at hardship.

The support provided by the administration, the computer section, the library, the hostel and the mess at IIT Indore has been excellent and I am thankful to them.

All of my friends who supported me in writing and encouraged me to strive towards my goal: thank you all!

Finally, but by no means least, thanks to my parents, brother, husband and maternal family for almost unbelievable support. They are the most important people in the world and I dedicate this thesis to them.

DEDICATION

To my parents

and

husband

SYNOPSIS

1. INTRODUCTION

Galaxies, including our own Milky Way Galaxy, are vast assemblies of stars and gas. Clusters of galaxies consist of tens to hundreds of galaxies and are the largest gravitationally bound structures in the universe. They are ideal laboratories to study the formation and evolution of cosmic structure. Zwicky was the first to examine the Coma galaxy cluster in 1933, by using the virial theorem to infer the existence of unseen matter, which he referred to as *Dunkle Materie* 'dark matter'.

Galaxy clusters have become an important cosmological tool in the last two decades for studying the accelerated expansion of the universe caused by dark energy. Recently, we have learned that these clusters show the peculiar characterstics i.e. they are not as simple as they appear. We now know that galaxy cluster mergers are the most energetic events in the universe and that these clusters frequently collided in the early universe. Most clusters are really the result of 'cluster mergers', which are collisions between galaxy clusters. These collisions have major impact on the structure and evolution of the clusters and the cosmological conclusions we draw from observing them. The goal of the research program proposed here is to observe a two of these cluster mergers at several different frequencies.

According to 2dF galaxy redshift surveys (Peacock et al 2001), clusters of galaxies are formed in the large-scale filamentary structure of the Universe at the present epoch.A slice of the Millennium Simulation (Springel et al 2005) is shown in Fig. 1.1 (left). It is a visual impression of the distribution of the dark matter on large scales in the Universe at the present epoch. A cluster of galaxies formed at the intersection of the filaments is shown in Fig. 1.1 (right).

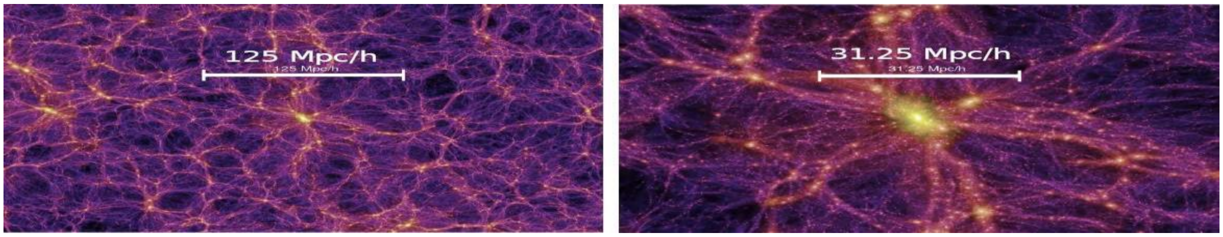

Figure 1: (Left)Visual impression of the dark matter structure on large scales at the present time as shown by the Millennium Simulation. (Right) A closer view of a galaxy cluster formed at the intersection of filaments. (Images: VIRGO consortium)

2. OBJECTIVES OF THIS THESIS

This thesis is a presentation of a multifrequency analysis of two galaxy clusters known to be experiencing merger events. Diffuse non-thermal radio emission in clusters of galaxies of ~Mpc size not associated with galaxies, when close to the centres of clusters, are called radio halos, and when at or close to the peripheries of clusters are called radio relics. These are due to relativistic electrons and magnetic fields in the ICM and have steep synchrotron spectra. Also,we use Newtonian formalism to motivate the form of Friedmann equations that describe the expansion of the universe in the standard cosmological model. We use the same formalism to study the evolution of density perturbations in the universe. We show that a simple model like spherical collapse can be used to estimate the characteristics of halos of galaxies and clusters of galaxies.

RADIO HALOS AND RELICS

Radio halos are diffuse radio sources of low surface brightness(~1-0.1 μJy/arcsec^2 at 1.4 GHz) permeating the cluster volume of a cluster. They are typically extended with sizes of $\geq 1Mpc$, regular in morphology and located at the center of the cluster.

Relic sources are diffuse extended sources similar to radio halos in their low surface brightness, large size ($\geq 1Mpc$) and steep spectrum ($\alpha \geq 1$), but, unlike halos they are located in cluster peripheral regions. Observations of relics provide the best indications for the presence of μG level magnetic fields and relativistic particles in cluster outskirts. They provide evidence for the acceleration of relativistic particles at shockfronts at large distance (Mpc scale) from the cluster centers. Some galaxy clusters host both radio halos and radio relics. Some host a double radio relic system as indicated in figure below.

CLUSTER MERGERS

Clusters of galaxies are the largest gravitationally bound systems in the Universe. Most of the gravitating matter in any cluster is in the form of dark matter (~ 80%). Some of the luminous matter is in galaxies (~3-5%), the rest is in diffuse hot gas (~15-17%),detected in X-ray through its thermal bremsstrahlung emission. This thermal plasmaconsisting of particles of energies of several keV, is commonly referred to as intracluster medium (ICM). The ICM can also contain highly relativistic particles. While the energy density is less than 1% of the energy density in the thermal plasma, these relativistic particles are very important in the cluster formation and evolution. Diffuse radio emission from the ICM (radio halos and relics) is the most direct probe of magnetic fields in clusters.

The ICM in merging clusters is likely to be in a violent or turbulent dynamical state. It is found that the diffuse sources are detected in clusters which have recently undergone a merger event, thus leading to the

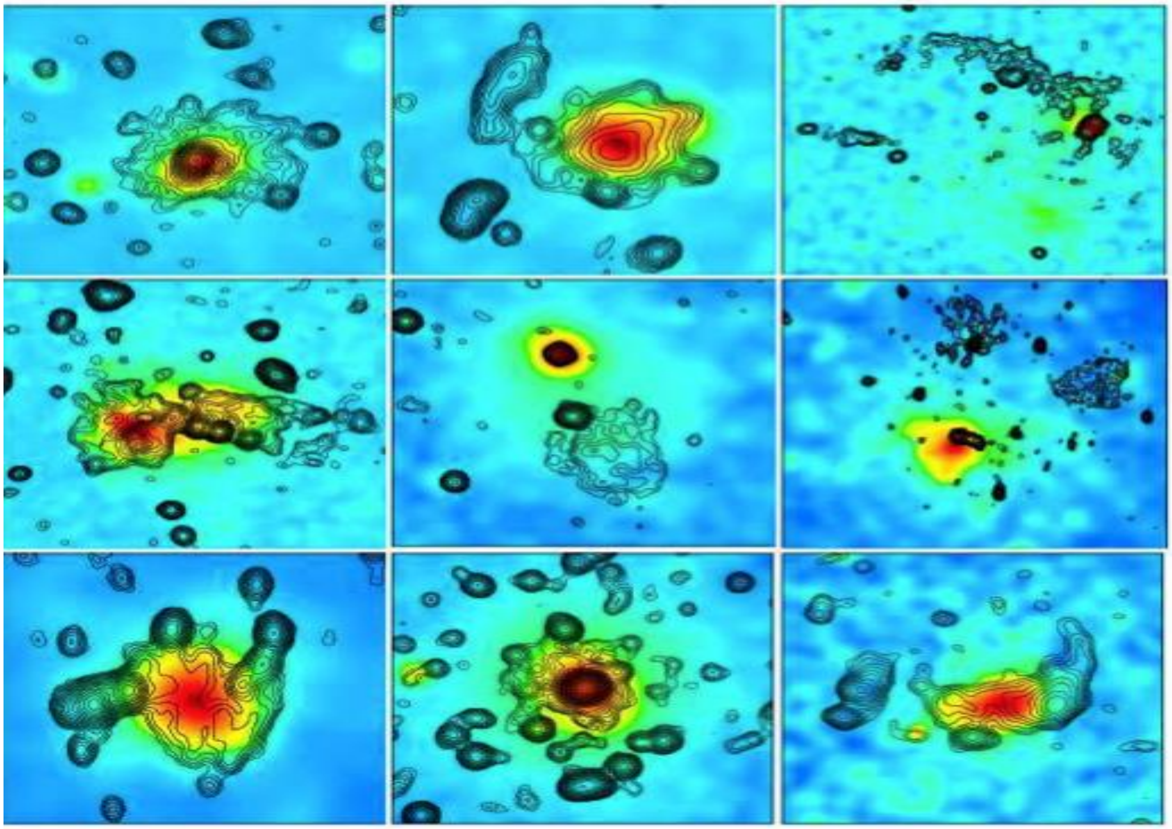

Figure 2: Collection of clusters showing several types of radio emission, shown in contours, overlaid onto the X-ray emission, shown in colors.Clusters are (from left to right and from top to bottom) A 2219 (halo), A 2744 (halo + relic), A 115 (relic), A 754 (complex, halo plus relic), A 1664 (relic), A 548b (relic), A 520 (halo), A 2029 (mini-halo), RXCJ1314.4-2515 (halo plus double relics) (e.g. Feretti2012).

idea that they are energized by turbulence and shocks in cluster mergers (**see Giovannini & Feretti 2002, & references therein).**

Turbulent magnetohydrodynamic (MHD) reacceleration of electrons in the ICM caused by energetic cluster mergers is a popular model proposed to explain the origin of radio halos (**e.g. Brunetti et al 2003**); whereas acceleration of electrons at outgoing merger shocks is believed to be responsible for radio relics (**e.g.**

Ferrari etal 2008 and references therein). All radio halos are associated with cluster mergers, but not all cluster mergers exhibit radio halos or relics.

In general, from the spectra of diffuse radio sources, it is known that the radiative lifetime of the relativistic electrons, considering synchrotron and inverse Compton (IC) energy losses, is of the order of ~ 10^8 year. This is too short to allow particle diffusion throughout the cluster volume. Thus, the radiating electrons cannot have been produced at some localized point of the cluster, but they must undergo in situ energization. This model is known as Primary or Reacceleration Model of radio halo formation (**e.g. Feretti 2004**).

Clearly, this model has not considered high-frequency observations but we have explored high-frequency observations of the cluster mergers in this thesis. The clusters studied in this thesis are:

1. **MACSJ0417.5-1154**, at a redshift of 0.443is the second most X-ray luminous galaxy cluster in the Massive Cluster Survey (MACS) with an X-ray luminosity in the 0.1-2.4 keV band of 2.9 x 10^{45} erg/s of the MACS sample and exhibits disturbed X-ray morphology.

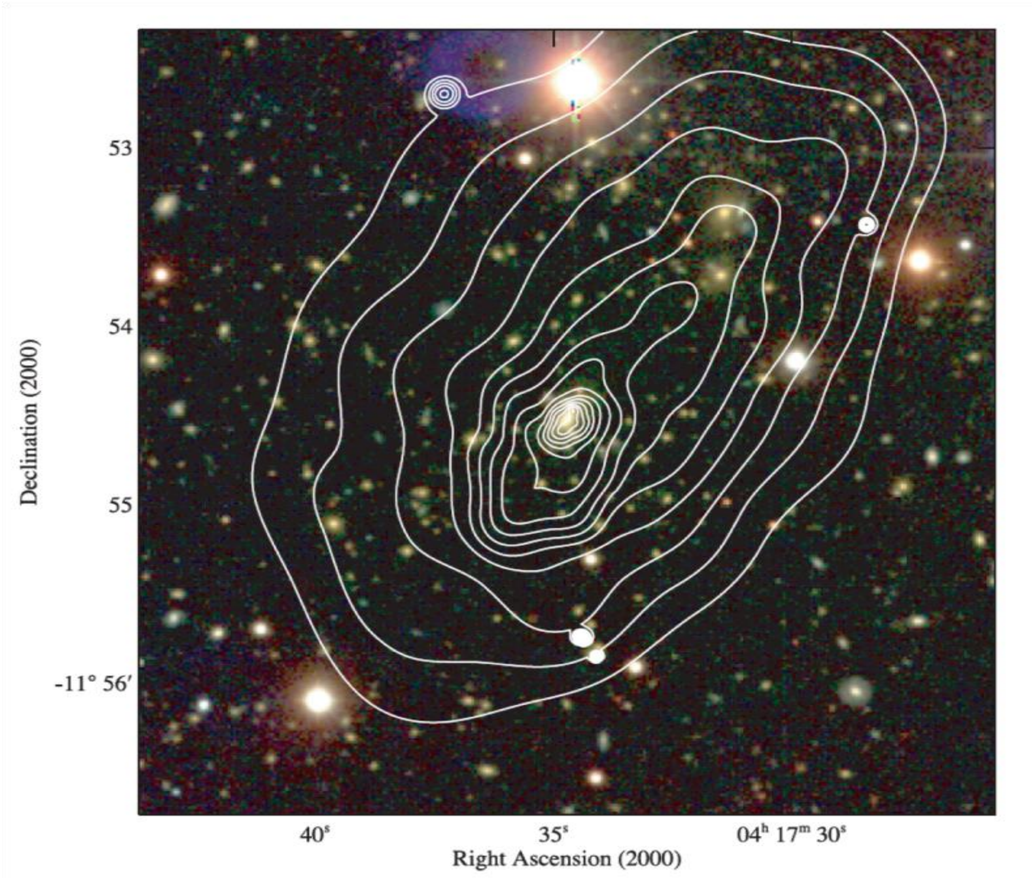

Figure 3: Contours of the X-ray surface brightness in the 0.5–7-keV band as observed with Chandra/ACIS-I overlaid on color images obtained with the UH 2.2-m telescope (V, R, I; 12min per filter). The image span 1.5 Mpc on the side at the cluster redshift. Contours are spaced logarithmically at the same levels for the image. The Chandra data were adaptively smoothed to 3σ significance using the ASMOOTH *algorithm of Ebeling,White, and Rangarajan (2005). Credit:Massive Clusters Catalogue, Ebeling et al.*

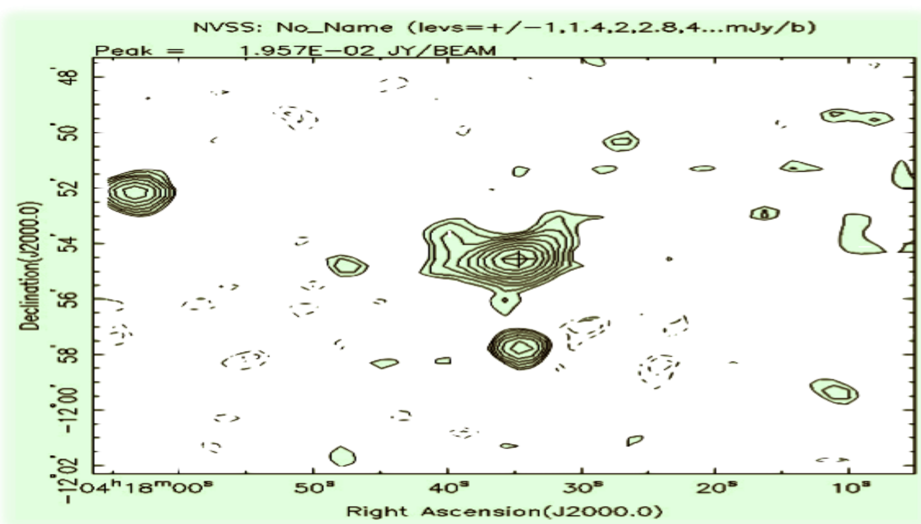

Figure 4: NVSS catalog image shows obvious diffuse emission at 1.4 GHz

MACSJ0417.5-1154 shows strange features in figure 3 and 4 – elongated and non-concentric X-ray contours. So, we analyzed this cluster at higher frequencies (1.4, 5.5, 9, 18 GHz) to check the shape of the spectra in order to test the current models.

2. Further, we present results from observations of the **Bullet cluster 1E 0657-55.8** at 5.5 and 9 GHz using Australia Telescope Compact Array (ATCA). The Bullet cluster is one of the hottest and most X-ray luminous galaxy clusters discovered thus far. The cluster merger gets its name from the shape of the smaller cluster. The diffuse emission studied in the Bullet cluster is then compared with the diffuse emission in the cluster MACSJ0417.5-1154.

SUMMARY OF RESEARCH WORK PRESENTED IN THE THESIS

1. As an application of the spherical collapse model, we calculated quantities of interest for an isothermal halo and discussed its implications for the formation of a cluster of galaxies.

2. For the Bullet cluster, Our results show detection of diffuse radio emission in this cluster. Our findings are consistent with the previous observations by **Shimwell et al. (2014, 2015)** at 1.1 – 3.1 GHz. Our results indicate steepening in the spectral index at higher frequencies (> 5 GHz) for region A. The spectrum can be fit well by a broken power law. We discuss the possibility of a few recent theoretical models explaining this break in the power law spectrum and find that a modified Diffusive Shock Acceleration (DSA) model or turbulent reacceleration model may be relevant. Deep radio observations at high frequencies (>5 GHz) are required for a detailed comparison with this model.

3. Then, we studied multi-frequency observations of the cluster MACSJ0417.5-1154 at 5.5 & 9 GHz from ATCA. Images from our data clearly show diffuse emission upto 10 GHz. We discovered above 1 GHz there is diffuse emission in

cluster MACSJ0417.5-1154 which has implications for radio halo models. In this thesis, we focus on the spectral properties of the diffuse sources at both GHz and 100s of MHz frequencies (we use archival TGSS and GLEAM data for the low frequencies) in clusters of galaxies in order to test the current models. With this aim, we present the results from high-frequency observations of extended emissions from this galaxy cluster, performed with ATCA (Australia Telescope Compact Array).

4. Additionally, we analyze the spectrum of this cluster, and find that the cut-off feature reported as sharp, and appearing to be anomalous, is likely an artifact of an underestimate of diffuse emission in the cluster at low (i.e. 100s of MHz) frequencies. On including archival TGSS and GLEAM data, we found that a single spectral index may fit the spectrum well, and therefore the sharp cutoff reported earlier may not be present, which is consistent with the cluster merger being relatively young.

Our 5.5 and 9 GHz data exhibit a steepening of the spectrum of the radio relic in the Bullet Cluster. Recent theoretical models may lead to a better understanding of the origin of the radio relic in the Bullet Cluster, as well as the radio halo in the cluster MACS J0417.5-1154, as has been demonstrated for the 'Sausage' relic – further observations with high resolution are needed at 5.5 and 9 GHz to facilitate comparison with these models.

1. **Images of Diffuse Emission in the two cluster mergers**

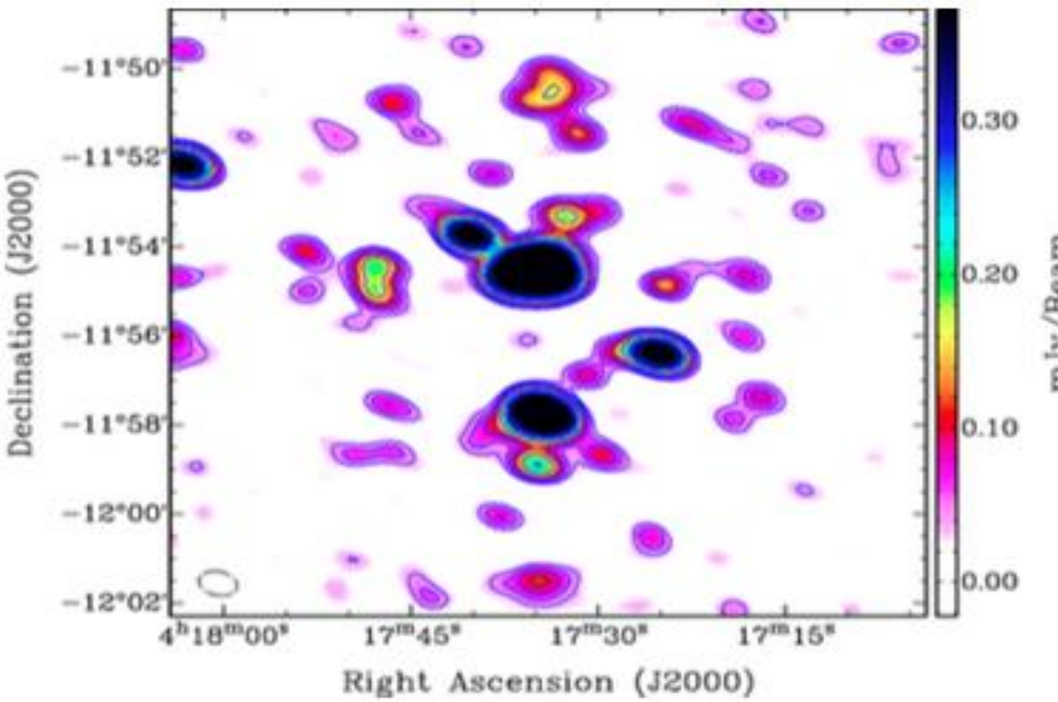

Figure 5. A natural–weighted image of the entire region of the cluster MACS J0417−1154 at 5.5 GHz from ATCA. The beam, which is 46.3″×31.9″ is shown in the bottom left–hand corner. Noise rms is 8μJy/beam.Contour levels start at 5σ and increase by a factor of $\sqrt{2}$.

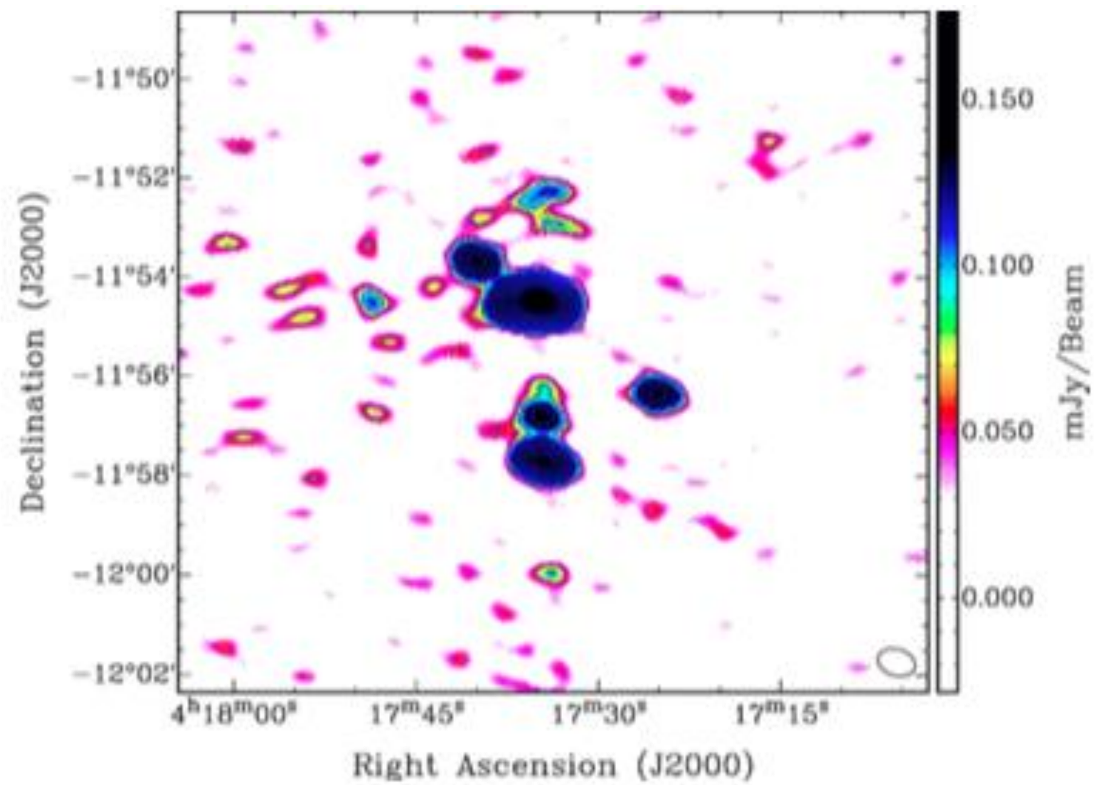

Figure 6. 9 GHz image of the cluster MACS J0417.5−1154, made with a 46.3″× 31.9″ beam, shown as an ellipse in the bottom left corner of the image. Noise rms is 12μJy beam^{-1}. Contour levels start at 5σ and increase by a factor of $\sqrt{2}$.

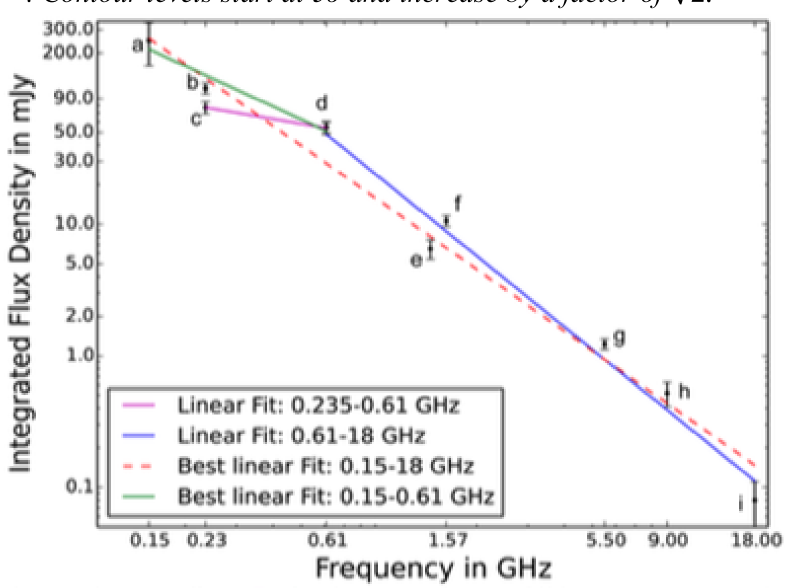

Figure 7. The spectrum of diffuse radio emission in MACSJ0417.5-1154. Different linear fits are shown here for data ranging from 150 MHz to 18 GHz. The best single line fit spectral index is $\alpha = -1.61 \pm 0.12$, shown here as a dotted red line. 150 &

235 MHz data are taken from the GLEAM survey, and are really upper limits to the diffuse emission. The magenta line from 235 to 610 MHz is the spectrum, considering only the value of diffuse emission at 235 MHz, which is likely underestimated.

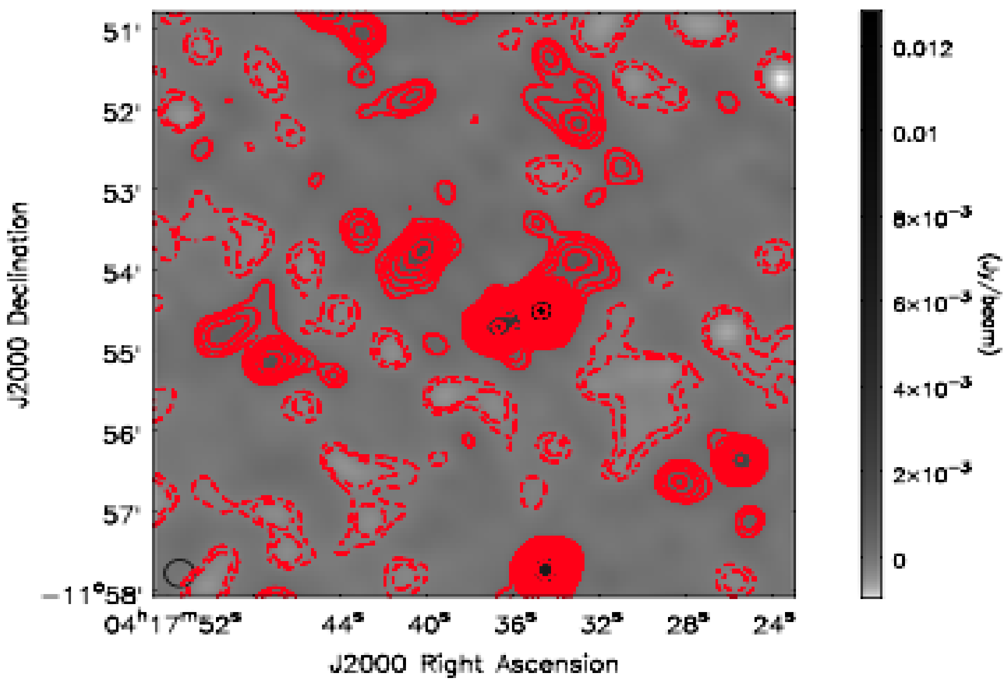

Figure 8. The GMRT radio image of the galaxy cluster MACS J0417.5-1154 at 1387 MHz. The resolution of this image is 20" with rms noise of 50μJy/beam. The Contour levels start at 5σ and increase by a factor of $\sqrt{2}$*. Dashed lines are negative contours at 3 & 5σ*

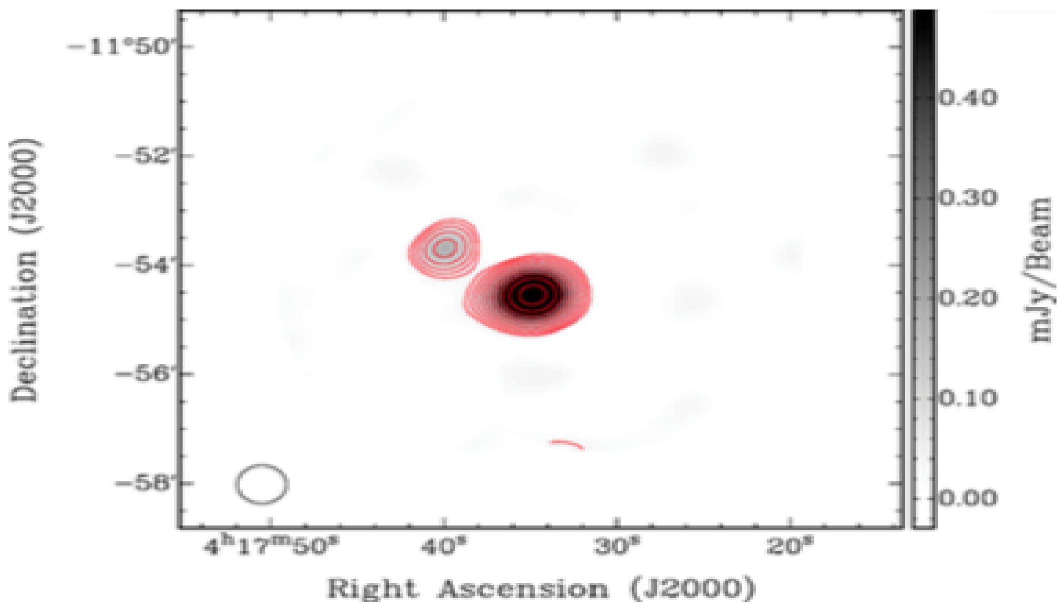

Figure 9. The ATCA radio image of the galaxy Cluster MACS J0417.5-1154 at 18 GHz. The resolution of this image is 42" with rms noise of 8μJy/beam. The Contour levels start at 5σ and increase by a factor of $\sqrt{2}$.

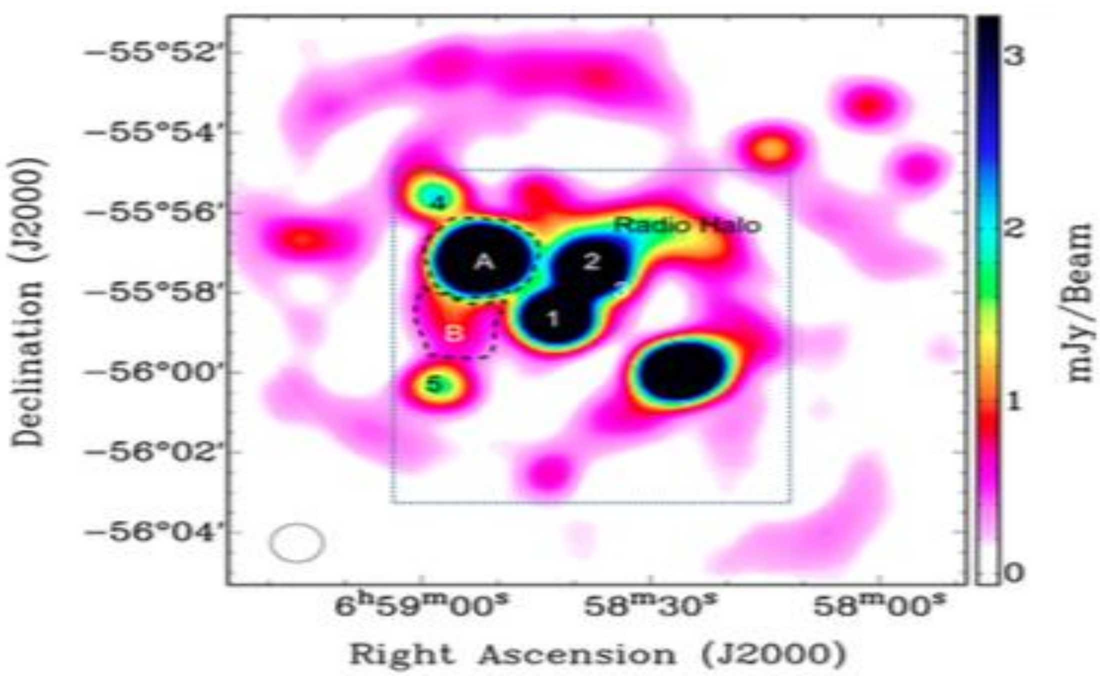

Figure 10. A natural–weighted image of the Bullet cluster at 5.5 GHz from ATCA. The beam, which is $57'' \times 57''$ *is shown in the bottom left–hand corner. Noise rms is 20μJy/beam.*

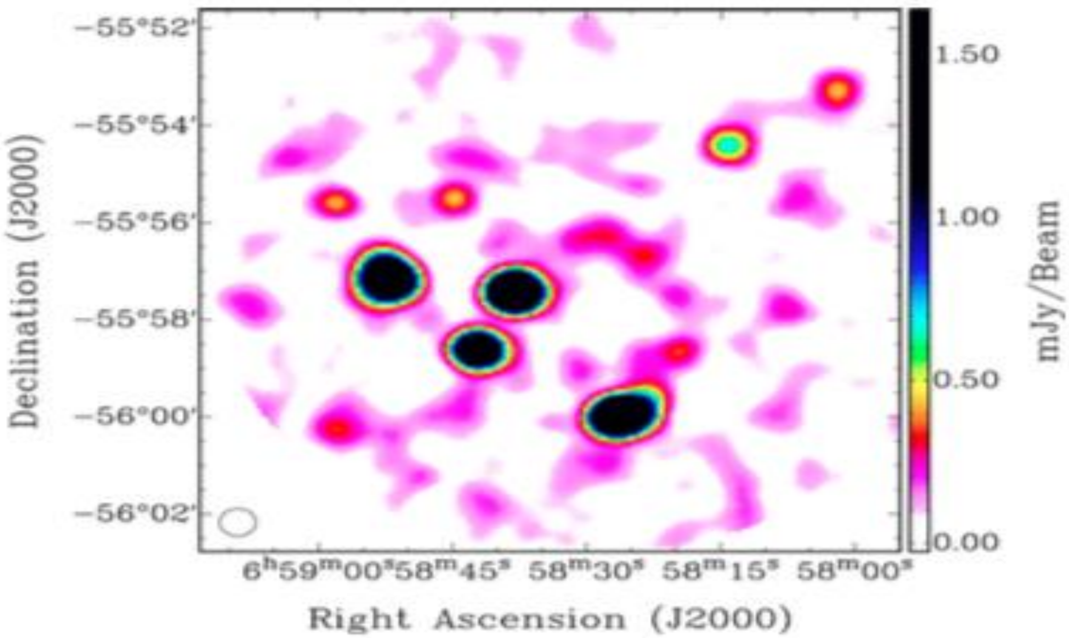

Figure 11. A natural–weighted image of the Bullet cluster at 9 GHz from ATCA. The beam, which is 34″× 34″ is shown in the bottom left–hand corner. Noise rms is 25μJy/beam.

Throughout the present thesis a cosmology with H_0 = 70 km s^{-1} Mpc^{-1}, Ω_m=0.3 and Ω_λ=0.7 is assumed.

The new generation radio telescopes like LOFAR, U-GMRT, and SKA will provide better sensitivity and resolution than today frequencies. Discoveries of new ultra-steep spectrum components in the known radio halo and relic sources and of an entirely new sample of radio halos and relics are awaited from the new generation of telescopes.

REFERENCES

[1] C H Lineweaver, L Tenorio, G F Smoot, *et al*, The dipole observed in the COBE DMR 4 year data, *ApJ*., 470, 38, 1996.

[2] M I Scrimgeour, T Davis, C Blake *et al*, The wiggleZ dark energy survey: the transition to large-scale cosmic homogeneity, *MNRAS*, 425, 116, 2012.

[3] J E Gunn and J R Gott III, On the infall of matter into clusters of galaxies and some effects on their evolution, *ApJ*, 176, 1, 1972.

[4] D Lynden-Bell, Statistical mechanics of violent relaxation in stellar systems, *MNRAS*, 136, 101, 1967.

[5] L D Landau, E M Lifshitz, *Fluid Mechanics*, Course of Theoretical Physics, Pergamon Press, Oxford, 1959.

[6] Ferretti et al AstronAstrophys Rev (2012) 20:54.

[7] Brunetti, G.; Giacintucci, S.; Cassano, R. et al., A low-frequency radio halo associated with a cluster of galaxies, Nature 455, 944-947 (2008).

[8] Giacintucci, S., Diffuse radio sources in colliding galaxy clusters, Mem. S.A.I Vol. 75, 282 (2008).

[9] Cassano, R., Radio Halos, cluster mergers and the role of future **LOFAR** observations, Mem. S.A.It. Vol. , 1(2008).

[10] Ferretti L., Radio observations of cluster mergers, Santa Fe NM, 3-6 February 2004.

[11]K.S. Dwarakanath, Siddharth Malu & Ruta Kale, Discovery of a Giant Radio Halo in a Massive Merging Cluster at z=0.443, J. Astrophys. Astr. (2011) 32, 529-532.

LIST OF PUBLICATIONS

Peer Reviewed

- Pritpal Sandhu, SiddharthMalu, Ramij Raja and Abhirup Datta (2018), "The peculiar cluster MACSJ0417-1154 in the C & X- bands", Astrophysics and Space Science, 363:133 (https://doi.org/10.1007/s10509 - 018 -3354 - 6)

- Siddharth Malu, Abhirup Datta and Pritpal Sandhu (2016), "First detection at 5.5 and 9 GHz of the radio relics in bullet cluster with ATCA", Astrophysics and Space Science, 361(8), 1-8 (doi: 10.1007/s10509-016-2844-7)

- Prof. J S Bagla & Pritpal Kaur Sandhu (2015), "Gravitational collapse and structure formation in an expanding universe", Resonance Journal of Science Education,Vol. 20, issue No. 9.

Under Review

- Pritpal Sandhu, Ramij Raja, Majidul Rahaman, Siddharth Malu & Abhirup Datta (2018),“ Radio Observations of the cluster MACSJ0417.5-1154", Journal of Astronomy & Astrophysics, under review.

Publications other than thesis work

- Gaurav Bajpai, Mohd. Nasir, E. G. Rini, Pritpal K. Sandhu, SiddharthMalu, Sunil Kumar, Parasharam M. Shirage, and SomadityaSen (2016), "Structural and Mechanical Characterization of Si-DopedZnO", Journal of Nanoscience and Nanotechnology, Vol. 16, 1–7 (doi:10.1166/jnn.2016.13020).

- N. Rathnasree, Lavanya Nemani, Pritpal Sandhu,Pulkit Agarwal, Sonia Munjal,Megha Rajoria, Ramesh Chikara, Naresh Kumar, C B Devgun ,Sneh Kesari, Siddharth Madan, and Priyanka Gupta (2017), "Towards the restoration of the Jantar Mantar observatory instruments at Delhi Calibration and observations with the Jaiprakash and Ram Yantra", accepted in Proceedings of the IXth International Conference on Oriental Astronomy, IISER Pune.

TABLE OF CONTENTS

CONTENTS

PAGE NO.

LIST OF FIGURES

LIST OF TABLES

CHAPTER 1

INTRODUCTION AND PLAN OF THE THESIS

In this introductory chapter, we introduce the relevant concepts in cosmology, followed by a brief discussion of how the last scattering surface leads to the formation of structure in the universe; we also briefly discuss how perturbations in matter density in the early universe (which lead to all structure that we see in the universe today) can be studied through the cosmic microwave background (CMB).

Thereafter, we present a brief plan of this thesis in the last section.

1.1 COSMOLOGY

It is only relatively recently (19th century onwards) that scientists have made predictions about and observations of the early Universe and have come up with a successful paradigm that explains the observations and reconcile them with physical theories.

A few decades ago, two scientists at Bell Labs decided to test their shiny new antenna by pointing it to different parts of the sky. They ended up with a residual noise with an equivalent temperature of 3K and a huge confusion on their hands. The puzzle about the source of this seemingly uniform source was solved only when physicists at the nearby Princeton University shared with them their ideas about the origins of the universe. Thus started the field of CMB cosmology, one which has proved to be even more fundamental to our understanding of the universe over time.

The rest of this chapter will briefly introduce two of the three “pillars” of Cosmology (we do not discuss primoridal nucleosynthesis here - see, e.g.[1]), as well as the background in General Relativity and discuss the physics and importance of CMB temperature and polarization anisotropies and how they can acts as windows to the very early universe.

1.1.1 HUBBLE'S LAW AND FRWL COSMOLOGY

In the 1920s[2], Hubble pointed his telescope to a few galaxies and discovered the fact that each one of them was moving away from us, with a velocity proportional to the distance between us and the galaxy we're looking at. Since there is no reason to expect that the Milky Way is at the centre of the Universe, it is reasonable to extend this result and say that every galaxy is receding from every other with the same property of recession. This has been checked with observations as well. It turns out that the formalism for expressing Hubble's law is simple, and the idea along with all its results remains the same in the General Theory of Relativity (GR henceforth) as well as Newtonian mechanics. Clearly, Newtonian mechanics is not up to the task of dealing with the expanding Universe, for several reasons.

Let us denote by r the physical distance between two galaxies, and by v their relative
velocity. Then, Hubble law says that v α r. We can then write the equation

$$v = Hr \tag{1.1}$$

where H is called the Hubble parameter (technically, it should be a "constant", but we have tacitly ignored curvature and every other issue associated with GR; H can be thought to encompass all these GR effects). We would do well to remember that this expansion is not just a widening in distance between galaxies, it is a "stretching" of space (space-time, strictly speaking, but the beauty of the presently-accepted Friedmann-Robertson-Walker-Lemaitre (FRWL) universe model is that one can view "spatial slices" or spatial hypersurfaces at different times; it is possible that the Universe is not FRWL - there are other solutions to the Einstein equations that are not homogeneous spatially or temporally, but while that is an active area of research, everyone in the astrophysics community agrees that FRWL is by far the most likely model that the Universe obeys). In that case, we can (as a matter of fact, we ought to, as we will see later) reformulate the picture in the following way. We encode the expansion of the Universe in a single variable which is a function of time and define what is called a “comoving” frame of reference in which the distance between, say, any two given galaxies is a constant, i.e. we are “viewing” this distance from a pre-defined epoch. There is nothing that prevents us from this pre-defined epoch to “now” - indeed; this is often a convenient choice, as we will see. The variable that encodes the expansion of the Universe is called the “scale-factor”, which we represent here with a (t). We can then write any given physical distance as

$$v = a(t)\, x \tag{1.2}$$

where x is the comoving distance between the two given points under consideration. The velocity is v = dr/dt, meaning that

$$v = \frac{d}{dt}(\, a(t)\, x\,) = \, x\, \frac{da}{dt} \tag{1.3}$$

where the last equality holds because x (i.e. the comoving distance between between any two given objects) is fixed by definition. We can then write the Hubble law as

$$v = x\, \frac{da}{dt} = H\, a\, x = H\, r \tag{1.4}$$

$$\Rightarrow H = \frac{1}{a}\frac{da}{dt}$$

This, then, is the most general definition of the Hubble parameter. By calling it a parameter, we have gotten away with proving this relation for any theory of gravity we might choose to consider - Newtonian or Einsteinian.

Next, we look at FRWL metric (eq. 1.7). Put k=0 and get eq. 1.5 in spherical polar co-ordinates:

$$ds^2 = dt^2 - a(t)^2\, [dr^2 + r^2\, d\Omega^2] \tag{1.5}$$

This represents flat space-time only. Let us generalize this to a space-time with positive curvature, in analogy with a 2-sphere (the object we know and love as a “sphere”). This is a 3-d surface, so in analogy with the “normal” or 2-d sphere whose equation is

$$x^2 + y^2 + z^2 + w^2 = b^2 \tag{1.6}$$

Here, x, y and z are ordinary spatial dimensions, and w can be thought of as a fiducial variable, whose physical interpretation is that it is a 3-sphere embedded in 4-d space. If we accept this without much ado, we can go about expressing w completely in terms of r, b etc. in the following way.

Replacing w in terms of x, y and z would eventually give us

$$ds^2 = dt^2 - a(t)^2 \left[\frac{dr^2}{1 - kr^2} + r^2 d\Omega^2\right] \tag{1.7}$$

where k is the curvature, and can take on values -1, 0 or 1.

Having studied the geometrical aspects of the metric, let us now turn our attention to the dynamics of the Universe. The equations that are derived below are again very useful, especially in their most general form, and their beauty lies in the fact that though the derivation has nothing to do with GR, these are the exact same result we would get if we worked with the Einstein equations instead. The GR approach will be outlined briefly after the following derivation. Let us start from the first law of thermodynamics:

$$dU + pdV = 0 \tag{1.8}$$

where, naturally, U = ρ a^3, where ρ is the density (total energy density, but this can be simplified for those epochs when the total energy density is dominated by just one component) and a the scale factor, which is a function of time. Substituting for U, we get

$$\begin{gathered} a^3 d\rho + 3a^2 \rho da + 3a^2 p da = 0 \\ \Rightarrow 3\left(\frac{p}{\rho} + 1\right)\frac{da}{a} = \frac{d\rho}{\rho} \end{gathered} \tag{1.9}$$

Now p/□ is what is referred to as the equation of state. It is usually denoted by w in the literature, so we will follow the convention:

$$3\,(\,w+1\,)\,\frac{da}{a} = \frac{d\rho}{\rho}$$

(1.10)

$$\Rightarrow \frac{d\ln\rho}{d\ln a} = -3(1+w)$$

This, then, is the most general expression relating ρ and a. Notice that we have not yet made any assumption about w - it may very well be a function of a, and this equation will still hold.

If we assume a constant equation of state w (as is true for baryonic matter and radiation), we get a simpler relation:

$$\rho \sim a^{-3(1+w)} \tag{1.11}$$

After cosmological inflation ends, there is a small amount (~ 1 in 10^5) anisotropy remaining in the matter density. There are two opposing forces – that of gravity (attractive), and radiation pressure (repulsive), which means that oscillations are set up in matter in the early universe.

1.1.2 COSMIC MICROWAVE BACKGROUND (CMB)

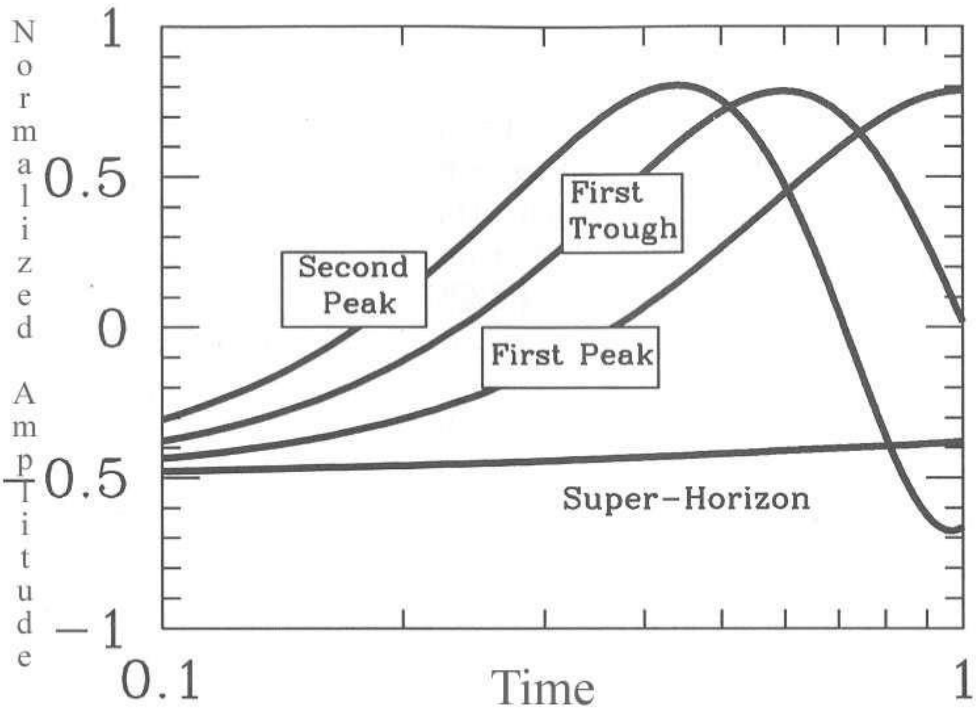

Figure 1.1: Evolution of perturbations. Shown here are three oscillation sizes which are important for extracting information from the CMB.

The cosmic microwave background (CMB) is another "pillar" of cosmology, and by far the most informative one. Before we delve into what cosmological parameters can be constrained with the CMB, let us look briefly at the CMB itself. Hubble's law imples that as we go back in time, the size of the universe decreases monotonically. This means that the wavelength of photons decreases and the temperature of the universe increases. This implies that there must have been an epoch earlier than which the universe would have been ionized. This epoch is called "recombination" or "last scattering surface" and we shall use these terms interchangably. Before recombination, the universe can be thought of as a "primordial soup" of protons, electrons, neutrons (i.e. baryonic matter) and photons. Baryonic matter experiences two opposing forces: the attractive force of gravity and repulsive force of radiation pressure. These two opposing forces set up acoustic oscillations in the "primordial soup". But these end at recombination, and the photons that travel freely after recombination constitute the CMB. We need to remember, though, that the universe is expanding even as these acoustic oscillations permeate the universe. Keeping this in mind, and looking at comoving distances instead of physical ones, let us examine the acoustic oscillations in a little more detail.

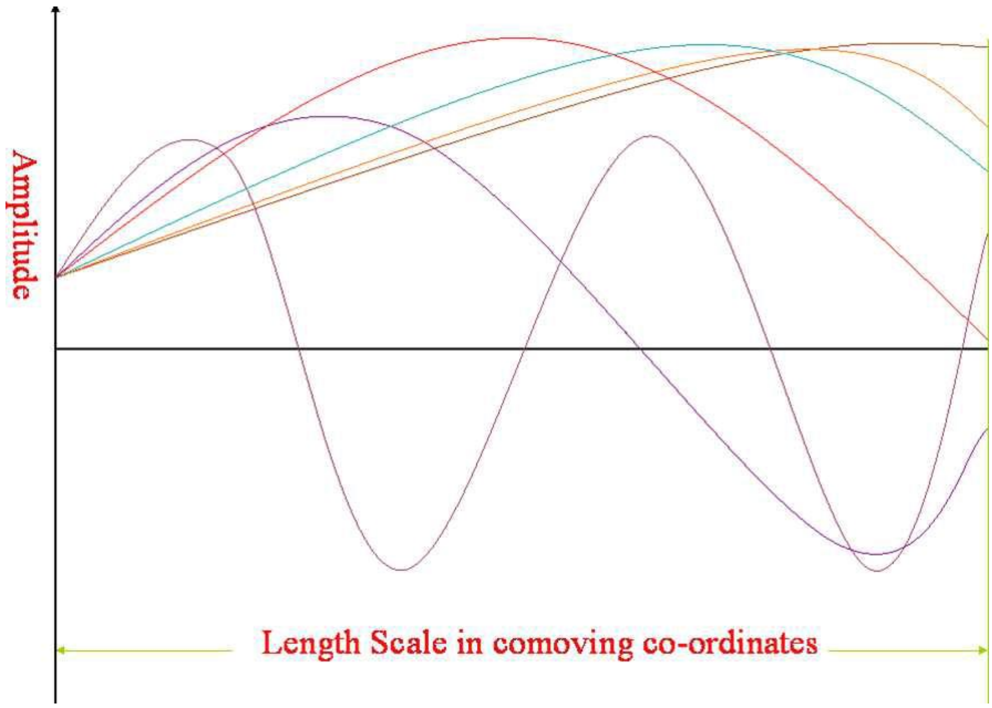

Figure 1.2: Acoustic oscillations in the CMB. What we are able to measure today is proportional to the square of the amplitude at recombination, via the CMB power spectrum.

Ignoring the origin of the oscillations for the moment, we immediately see from figs.(1.1) and (1.2) that every length scale ends up with a different amplitude. If the wavelength of a “mode” (i.e. a length scale) is sufficiently large, small changes in the wavelength do not produce an appreciable effect (this is the reason that the power spectrum is nearly constant for low l’s - see fig.(2.4)). As the wavelength decreases, however, the amplitude of the mode at recombination increases until it reaches a maximum, and then decreases with decreasing wavelength.

The amplitude cannot possibly be measured today, but the power level can, and so this is the quantity that CMB cosmology aims to measure. The reason that we can measure this quantity (i.e. the power in fluctuations in matter) is that the photons that we detect today as the CMB were coupled to matter before recombination. This is why fluctuations in the CMB temperature directly indicate fluctuations in the matter before recombination. What makes the study of the CMB fundamental to our understanding of the universe is that it is these small fluctuations in matter that grow to become all the structure we see in the universe today. **The study of fluctuations in the CMB is the study of the origins of all structure in the universe.**

The largest structures thus formed after recombination or the last scattering surface are clusters of galaxies, briefly discussed below.

1.2 GALAXY CLUSTERS

Galaxy clusters are the largest gravitationally bound objects in the universe. Since the 1930's they have been used as remote laboratories for studying gravity on large scales. Our first evidence for the existence of dark matter came from observations of the motions of galaxies in clusters at visible wavelengths (Zwicky). In the past two decades galaxy clusters have become an important cosmological tool for studying the accelerated expansion of the universe caused by dark energy. However, recently we have learned that these clusters are not as simple as they appear. We now know that galaxy clusters frequently collided in the early universe, causing the most energetic events in the universe. Most clusters are really the result of 'cluster mergers'. The collisions have major impact on the structure and evolution of the clusters and the cosmological conclusions we draw from observing them. The goal of the research program proposed here is to exploit new detector technologies in radio astronomy to understand cluster mergers well enough to use clusters for precision tests of cosmology.

In the current paradigm of structure formation, clusters are thought to form via a hierarchical sequence of mergers and accretion of smaller systems driven by dark matter that dominates the gravitational field. Mergers, the most energetic phenomena since the Big Bang, dissipate up to 10^{63} - 10^{64} ergs during one cluster crossing time (~Gyr). This energy is dissipated primarily at shocks into heating of the gas to high temperature, but also through large-scale ICM motions (Kravtsov 2012; Norman 1999; Ryu 2008).

Galaxy clusters are therefore veritable crossroads of cosmology and astrophysics; on one hand they probe the physics that governs the dynamics of the large-scale structure in the Universe, while on the other hand they are laboratories to study the processes of dissipation of the gravitational energy at smaller scales. In particular, a fraction of the energy that is dissipated during the hierarchial sequence of matter accretion can be channeled into non-thermal plasma components, i.e. relativistic particles and magnetic fields in the ICM (Brunetti & Jones 2014))

The hot gas in these merged clusters emits copious amounts of radio radiation across the radio spectrum. It has been pointed out that it should be impossible to detect *any* diffuse emission from galaxy cluster mergers, particularly diffuse emission from the central regions referred to as Radio Halos, above 10 GHz, due to the steep (falling with frequency) spectra exhibited by these Radio Halos. A well-studied model for the formation of Radio Halos, called the "Primary Model", predicts a steep spectrum, (Brunetti et al., Nature, 2008).

A large fraction of the mass of rich clusters of galaxies that emits electromagnetic radiation is in the form of a diffuse (density ~ 10^{-3} atoms cm^{-3}) intracluster medium (ICM), macroscopically at rest in the cluster gravitational potential well. This gas is hot (10^8 K) and especially conspicuous in x-rays, which are produced by thermal bremsstrahlung.

Individual galaxies in clusters are, of course, radio emitters, as are those outside of clusters. However, the location of cluster galaxies in a high-density environment brings about peculiar characteristics which are usually attributed to their interaction with the ICM or to the exceptional character of the objects dwelling in the cluster cores (e.g., cD galaxies are central dominant galaxy or largest galaxies). The characteristics of the radio emission arising from the interaction of radio sources with the ICM, as well as the global radio properties are associated with the ICM itself.

1.3 PLAN OF THE THESIS

In this thesis, we present multi-frequency radio observations of a peculiar galaxy cluster MACS J0417.5-1154. In particular, we examine diffuse emission in the centre of this cluster merger at various frequencies – at 5.5 and 9 GHz, to explore the high-frequency behavior of this diffuse emission, and at frequencies lower than 300 MHz, to explore the behavior of the spectrum of diffuse emission at low frequencies, and how that affects the overall spectrum and spectral index. Diffuse emission (which is really synchrotron radiation) from cluster mergers is thought to arise due to the acceleration of electrons caused by mergers.

We also examine the high frequency diffuse emission from the Bullet cluster of galaxies and compare it with the diffuse emission from the cluster MACS J0417.5-1154. While both cluster mergers exhibit diffuse emission from their central regions, they differ significantly in the morphology and dynamics of the merger process. This is why, the spectrum of the two cluster mergers is expected to be different. For the Bullet cluster, we expect to see a break in the spectrum at a certain frequency, since the age of the merger is ~ 100 million years. Also, cut-off frequency depends on the magnetic fields and acceleration efficiency in the ICM and on the energy density of CMB radiation (Cassano 2010). Further, it is believed that ~ Gyr after cluster merger turbulence in the ICM becomes weaker and there are a strong synchrotron energy losses which produce a cut-off between ~ 100 MHz and GHz frequency range (Cassano 2010; Venturi 2011). Hence, higher the break frequency in the spectrum then higher would be the energy of the cluster merger. That is why, frequency of the break is inversely proportional to the age of the merger.

However, it is unclear whether a break in the spectrum should be expected for the cluster merger MACS J0417.5-1154 (MACS0417 henceforth). Being a relatively young cluster merger, we should expect the break to occur at a high frequency. However, MACS0417 shows a break at a very low frequency, namely, at 610 MHz. This is surprising, as this low-frequency break is indicative of an aged plasma, belonging to a merger that may be up to ~1 Gyr old, and not a relatively young merger.

We present data from JVLA, ATCA, as well as archival data from the GLEAM survey, in order to examine the spectrum of diffuse emission in MACS0417 over more than a decade in frequency – 150 MHz to 18 GHz.

We present an overview of galaxy clusters in Chapter 2, including a simple spherical collapse model. In Chapter 3, present results from 21 cm observations made with a simple and cheap receiver system. We also present an overview of radio interferometric observations in Chapter 3.

In Chapter 4, we present ATCA observations of the Bullet cluster, and examine the diffuse emission in the Bullet cluster at 5.5 GHz and 9 GHz – both the radio relic and the radio halo in the Bullet cluster are discussed.

In Chapter 5, we present data from our 5.5 GHz and 9 GHz ATCA observations of MACS0417, as well as archival GLEAM data, from 70 MHz to 235 MHz. Spectral indices derived from a combination of the ATCA data and archival GLEAM data are then compared with the spectral indices derived earlier by Parekh et al. (2017) from 235 MHz and 610 MHz GMRT data, and 1575 MHz JVLA data. A combined spectral index from 70 MHz to 9 GHz is also calculated. In particular, we discuss the effect of an underestimate of diffuse emission at low frequencies on the spectral index estimation.

In Chapter 6, we present our 1.387 GHz GMRT and 18 GHz ATCA observations of MACS0417, as well as archival TGSS data, to get an estimate of the spectrum from 150 MHz to 18 GHz, i.e. more than a decade in frequency. We compare the spectral fit with the one provided in earlier publications about the cluster and make comments about the age of the merger.

Finally, we present our conclusions about the diffuse emission in MACS0417 in Chapter 7.

CHAPTER 2

GALAXY CLUSTERS AND CLUSTER MERGERS

In this chapter, we discuss the galaxy clusters and their properties, as observed in the optical, X-ray and radio parts of the electromagnetic spectrum. Each of these frequencies yields different information about the clusters. For instance, X-ray observations yield information about thermal processes in the intracluster medium, and radio observations provide information about non-thermal processes. This thesis is focused on radio observations of diffuse emission from galaxy clusters (in particular, cluster mergers).

We discuss a simple model for the formation of large-scale structures in the universe, applying a semi-Newtonian treatment. We then briefly describe the optical and X-ray properties of clusters, and then go on to describe radio emission from clusters; in particular, from mergers between clusters of galaxies.

2.1 The Spherical Collapse Model

(*Based on Bagla, J. and Kaur, P. , "Gravitational collapse and structure formation in an expanding universe", Resonance Journal of Science Education,Vol. 20, issue No. 9*)

In the previous chapter, we discussed briefly how acoustic oscillations of matter over and under-densities provide the seeds of all structure in the universe.

Having briefly mentioned the relevant physical processes in galaxy clusters that we intend to study, we discuss how these objects form, through the spherical collapse model, with a semi-Newtonian treatment of spherical collapse.

Consider a spherical region with a constant over-density that is expanding along with the rest of the universe during the early times. We assume that the initial over-density is small in magnitude and that the size of the over-dense region is also small. Now consider a shell, initially at radius r_i, which encloses a mass M. It can be shown that mass will remain conserved as the system evolves. The equation of motion is:

$$\ddot{r} = -\frac{GM}{r^2}$$

Using the constancy of mass enclosed we obtain the first integral of motion:

$$\frac{\dot{r}^2}{2} = \frac{GM}{r} + E \qquad (1)$$

where E = E'/m. The energy E has to be negative for this to be a bound perturbation and we write it explicitly as E = −|E|. Further, as mentioned above, we assume that the perturbation is taken to be situated in an Einstein–deSitter universe. Therefore the energy can be written in terms of initial conditions:

$$|E| = -\frac{1}{2}\dot{r}_i^2 + \frac{GM}{r_i}$$

$$= -\frac{1}{2}H_i^2 r_i^2 + \frac{4\pi G}{3}\rho_i r_i^2$$

$$= -\frac{1}{2}H_i^2 r_i^2 + \frac{4\pi G}{3}\overline{\rho}_i (1+\delta_i) r_i^2$$

$$= \frac{1}{2}H_i^2 r_i^2 \delta_i \qquad (2)$$

Here, r_i and $\dot{r}_i$ are the initial radius and velocity of the shell. We assume that these are related through the Hubble's law $\dot{r}_i = H_i r_i$ with H_i as the value of Hubble's parameter at the initial time. Hubble's Law: $\vartheta = H\, r$

$$put\ r = a(t)\, x$$

where $r -$ physical coordinate

$a(t) -$ scale factor

$x -$ comoving coordinate

only scale factor explains expansion or contraction of universe.

Therefore, $\frac{\dot{a}}{a} = H$, at $t = t_o$ then H_o = 70 km/s/Mpc

where 1 Mpc = 3.02 x 10^{22} meters

$\rho_i = \bar{\rho}_i(1+\delta_i)$ is the density of the perturbation and is related to the average density $\bar{\rho}_i$ and density contrast δ_i. Qualitatively, we can see that as compared to the Einstein–deSitter universe, the expansion rate of the shell within the over-dense region slows down at a faster rate until it comes to a halt and then begins to recollapse. The slower expansion leads to a relative increase in the density within the shell as compared to the background universe. At the stage when its radius is maximum, we have |E| = GM/r_{max} and hence, $r_{max} = r_i$ (1 + δ_i) / δ_i ~ r_i / δ_i.

The solution to (1) can be written in a parametric form,

$$r = \frac{1}{2} r_{max} (1 - \cos\theta), \qquad t = \frac{1}{2H_i\delta_i^{3/2}} (\theta - \sin\theta) \tag{3}$$

where we assume that $\delta_i \ll 1$. This is obtained by integrating (1) and substituting for r. We note that the characteristic collapse time for the perturbation is $H_i / \delta_i^{3/2}$ and is smaller for perturbations with a larger initial density contrast. This implies that if we have a perturbation where density contrast decreases as we go to larger radii, the inner shells collapse first and outer regions collapse later.

It is interesting to note that the characteristic collapse time is fairly long – indeed it is of the same order as the age of the universe. In contrast, the collapse of a perturbation of similar density in a static universe is about $\delta_i^{3/2}$

times smaller, i.e., for a $\delta_i \sim 10^{-2}$, the difference is three orders of magnitude if we consider perturbations with the same density. Thus, the expansion of the universe slows down the collapse of perturbations significantly and as a result, the growth of density perturbations in an expanding universe becomes a slow process as compared to its counterpart in a static background.

The solution given above is cyclic in nature where shells collapse to the centre and then rebound to the same amplitude in the other direction. However, it is obvious that most perturbations do not have spherical symmetry. It can also be shown that any departures from spherical symmetry grow rapidly during collapse. Hence, our estimation is likely to deviate more and more from the collapse of real perturbations that happened at a later time. We can capture the physics of key stages during further collapse by realising that in the collapsing phase deviations from a symmetric initial condition grow rapidly; violent relaxation is likely to play an important role to bring the system close to an equilibrium state in a very short time.

In equilibrium state for self-gravitating systems, the virial theorem dictates that we must have 2K + U = 0, where K is the kinetic energy and U is the potential energy of the system. This can be rephrased as 2K + U = 2E − U = 0, and therefore $|E| = GM/2r_{vir}$, where r_{vir} is the radius of the system after it has reached virial equilibrium. Comparing this with the value of energy at the time when the system is at its maximum radius r_{max} , we find that $r_{vir} = r_{max}/2$. Thus, the system relaxes to equilibrium at half the radius of maximum expansion, after which change in its size is not expected, but, the universe continues to expand.

The density contrast for the matter contained within the shell can be written in the following form at any given time:

$$1 + \delta = \frac{\rho}{\bar{\rho}} = \frac{{}^{3M}\!/_{4\pi r^3}}{\bar{\rho}} \tag{4}$$

For the Einstein–deSitter universe, we have:

$$H^2 = \frac{8\pi G}{3}\bar{\rho}$$

where, H = $\dot{a}/a$ is the Hubble parameter. Using the fact that a ∝ $t^{2/3}$, in this case we have H = 2/3t. This gives: $\bar{\rho}$ = $1/6\pi G t^2$ (5)

$$1 + \delta = \frac{9GMt^2}{2r^3} = \frac{9}{2}\frac{(\theta - \sin\theta)^2}{(1-\cos\theta)^2}$$

The perturbation has a density contrast of $9\pi^2/16 - 1 = 4.55$ at the time of maximum expansion.

As discussed above, the perturbation is expected to take one crossing time beyond the stage of maximum expansion to reach close to dynamical equilibrium. Thus, it requires time t(θ = π) to reach virial equilibrium from the stage of maximum expansion. We have already found that the radius at virial equilibrium is half of the radius at maximum expansion. Using these in (4) and (5), we find that the density contrast, at the time it reaches equilibrium, is 168. Thus, the typical over-density of a collapsed virialised halo is 168, i.e., average density inside virialised halos is 168 times the average density of the universe at the time of collapse. Note that for this second calculation we do not use the last equality, as the parametric solution for r is invalid in this regime.

The density of the halo remains constant once it reaches virial equilibrium but the density contrast continues to increase as the average density of the universe continues to decrease.

The discussion so far has focused on the evolution of perturbation due to gravitational interaction. It is interesting to ask what happens to gases during the evolution of the perturbation. As perturbation expands with the universe, clearly gases must cool, and there should be some heating as it collapses after reaching its maximum radius. An implicit assumption here is that the entire evolution is adiabatic and that the gases do not gain or lose energy to any external source or sink. As the expansion of perturbation is the dominant scaling as compared to compression by a factor of two during the collapse, it is clear that the temperature of gases is not very high.

If we assume that after collapse gas inside the virialised halo is supported by thermal pressure, we can estimate the temperature of gas using the expression for virial equilibrium, and by recognising that the kinetic energy of gas is related to its temperature. If the gas temperature is lower than this virial temperature T_{vir}, then the gas must collapse towards the centre of the halo and heat up until the pressure is strong enough to provide the required support. We have:

$$K = <\frac{1}{2}mv^2> = \frac{3}{2}k_B T_{vir} = \frac{GMm}{2r_{vir}}$$

with k_B as the Boltzmann constant and T_{vir} as the temperature in virial equilibrium for a halo of mass M and radius r_{vir}. Thus,

$$T_{vir} = \frac{3GMm}{r_{vir}k_B} \sim 10^7 K(\frac{M}{10^{12} Msun})\,(\frac{r_{vir}}{100kpc})^{-1}$$

where M_{sun} =2×10^{30} kg is the mass of the Sun and 1kpc = 3.08 × 10^{19} m. Performing the above calculation for a typical galaxy cluster with typical mass ~ $10^{14}M_{sun}$, and a radius ~ 1 Mpc, we get,

$$T_{vir} \sim 10^7 K(\frac{10^{14} Msun}{10^{12} Msun})\,(\frac{1000kpc}{100kpc})^{-1}$$

so that

$$T_{vir} \sim 10^8 K$$

Therefore, temperatures at the centres of galaxy clusters can go up to ~ 100 million degrees Kelvin.

2.2 GALAXY CLUSTERS

The universe consists of a large number of gravitationally bound structures known as clusters of galaxies. The most important components of galaxy clusters are (i) a dark matter halo which defines the gravitational potential of the cluster, (ii) the intracluster medium which contains the major fraction of the cluster baryons and consists of hot thermal gas, cosmic rays and magnetic fields, and (iii) galaxies which move in the dark matter potential and contain most of the stars of the cluster.

Galaxy clusters typically have masses ~ 10^{14}-10^{15} M_{sun}, and core temperatures of ~ 10^8 K. As we have described earlier in this chapter, it is possible for infalling gas to get heated to these temperatures. The composition of dark matter is ~ 70%, 15-20% hot diffuse gas and rest 10% are baryons in a galaxy clusters.

Galaxy clusters typically contain thousands of galaxies, but most of the ordinary matter resides in the hot plasma, known as the Intra-Cluster Medium (ICM). Approximately 15-20% of the total mass of galaxy clusters is typically in the form of hot gas that comprises the ICM.

In this part of the chapter, we introduce the properties of galaxy clusters, in the optical, X-ray and radio regimes, and briefly describe their physical properties that lead to these observations at different wavelengths.

2.2.1 OPTICAL OBSERVATIONS OF GALAXY CLUSTERS

Earlier than 1980, all of the discoveries on galaxy clusters were made through optical observations. With the development of X-ray observatories, astronomers were able to probe galaxy clusters in a different part of the electromagnetic spectrum. Coma and Virgo clusters were discovered by Messier and Herschel in 1784-85 as nebulae. It is, however, optical surveys that gave us cluster catalogs. There may be a presence of diffused light and also a small amount of H-alpha emission from a cool gas near the cluster core.

CATALOGS

The catalogs of rich clusters of galaxies was introduced by Abell (1958) and

Zwicky (1961-1968). These catalogs were built on the basis of clusters as increment in the areal number density galaxies on the National Geographic Society - Palomar Observatory Sky Survey.

Both Minkowski and Abell (1963) are limited to northern areas of sky (declination greater than -20° for Abell and -3° for Zwicky). Abell surveyed those clusters in the sky which are isolated from the plane of our Milky way galaxy.

It is not possible to give a definition of a rich cluster based on angular and intensity scales of existence of cluster. So, based on the linear or angular scale and the surface number density inclusion one can define rich cluster. The scale is one of the parameter in order to remove small group of galaxies. Take an example of two galaxies which are very close and represent a large increment as compared to background density of galaxy on a small angular scale. In other words, the richness of galaxies is specified as scale, surface density and the number of galaxies. Once observed number of galaxies is increased then brightness would diminish. For determining the cluster richness, range of magnitudes of the galaxies must be specified. At the end, as distance increases the galaxies grow fainter.

The basis of Abell's nomenclature were as follows:

1. There should be at least 50 galaxies in each cluster with magnitude range m_3 to m_3+2, where m_3 is the magnitude of the third brightest galaxy.
2. These galaxies should be confined in a circle of radius RA=1.7/z minutes where z is redshift of the cluster and RA is abell radius of the cluster. Abell radius of a cluster defined as to measure the compactness of the cluster. It is the distance where cluster members can be counted.
3. The range of redshift should be $0.02 < z < 0.20$.

Out of 2712 clusters 1682 fulfill the above mention criteria in Abell catalog. The rest of them 1030 were discovered by him. Finally, he provided an information on cluster centre position, distance, richness and magnitude of the tenth brightest galaxy m_{10}.

According to Zwicky catalog, the criteria were as follows:

1. The contour would define the boundary of cluster where surface density of galaxy was twice the background density.
2. These maps contained at least 50 galaxies in each cluster with magnitude range m_1 to $m_1 +3$, where m_1 is the magnitude of the first brightest galaxy.

As compared to Abell's criteria, Zwicky catalog are much less strict and contains less rich clusters. Zwicky catalog gives a classification of each cluster based on diameter, richness, redshift and coordinate centre .

REDSHIFTS

Redshift was defined as the magnitude of the tenth brightest galaxy in the cluster. The Abell catalog placed the clusters on group of distance based on above estimation of redshift. By using the magnitudes of the first and tenth brightest galaxies, the redshift was calculated for 1889 Abell clusters. Further, Leir and van den Bergh made better estimation of radius of cluster. Therefore, Zwicky catalog kept each clusters in group of distance based on magnitudes and sizes of the brightest cluster galaxies.

RICHNESS

Richness defination doesn't mean to define any galaxy in the cluster because of the presence of background galaxies. It means how many galaxies are in a cluster. It is a concept of statistics, based on the measure of the number of galaxies in the cluster. It can be defined in such a manner that it should not dependent on cluster shape and distance.

During 1961-68, Zwicky defined richness of cluster as visibility of total number of galaxies on the red sky survey plates. Also, background galaxies is removed from the richness. It shows richness not independent of redshift of cluster. As the magnitude of the first brightest galaxy is away from the limit of plate, only broader range of magnitude is incorported for close by clusters.

Further, look at the neighbourhood of the clusters where largest area is added because the point which has gone from the cluster would be double of background is equivalent to surface density.

In 1958, Abell splited the clusters into groups based on the richness and used the basis that distance is independent. That means, range of magnitude and area do not change with redshift. There would be a little relation between richness and distance in this catalog. Statistically, concept of richness is benefit but carefully to study the individual clusters.

LUMINOSITY FUNCTION OF GALAXIES

In a cluster, the luminosity function assigns a number to the luminosities of galaxies. The integrated luminosity function N(L) is the number of galaxies with luminosities greater than L, while the differential luminosity function n(L)dL is the number of galaxies with luminosities in the range L to L + dL. Obviously, n(L)= - dN (L)/ dL. These functions are often defined in terms of galaxy magnitudes where m is proportional to -2.5 $\log_{10}$(L).

For most galaxy clusters, n(L) is well described by the empirical Schechter function (Schechter, 1976),

$$n(\mathrm{L}) = \left(\frac{n^*}{L^*}\right)\left(\frac{L}{L^*}\right)^{\alpha} exp\left(-\frac{L}{L^*}\right)$$

The parameter L* is a characteristic luminosity. Above L*, the distribution decreases exponentially. The normalization of the distribution is given by n*, and the slope of the distribution for faint (low L) galaxies is given by alpha.

GALAXY COLORS

Multiple filters and imaging is the technique to measure galaxy colors. Color is linked with type of galaxy and their star formation rates. Blue color in spiral galaxies indicate a young stellar population and active star formation whereas elliptical galaxies are red in color as consist of old stellar population with slightly star formation. These red galaxies dominate in the central region of galaxy cluster. Some fraction of spiral galaxies in a cluster increases with distance from the center with decreasing galaxy density. On the other hand, some sort of elliptical galaxies is higher in the central regions where the galaxy density is higher. This is known as morphology-density relation. As a result of this relation, the small part of spiral galaxies decreases with cluster richness, since the galaxy number density is higher in rich clusters. The different types of galaxies have different luminosity functions. Such a development in galaxy population from poor to rich clusters also affects the luminosity function of clusters.

When plotting the color vs magnitude graph of a galaxy cluster, the red galaxies occupy a very narrow range of color, a phenomenon known as the red sequence (Bower et al., 1992). Interestingly, all cluster red sequences are very similar at a given redshift i.e. galaxies in different clusters that have the same redshift and luminosity are nearly the same color. In order to remove foreground galaxies in cluster surveys (e.g. Gladders & Yee, 2000), it is possible to use this similarity to estimate cluster redshifts (a type of photometric redshift). It appears that the red sequence is in place for clusters out to redshifts of z ~0.5 (Papovich et al., 2010; Hayashi et al., 2011), and possibly even out to z = 3 (Kodama et al., 2007; Doherty et al., 2010), which makes it an invaluable tool for detecting clusters in optical and infrared surveys out to intermediate redshifts.

GALAXY VELOCITIES

Spectroscopic observations of galaxies in clusters also provide measurements of their radial velocities, with typical values of v ~ 1000 km/s. The galaxy velocity distribution for a relaxed cluster can be fitted with a Gaussian, exp (-(v_r - < v_r >)^2/2 σ_r^2), which then defines the galaxy velocity dispersion, s_r (Voit, 2005). Ellipticals have a relatively low-velocity dispersion that does not vary much with distance from the cluster center, whereas spirals have a higher velocity dispersion which increases towards the cluster center as discovered by Biviano et al. (2002). Measurements of galaxy velocities are useful for several reasons. First, galaxies which are not cluster members can be identified as outliers on the Gaussian distribution, helping to minimize projection effects. Second, any models that describe galaxy evolution in clusters must be able to account for the observed velocity dispersions. Third, as initiated by Zwicky in 1933 (Zwicky, 1933), the velocity dispersion can be used in conjunction with the virial theorem to obtain the total cluster mass. As mentioned previously, this is needed to constrain cosmological parameters using clusters.

2.3 X-RAY OBSERVATIONS

There is a gas in galaxy clusters is at temperatures of a million kelvins. Further, gas consists of particles with high energy. As the cools down it emits X-rays. This emission is a combination of bremsstrahlung and emission lines from iron and other heavy elements. This shows that the intracluster gas must emit from galaxies in the cluster. Recently, Einstein X-ray satellite indicates that intracluster gas cool down in some cluster of galaxies.

The word bremsstrahlung originates from a German word and means braking radiation. It defines as any charged particle is accelerated when deflected by another charged particle in the coulomb field. Therefore, intensity of this radiation is proportional to square of the gas density.

Spectral lines are the consequences of interaction between atoms and photons. Each element has its own characterstics emission and absorption line, therefore, the analysis of line emission from the gas allows the determination of its chemical characterstics.

When we observe galaxy clusters, it is possible to produce an X-ray image and also count the number of photons per energy, in other words, a spectrum. From the study of X-ray emission from the gas it is possible to derive some of the cluster properties.

As an example, the Virgo cluster has a center where galaxy M87 and around that region X-ray emission detected in 1966.

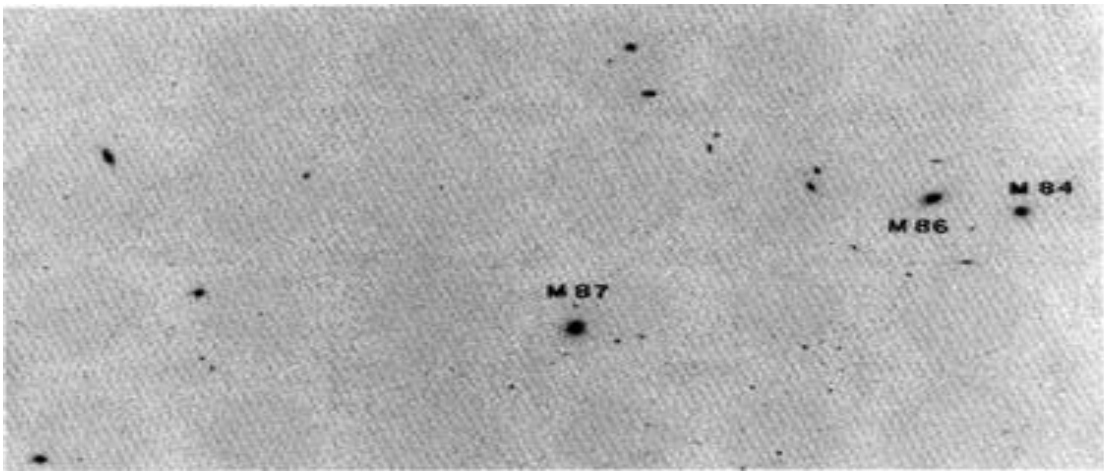

Figure 2.1 Optical photograph from the Palomar Observatory Sky Survey of Virgo cluster of galaxies

M87 is also identified as a X-ray source. Further, there were detections of X-ray sources in Coma and Perseus clusters. Thus, all these galaxies / clusters of galaxies are sources of astronomical X- ray emission.

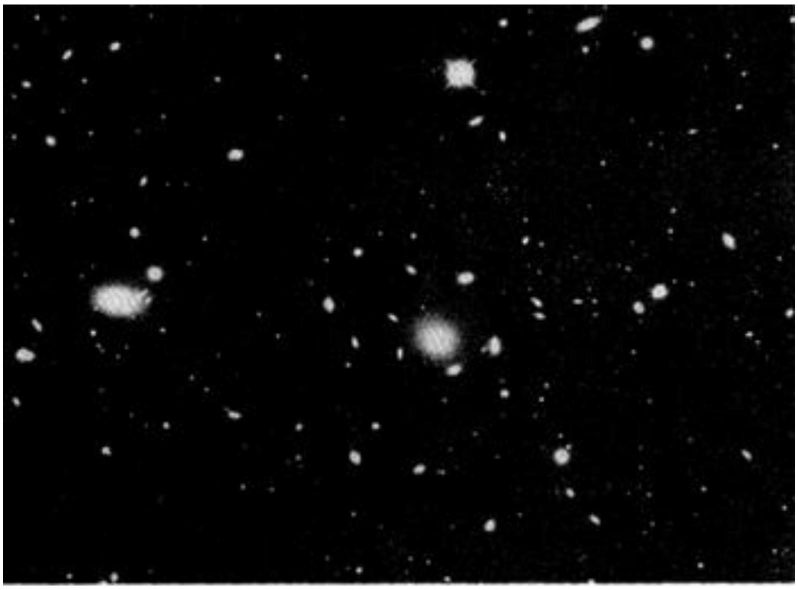

Figure 2.2 Optical photograph of Coma cluster. Credit: the national optical astronomy observatories.

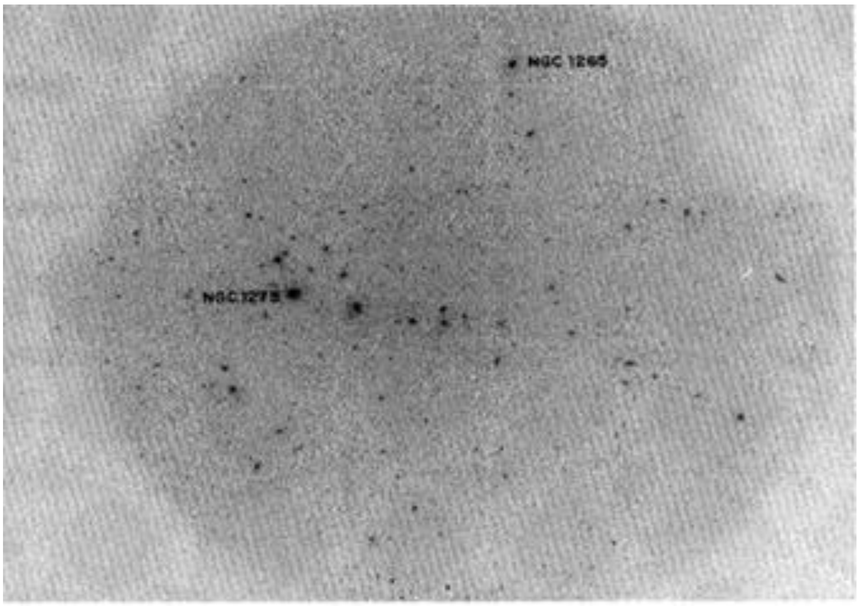

Figure 2.3 Optical photograph of Perseus cluster of galaxies. Credit: Strom and Strom (1978b)

2.3.1 LUMINOSITY AND ENERGY FLUX

Clusters of galaxies are luminous X-ray sources, with X-ray luminosities ranging from 10^{43} to 10^{46} erg s^{-1}. The luminosity is the amount of energy emitted by a source each second. For clusters of galaxies, the X-ray luminosity is the amount of energy in the form of X-rays emitted by the gas each second.

The X-ray luminosity is calculated from the observed flux in the instrument's energy band. The flux is the energy received per unit of area of the detector each second, or in other words, it is the luminosity per unit area. The emission of electromagnetic radiation has intensity and wavelengths related to its temperature.

The energy flux and X-ray luminosity of clusters are computed by fitting a model to the observed X-ray spectrum for a given redshift and energy range.

2.3.2 THE GAS DENSITY PROFILE

Assuming an isothermal spherical gas cloud in hydrostatic equilibrium and assuming the volume density of galaxies follows a so called King profile, the density profile of X-ray emitting gas can be approximated by an isothermal β model,

$$\rho_{gas} = \rho_0 \left(1 + \left(\frac{r}{R_c}\right)^2\right)^{\frac{-3\beta}{2}}$$

where ρ_{gas} is the density of the gas as a function of the cluster's projected radius r, R_c is the core radius and ρ_0 is the density at the cluster's center. The values of β and R_c are obtained by analysis of the X-ray surface brightness profile.

2.3.3 SURFACE BRIGHTNESS PROFILE

X-ray image analysis allows the determination of the X-ray surface brightness profile. Assuming that the hot gas is isothermal leads to a β model for the cluster's brightness profile,

$$S(r) = S_0 \left(1 + \left(\frac{r}{R_c}\right)^2\right)^{-3\beta+\frac{1}{2}} + \mathrm{C}$$

where $S(r)$ is the X-ray brightness as a function of the projected cluster's radius r. S_0, R_c, β and C are free parameters in fitting the model to the X-ray brightness profile. In general the X-ray surface brightness profile is well approximated by the β model.

2.3.4 TEMPERATURE OF INTRA-CLUSTER MEDIUM (ICM)

The temperature of the ICM is closely related to the depth of the cluster's potential well. The gas trapped by a cluster's potential well presents temperatures of the order of 10^7 K.

The average temperature T of the gas is derived by fitting a model to the observed X-ray spectrum. The average temperature is a free parameter of the model that is varied to produce the best fit to the observed spectrum. The assumption of isothermality of the intra-cluster medium is not always valid as some clusters can host cool cores. The result of a cluster's average temperature including cool cores will be lower than the average temperature excluding a core region. We are interested in the average temperature of gas that is relaxed and in hydrostatic equilibrium. That is not the case of a core region hosting cooling flows. Studies of temperature profiles in clusters also show that the temperature generally declines outside the central regions but shows that despite these variations a single integrated temperature, excluding the core regions, remains a good approximation for the total mass.

2.3.5 METAL ABUNDANCE

The metal abundance can be determined from the emission lines of heavy elements in the spectra. A emission line is a bright line in a continuous spectrum resulting from an excess of photons. Emission lines are very specific for each element and can be used to identify the chemical composition of the gas.

X-ray spectroscopy is a powerful tool for analyzing the metal abundance of the ICM. Studies of the chemical abundances of nearby clusters yield a typical mean value for the metallicity in clusters of approximately 0.3 of solar metallicity.

2.4 RADIO COMPONENTS OF GALAXY CLUSTERS

Clusters of galaxies are the nodes of the sheets and filaments where most galaxies reside, and they grow and evolve as matter containing galaxies and groups inflows and as clusters of galaxies merge. Understanding the complex processes and timescales in this evolution is critical to understanding the origin of the state of clusters of galaxies.

Diffuse non-thermal radio emission in clusters of galaxies of ~Mpc size not associated with galaxies, when close to the centres of clusters, are called *radio halos*, and when at or close to the peripheries of clusters are called *radio relics*. These are due to relativistic electrons and magnetic fields in the ICM and have steep synchrotron spectra ($S \alpha \nu^{-\alpha}$, $\alpha > 1.1$), and radio relics have even steeper spectra compared to radio halos. Turbulent reacceleration of electrons in the ICM has been proposed as a model for radio halos; whereas acceleration of electrons at outgoing merger shocks are believed to be responsible for radio relics (eg. Ferrari et al 2008). About 35% of clusters with X-ray luminosities greater than 5×10^{44} ergs/s have radio halos (Venturi et al

2008). However, among clusters that are dynamically disturbed, about 3/4ths exhibit radio halos (Cassano et al 2010).

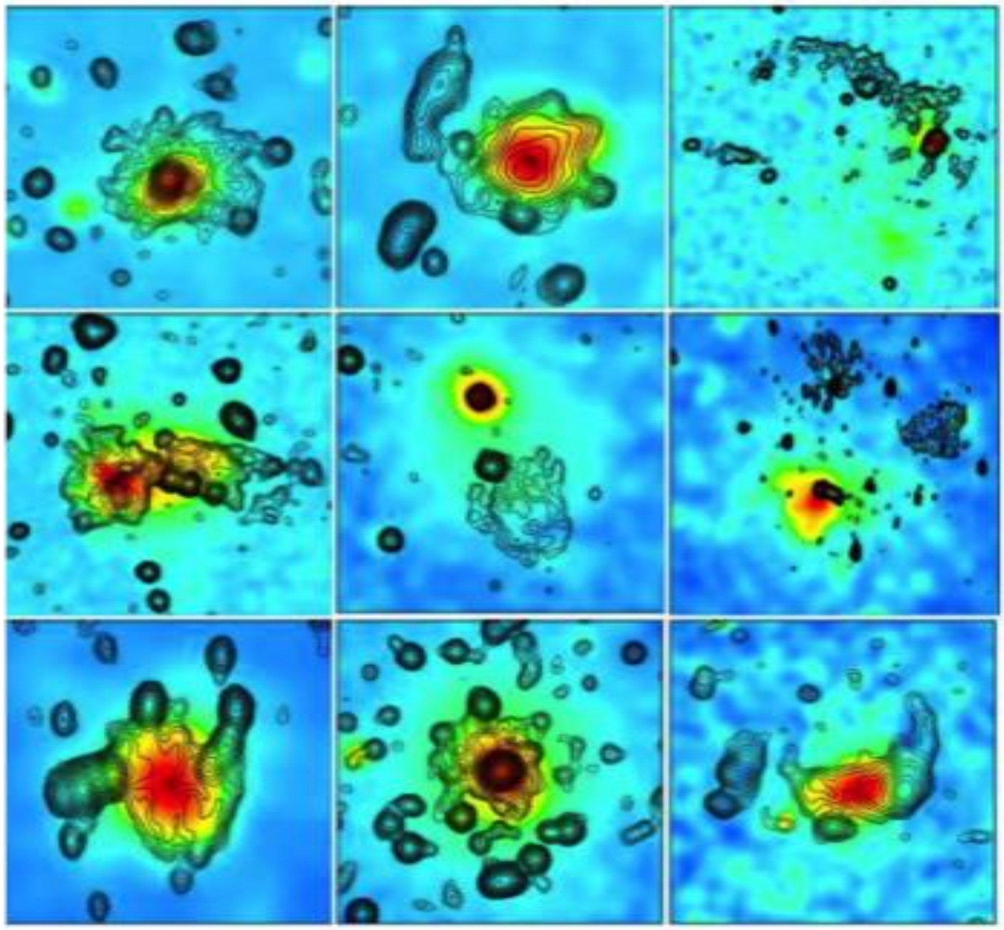

Figure 2.4: Collection of galaxy clusters showing several types of radio emission, shown in con- tours, overlaid onto the X-ray emission, shown in colors. Clusters are (from left to right and from top to bottom) A 2219 (halo, Bacchi et al., 2003), A 2744 (halo + relic, Govoni et al., 2001), A 115 (relic, Govoni et al., 2001), A 754(complex, halo plus relic, Bacchi et al., 2003), A 1664 (relic, Govoni et al., 2001), A 548b (relic, Feretti et al., 2006), A 520 (halo, Govoni et al., 2001), A 2029 (mini-halo, Govoni et al., 2009), RXCJ1314.42515 (halo plus double relics, Feretti et al., 2005). Adopted from Feretti et al. (2012).

Synchrotron emission from cluster of galaxies gives information that diffuse radio emission are up to Mpc-scale. There are three radio components, as mentioned above: halos, relics and mini-halos. The first two are studied in this thesis. Synchrotron emission happens in the presence of relativistic electrons (~ GeV) and weak magnetic fields (~ μG) in the intra-cluster medium, with hot thermal plasma emitting X-rays. In the last 30 years people have known about radio halos and relics but their origin is as yet debated. The short radiation lifetime of the emitting electrons and their Mpc size pose the main difficulty in explaining extended emissions. It requires re-acceleration of the electrons. Cluster merger plays a key role where shocks correspond to relics and halos formation is due to turbulence in the ICM, which further amplifies the magnetic field. Some galaxy clusters have double relics and some have both halos and relics; see the figure below.

2.4.1 RADIO RELICS

Diffuse emission features have been observed in the outskirts of clusters of galaxies – these are known as radio relics. Some characteristics of these radio relics are: low surface brightness, steep integrated radio spectrum ($\alpha \geq 1$, $S \propto \nu^{-\alpha}$) and a medium-to- high level of polarization (upto 40%, see the below fig).

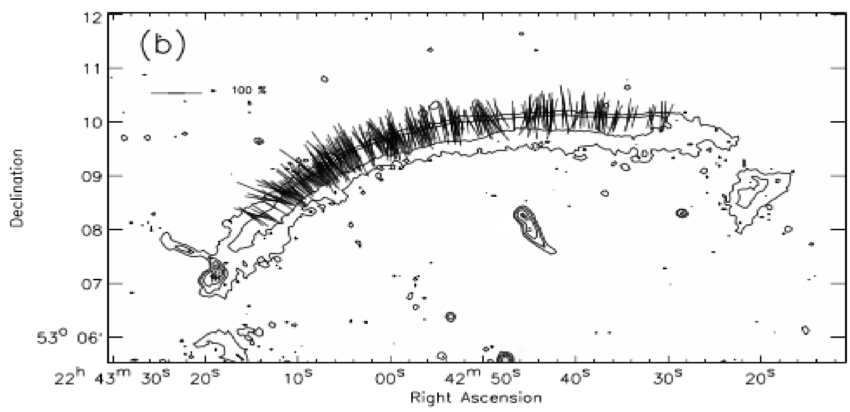

Figure 2.5: The radio relic in CIZAJ2242.8+5301: contours represent the total intensity emission obtained with thw GMRT at 610 MHz. Superimposed bars represent the polarization electric field vectors obtained with the VLA at 4.9 GHz. Adopted from van Weeren et al. (2010).

Relics are observed in both merging and cool-core systems toward the periphery of clusters. They are detected up to redshift $z \sim 0.4$. The low number of high-redshift relics could be due to increasing relevance of inverse compton losses with z. (Feretti et al. 2012). Giovannini et al. (1999) showed that the occurrence of relics in a sample from the NVSS is higher in clusters showing a high X-ray luminosity. Relics are further subdivided into three classes: radio gischt, radio phoenices and AGN relics (see Kempner et al., 2004).

Radio gischt or giant radio relics are large extended arc-like sources, synchrotron emission from electrons re-accelerated in merger or accretion shocks, through diffusive shock acceleration (DSA; Ensslin et al., 1998; Kang Ryu, 2011). For example giant radio relic has been observed in the galaxy cluster CIZA J2242.8+5301.

Radio phoenices are smaller structures formed as a result of the re-energization, via adiabatic compression. The adiabatic compression is triggered when a merger or accretion shock passes through such a faded relic radio galaxy (Enlin Gopal-Krishna, 2001; Enlin Bruggen, 2002). An example of a radio phoenix has been found in the galaxy cluster A2443.

AGN relics are fossil radio galaxies where the AGN switched off more quickly and no re-energization occurred.

Radio relics have been classified based on morphology, viz. elongated vs. roundish. In first approximation, elongated relics correspond to the giant radio relics of Kempner's classification, while roundish relics correspond to radio phoenices. The roundish sources are more concentrated towards the cluster center, while elongated relics are mostly located between 0.5 and 1.5 Mpc from the center, up to a distance of 3 Mpc (see Fig. 2.6 left panel). Moreover, elongated relics show the spectral index α in the range -1.0 to -1.6, with an average value of -1.3, while spectral indices of roundish relics span a larger range of values, -1.1 to -2.9, with an average value of -2.0 (see Fig. 2.6 right panel).

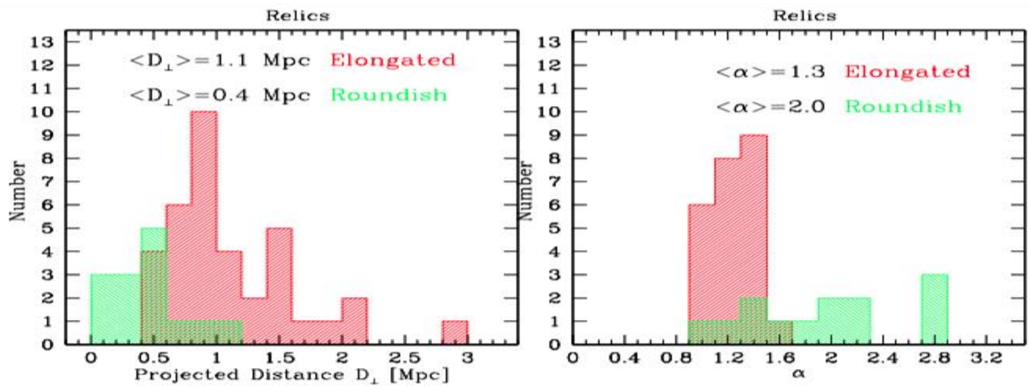

Figure 2.6: Left panel: Distribution of relics according to their projected distance from the cluster center. Right panel: Spectral index distribution of relics. Adopted from Feretti et al. (2012).

A2256 has extended giant relics with central halos in its clusters (Clarke Ensslin, 2006). Moreover, one can see double and symmetric relics located in the oppo- site sides of cluster A3667 (Rottgering et al., 1997; Johnston-Hollitt et al., 2002). Further, some unique objects can also be found in Feretti et al. 2012. By Hugoniot-Rankine conditions, the presence of a shockfront at the location of radio relic has been proved though X-ray observations (Markevitch et al., 2002). However, the detection of shocks in the X-ray gives the information that relics are observed in the outskirts of clusters where low density of electrons can be found.

2.4.2 RADIO HALOS

The term radio halo is used to indicate low-surface brightness extended radio sources permeating the volume Mpc^3 of clusters. The radio morphology is generally irregular and while detection of polarized emission connected with a radio halo have been found in the galaxy clusters A2255 (Govoni et al., 2005; Pizzo et al., 2011) and MACS J0717.5+3745 (Bonafede et al., 2009), radio halos have either low percentage polarization, or are unpolarized.

This absence of significant observed levels of polarization, together with their morphological connection with the thermal X-ray emission suggest that the relativistic plasma that generates the synchrotron radiation occupies a large fraction of the volume filled by the hot X-ray emitting ICM.

Detection of Radio halos is difficult because of their low-surface brightness, steep spectra and large angular size. The occurrence of halos in the NVSS sample increases with increasing X-ray luminosity of the host cluster (Giovannini et al., 1999). The GMRT Radio Halo Survey (Venturi et al., 2007, 2008) has provided a significant improvement of the statistics in reference to radio halo occurrence. This survey consists of 610 MHz observations of a complete sample of 50 X-ray-luminous galaxy clusters in the redshift range of 0.2 - 0.4 (with L_X~$5x10^{44}$ erg/s, taken from the REFLEX and the extended BCS catalogues, Bohringer et al., 2004; Ebeling et al., 1998, 2000).

Large-scale synchrotron emission at the level of presently known radio halos was found only in 30% of the selected clusters (Venturi et al., 2008), confirming that this fraction depends on the cluster X-ray luminosity (Cassano et al., 2008). Figure 6 (from Brunetti et al., 2009) shows the distribution of the GMRT galaxy (blue) and other clusters hosting giant radio halos from the literature, in the plane of X-ray thermal luminosity in the energy range 0.1 - 2.4 keV (L[0.1-2.4]keV) vs the non-thermal radio power at 1.4 GHz (P1.4GHz). The distribution follows a bimodal behavior, with radio-halo clusters tracing a $P_{1.4}$ - L_X correlation and radio-quiet clusters (without radio halo; upper limits indicated by arrows in below figure) clearly separated. Since the X-ray luminosity is directly related to the cluster mass, the $P_{1.4}$ - L_X correlation suggests that gravity provides the reservoir of energy to generate the non-thermal components in the ICM.

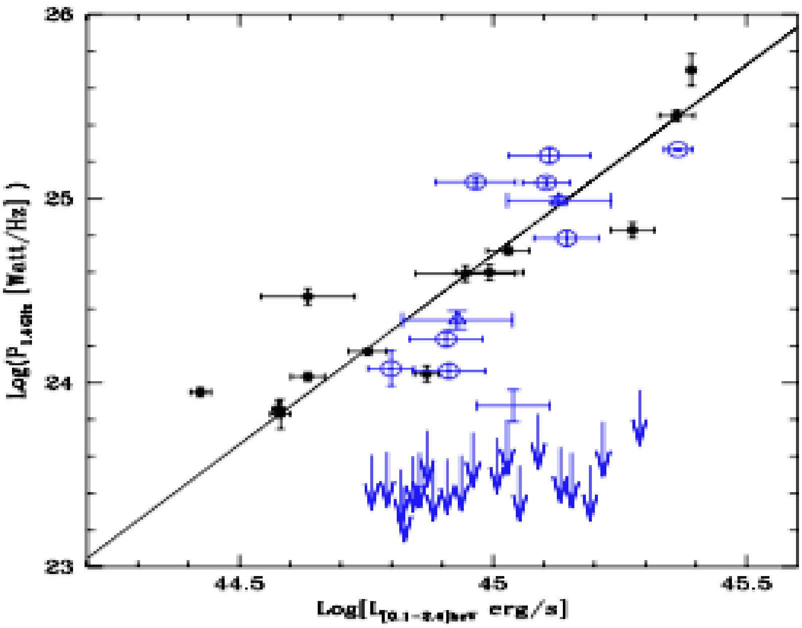

Figure 2.7: Distribution of GMRT galaxy clusters (blue) and of other radio-halo clusters from the literature (filled black symbols) in the $P_{1.4}$-L_X(0.1-2.4 keV) luminosity plane. Empty circles mark giant radio halos from the GMRT sample, empty triangles mark the two mini-halos in cool-core clusters from the GMRT sample. The cross marks the position of RXJ1314, and arrows mark upper limits of GMRT clusters with no evidence of Mpc- scale radio emission. The solid line gives the best fit to the distribution of giant radio halos. Adopted from Brunetti et al. (2009).

Brunetti et al. (2009) estimated that the life-time of radio halos is ~ 1.3 Gyr. The time interval that clusters may spend in the empty region is ~ 180 Myr and the corresponding time-scale for suppression of the cluster-scale synchrotron emission from the level of radio halos to that of radio quiet clusters is roughly 90 Myr.

However, radio halos in under luminous X-ray clusters, i.e. outside the correlation between radio power and X-ray luminosity, have been found in a few cases (Giovannini et al., 2009, 2011; Brown et al., 2011).

We point to Table 1 of Feretti et al. (2012) for a collection of known radio halos updated to September 2011.

It is also known that the spectra of diffuse emission in some galaxy cluster mergers show a “break”, i.e. the spectra steepen at a certain frequency. Brunetti et al. (Nature, 2008) have shown exactly this for the spectrum of diffuse emission from one cluster merger – in this case, the break occurs at ~ 1.4 GHz. This break in the spectrum, or a steepening of the spectrum, is expected to occur at frequencies ~1-2 GHz. The exact frequency of this break or steepening depends on the total amount of energy associated with the cluster merger. The higher the energy of the cluster merger, the higher the frequency of this break or steepening. For this reason, the frequency of the break in the spectrum is inversely proportional to the age of the merger.

CHAPTER 3

RADIO INTERFEROMETRY

In order to estimate the amount of diffuse emission from large structures like galaxy clusters, it is necessary to make images which have both adequate resolution as well as a large-enough field-of-view, so that the entire structure is present in the image. If the resolution is limited, the morphology of the diffuse emission cannot be determined. On the other hand, if the field-of-view is limited, the entirety of the diffuse emission cannot be imaged, and we cannot estimate the total diffuse emission from the galaxy cluster.

Therefore, it is necessary to use a radio telescope that can provide both a large-enough field-of-view, as well as adequate resolution. In order to get adequate resolution, it becomes necessary to use multiple dishes instead of a single, large dish, and to interfere signals from these dishes. We explore the relationship between the image on the sky and the output of this radio interferometer. We also summarize how to extract the image from the output of a radio interferometer. These are the techniques we have used in order to extract information about diffuse radio emission from galaxy cluster mergers in this thesis.

Additionally, it turns out that while radio interferometers are able to provide resolution, they are unable to record the total power from an extended object, because of a missing “zero-spacing”.

To sum up, we present the details of

i) An introduction to radio interferometry; in particular, the relationship between sky image and visibility.
ii) An overview of analysis of radio interferometry data analysis

Having gone through the construction and use of a 21 cm horn and basic receiver system, we used a similar system (though simpler), as described below.

3.1 VISIBILITY AS A FUNCTION OF INTENSITY PATTERN ON THE SKY

Consider two horn antennas/radio telescopes separated by a distance B. These define one baseline. Let them be oriented as shown to receive a signal from an extended object in the sky. Then, consider a single point on the extended object or source, P. Let the distance from P to each of the telescopes be d_1 and d_2. The reason we consider a single point on the source is that rays originating in different parts of the source are not mutually coherent, i.e. their relative phases are random. So it doesn't make sense, for instance, to calculate the net electric field at one telescope due to rays from the object as a whole. We do need to make an image of the whole object, however, and for this reason, we scan across it with our baseline. Mathematically, this is equivalent to calculating the net field and then integrating over the source.

Let (x, y) be the co-ordinate system on the source. Let $I(x, y)$ be the intensity as a function of position on the source and let $E(x, y)$ be the electric field due to the source on both the antennas. D is the distance between the telescopes and the source.

There is a time delay of $\frac{d_2 - d_1}{c}$ between the signals received by the two telescopes. The electric fields at the two telescopes can be written as:

$$E_1 = E(x, y)\, e^{i\omega\left(t - \frac{d_1}{c}\right)}$$

$$E_2 = E(x, y)\, e^{i\omega\left(t - \frac{d_2}{c}\right)}$$

Consider now the product of these two electric fields. In brief, it is only by multiplying the two signals that we can get interference.

$$E_1 E_2^* = E^2\,(x, y)\, e^{\frac{i\omega\,(d_2 - d_1)}{c}} = I(x, y)\, e^{\frac{i\omega\,(d_2 - d_1)}{c}}$$

The two distances d_1 and d_2 can be written as

$$d_1^2 = \left(x - \frac{B}{2}\right)^2 + y^2 + D^2$$

$$d_2^2 = \left(x + \frac{B}{2}\right)^2 + y^2 + D^2$$

Clearly, $\frac{B}{D} << 1$; in other words, the distance between us and the source is much greater than the length of the baseline. We assume that $\frac{x}{D}, \frac{y}{D} << 1$, or that the size of the source is much smaller than the distance between us and the source. Then,

$$d_2 - d_1 \sim \frac{Bx}{D}$$

which implies that

$$E_1 E_2^* \sim I(x,y)\, e^{\frac{i\omega\, Bx}{c\, D}} = I(x,y)\, e^{i2\pi\frac{Bx}{D\lambda}}$$

We would like to work in terms of angles, so we change variables to $\alpha = \frac{x}{D}$, $\beta = \frac{y}{D}$ so that

$$E_1 E_2^* \sim I(\alpha,\beta)\, e^{i2\pi\frac{B\,\alpha}{\lambda}}$$

However, the basis (α,β) is relative to the source, and not the observation plane or the sky. We therefore slip the formalism into something more comfortable and convenient – the equatorial co-ordinates, thus:

$$\alpha = \cos\theta x' + \sin\theta\, y'$$

$$\beta = \sin\theta\, x' + \cos\theta\, y'$$

and then define

$$u = \frac{B}{\lambda}\cos\theta$$

$$v = \frac{B}{\lambda}\sin\theta$$

and integrate over x' and y' and to get

$$\iint E_1 E_2^*\, dx'\, dy' = \iint I\,(x', y')\, e^{i2\pi(ux'+vy')}\, dx'\, dy'$$

But the right side of the equation is just the Fourier transform of $I\ (x', y'\ )$. The left hand side is what we call visibility.

In this discussion, we ignored the effect of the diffraction patterns of the telescopes /
antennas themselves. We can introduce it in equations above to get

$$\iint E_1\, E_2^*\ dx'\, dy' = \iint A\ (x', y')\ \ I\ (x', y')\, e^{i2\pi(ux'+vy')}\, dx'\, dy'$$

We do not need to make the small-sky patch approximation to get a useful result, though. It just so happens that in this approximation, the output of the interferometer, the "Visibility", or as we defined it elsewhere, the "Mutual Coherence Function" happens to be the Fourier transform of the intensity pattern on the sky. If the approximation is relaxed, the visibility becomes a general mathematical transform of the intensity pattern, and not necessarily a Fourier transform.

The main idea is that one baseline, i.e. one pair of antennas gives us a single point in the Fourier transform of the intensity pattern on the sky, convolved, of course, with the beam.
To get more distinct points, we need more baselines, each with a different length or orientation. The most general form of $E_1E_2^*$ is then

$$\iint E_1\, E_2^*\ dx'\, dy' = \iint A\ (x', y')\ \ I\ (x', y')\, e^{i2\pi(\boldsymbol{u}.\boldsymbol{x})}\, dx'\, dy'$$

(x' and y' are really θ and ϕ on the sky) where **u** is the vector $\mathrm{u}\hat{u} + \mathrm{v}\hat{v}$ and the unit vectors $\hat{u}$ and $\hat{v}$ span what is called the "u-v" plane, which is the fourier-transform equivalent of the θ-ϕ plane on the sky. What this means is that visibility, which is a function of u and v, i.e. $V = f(u, v)$ is the fourier transform of the image (or intensity pattern) on the sky (for small patches) i.e.

$$V(u, v) = F\ (I(\theta, \phi))$$

which is exactly what the equation says above.

Then, to find an expression for |**u**|, consider: $|\mathbf{u}| = \frac{B}{\lambda}$ that is, |**u**| ∝ the baseline length. For the same baseline, though, a different orientation will give us the same $|\mathbf{u}|$ but different values of u and v . What this means is that if we were to track a single patch on the sky and rotate the instrument w.r.t. the patch, we will be observing at all those points in the uv plane that lie on a circle with the radius $|\mathbf{u}| = \frac{B}{\lambda}$

3.2 ANALYSIS OF DATA FROM INTERFEROMETRIC ARRAYS

Having described the details of the output of an interferometer, and its relationship with the sky image, we now summarize the data analysis process for interferometric data.

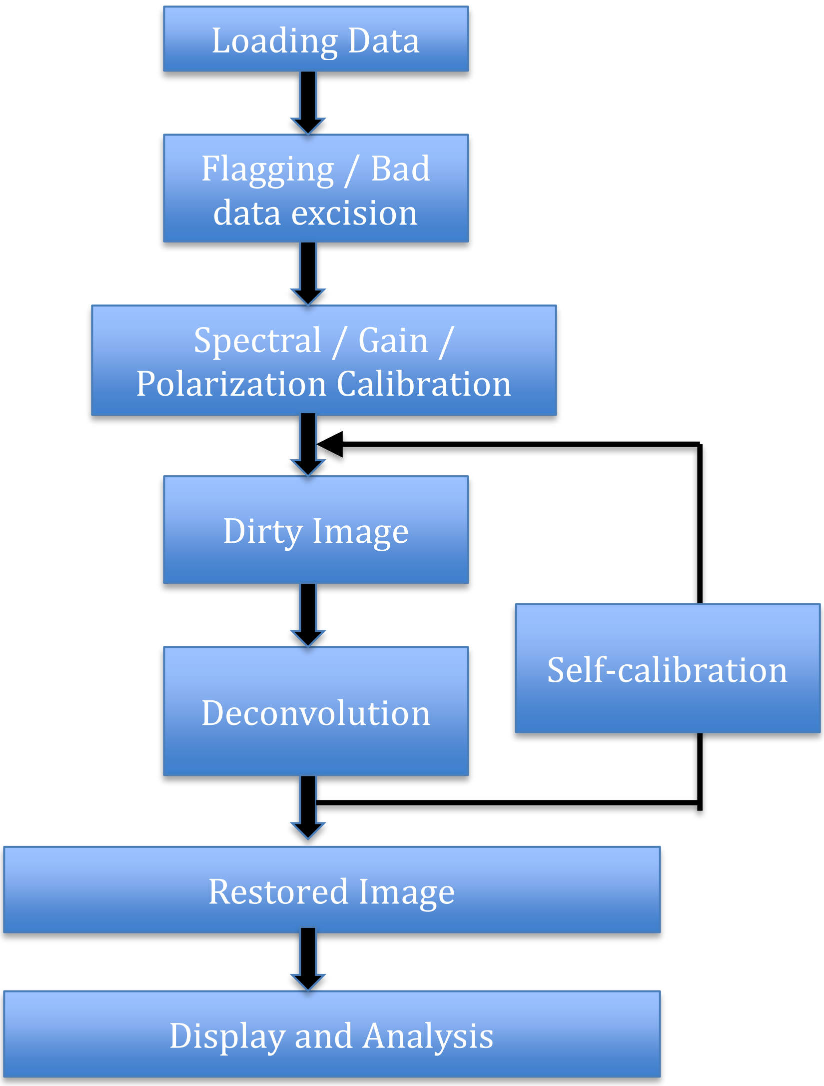

Figure 3.1: A schematic of the general data analysis strategy adopted for radio observations.

Standard data analysis packages are available for reducing and analyzing data from radio observatories; these include (but are not limited to): AIPS (Astronomical Image Processing System), CASA (Common Astronomy Software Applications) and MIRIAD (Multichannel Image Reconstruction Image Analysis and Display). All of these packages employ 'tasks' for specific operations performed on the data. While these packages were each developed by users of a particular facility, each package does allow analysis of data from other observatories as well.

While AIPS has been used for decades as the standard package for both VLA (Very Large Array) and GMRT (Giant Metrewave Radio Telescope) data, MIRIAD has been used by ATCA (Australia Telescope Compact Array; ATNF). Different parts of our dataset are from observations made at JVLA, GMRT and ATCA; we therefore used both CASA and MIRIAD in the analysis of our data.

We describe below the general procedures for analyzing radio datasets. In general, each step has several sub-steps, most of which are outlined below:

1. Loading Data: The format of data available from almost all radio observatories is either FITS (Flexible Image Transport System), or a variant of FITS (MIRIAD, for instance, uses RPFITS, and the conversion between FITS and RPFITS is done through a task). This data needs to be loaded in a format that can be read and manipulated by the software package. Additionally, headers in the data are read and recognized, so that different parameters of the observations, e.g. the object being observed, the position of the object, the total observation time, the system temperature during the observation, atmospheric conditions during the observations are read and recognized, so that they can be displayed conveniently later, as required.

2. Flagging: The most obvious kind of data flagging is that of spurious signals from various telescope instruments, as well as high-level radio frequency interference (RFI) – these may appear as spikes in the data, and

their removal can be automated using tasks in the software packages, depending on their amplitude. Several stages of flagging are usually needed – this depends on both the telescope site, as well as the frequency of observation, with the lowest frequencies obviously containing the greatest amounts of RFI. It may also be necessary to flag data based on known atmospheric disturbances that are known to disrupt observations. Additionally, for certain objects that may be too low in the sky, antennas can 'shadow' each other; this can be checked using the shadowing diagrams for a particular observatory, and the corresponding data for the relevant pairs of dishes can then be flagged.

3. Calibration: This is the most critical analysis step, since it decides how well data can be analyzed and interpreted – any errors made in calibration carry over as systematic effects in the image. Multiple steps are involved in calibration; these are outlined below. The basic idea in calibration is to estimate the real or complex factors that the data should be weighed with, in order to

a. Bandpass calibration – This depends on the spectral response of the instrument, and this calibration is done through observation on a bandpass calibrator, which is a bright source, with either a flat or known spectral response in our operating frequency band. Bandpass calibration is usually done before and after observations of the target source.
b. Amplitude calibration – This is needed to set the flux scale for target observations, i.e. to enable us to find an appropriate factor by which the brightness must be adjusted.
c. Phase calibration – For interferometric observations, is it critical to ensure that the relative phases of all the dishes in the radio interferometer remain constant. However, for various reasons, these relative phases drift with time, causing spurious phase differences between pairs of dishes where none exist in the radiation being received from the target source. In order to ensure that these relative phases remain stable, periodic observations of a bright source are made – one of the requirements for such a source to act as a phase calibrator is that its location should be close to the target source. This would ensure that the adjustments needed in phases account for phase

variations introduced by the atmosphere accurately. In order to perform phase calibration, the values of the phase differences between pairs of dishes are interpolated between successive observations of the phase calibrator. The complex factors or gains are then applied to the data. Apart from the above three kinds of calibrations applied to the data, there is another form of calibration – Self-calibration – which is also applied; this would be discussed below.

4. Dirty Image: After the appropriate complex gains have been applied to the visibilities as part of calibration described above, an inverse fourier transform can be applied on the visibility data, in order to produce what is known as a 'Dirty Image'. The dirty image is effectively the true sky image convolved with the inverse fourier transform of the visibility sampling function that the radio interferometer effectively applies on the sky image. For this reason, it is necessary to deconvolve this dirty image, as discussed below.

5. Deconvolution: As mentioned above, the sky image is effectively convolved with the inverse fourier transform of the visibility sampling function – this inverse fourier transform has a 2-dimensional sinc-function appearance, implying that it effectively 'smears' the amplitude of all sources over the field-of-view (FOV). In order to deconvolve, the following steps are followed by the deconvolution task:

a. The brightest pixel in the image is searched
b. This pixel is then convolved with the inverse fourier transform of the visibility sampling function – this is then subtracted form the image, having noted the pixel's position and brightness
c. The process above is repeated until the residual image brightness is close to the noise level
d. The position and brightness of the pixels then provide a 'component image', i.e. a position of all the sources in the sky that have been detected by the radio telescope

6. Restored Image: After the deconvolution process above, the component image is convolved with the synthesized beam of the radio telescope, in order to yield a restored image.

7. Self calibration: Before making a final restored image, however, another round of calibration is needed for the following reason. The sum of all phase differences for all pairs of dishes for any radio telescope should be exactly zero. However, due to phase drifts, this is not always the case. These phase variations cause systematic distortions and other effects in the restored image. In order to correct for these phase variations, an iterative calibration scheme is followed. First, the relative phases of the deconvolved visibilities are changed in order to reduce these phase variations, and the dirty image is reformed, and deconvolved again, using the phase-adjusted visibilities. The self-calibration algorithm uses the source to calibrate the antenna based complex gains. Self-calibration steps can be repeated as long as there is a significant improvement in the signal-to-noise ratio, as well as a decrease in the noise rms.

These steps, as described above, were followed for all data analysis performed for this thesis. For JVLA and GMRT data, the package CASA was used, whereas for ATCA data, the package MIRIAD was used. Further details of data analysis performed for radio data from the two galaxy cluster mergers that we study in this thesis are provided in subsequent chapters.

CHAPTER 4

RADIO RELICS IN THE BULLET CLUSTER AT 5.5 AND 9 GHZ

(Based on "First detection at 5.5 and 9 GHz of the radio relics in bullet cluster with ATCA", Astrophysics and Space Science, 361(8), 1-8 (doi: 10.1007/s10509-016-2844-7))

As stated earlier, clusters of galaxies are the largest gravitationally bound objects in the universe. However, these galaxy clusters are not static; in fact they grow by mergers with other clusters and galaxy groups. These mergers create shock waves within the ICM that can accelerate particles to extreme energies, and lead to "cold fronts" (Markevitch et al. Phys. Rep. 2007) with narrow pressure structures with low particle density; with the compression of magnetic fields along shock fronts causing an additional systematic pressure enhancement.

The acceleration of particles / plasma to extreme energies, and the compression of the magnetic field, lead to the emission of diffuse synchrotron radiation. The cluster merger shock carries with it a portion of accelerated particles, and these regions, which consist of non-thermal distributions of particles, and emit copiously in radio, are known as "Radio Relics". These radio relics are typically elongated along the direction perpendicular to shock propagation, and their sizes can exceed ~ Mpc (Brunetti and Jones 2014). Radio relics are usually highly polarized, and their properties point to a connection with cluster merger shocks.

Radio relics may form due to the acceleration of local electrons, or due to the re-acceleration of previously present relativistic electrons, which may have their origins in the jets or lobes of radio galaxies / active galactic nuclei (AGNs).

While the mechanism of generation of radio relics (which are produced due to merger shocks) is different from that of radio halos (produced due to turbulence in the ICM), the physical processes that cause them are connected (Brunetti and Jones 2014), which implies that radio halos and radio relics may well have bridges between them, especially in relatively younger galaxy cluster mergers.

In general, any non-thermal/relativistic population of particles with a power law distribution, which has lost energy only due to synchrotron radiation, would exhibit a "break" in its power spectrum, i.e. its spectrum would steepen at a certain frequency. Therefore, while studying diffuse emission from these mergers between clusters of galaxies, it is necessary to study the spectral characteristics of the emission, in order to figure out their spectral age.

We examine a relatively "young" cluster merger in this chapter, which is known to host both a radio halo, as well as a radio relic. We examine the spectrum of the radio relics in the cluster and the break in the spectrum, speculate about the origins of the bright radio relics in the cluster, and comment about the connection between radio halos and relics.

4.1 THE BULLET CLUSTER

1E0657–56, known as the 'Bullet Cluster', is one of the hottest known clusters (with X-ray luminosity $L_X \sim 4.3 \times 10^{45}$ ergs/s; temperature kT ~ 14.7 keV) that has been well-studied over the last decade for a variety of reasons; namely, the existence of a cold front in the X-ray observations (Owers et al. 2009) a strong radio halo (Liang et al. 2000), the Sunyaev-Zel'dovich effect (Halverson et al. 2009 ; Plagge et al. 2010 and references therein), though most notably in providing the most direct proof of the existence of dark matter (Clowe et al. 2006). It is a cluster collision/ merger event at $z \sim 0.296$, with the larger, eastward cluster being ~ 10 times the mass of the smaller 'bullet'. A powerful radio halo in the Bullet cluster was first reported by Liang et al. (2000), who detected the radio halo using the ATCA as well as 843 MHz Molonglo Observatory Synthesis Telescope (MOST). Analysis of data in Liang et al. (2000) centered on a 3.5 Mpc^2 region defined by them on the basis of the extent of diffuse emission observed at 1.3 GHz.

Shimwell et al. (2014) reported deep observations of the cluster at 2.1 GHz, with a noise rms of 15 μJy beam^{-1}, a significant improvement over Liang et al. (2000). This was made possible by two upgrades of the Australia

Telescope Compact Array (ATCA)—addition of a N-S spur, and the increase in bandwidth by a factor of 16, through the Compact Array Broadband Backend, or CABB (Wilson et al. 2011). These two upgrades improved the sensitivity of ATCA by a factor of ~ 4, and enabled deep observations of Bullet cluster at 2.1 GHz and higher frequencies.

Shimwell et al. (2014) constructed a spectral index map of the Bullet cluster, and detected polarization in a certain region. Shimwell et al. (2015) studied this region in more detail, and confirmed that it has the characteristics of a relic. They then proceeded to estimate the total brightness of the two components marked 'Region A' and 'Region B' in four sub-bands, and derive spectral indices −1.07 +/- 0.03 and −1.66 +/- 0.14 for the two components respectively. They also interpret 'Region B' as a second shock front. One of the most important aspects of the detection and characterization of diffuse emission in Shimwell et al. (2014,2015) is their "in-band" spectral index estimation, i.e. determination of spectral index within the 1.1–3.1 GHz ATCA band.

2.1 GHz deep observations of Shimwell et al. (2014, 2015) are critical not only for an accurate estimation of the radio halo/relic flux, but also to accurately determine the spectral index of both the radio halo and the radio relic. As a practical matter, it is in fact easier to estimate the total flux and spectral index of the radio relic as compared to the radio halo, since halos, due to their central location in cluster mergers, are likely to be in the vicinity of several point sources (bright radio galaxies).

4.2 ATCA RADIO OBSERVATIONS

The Australia Telescope Compact Array (ATCA) is a radio interferometer with six 22 m antennas, five of which may be positioned on stations along a T-shaped rail track that is 3-km along E-W and 214-m along N-S. The bullet cluster was observed for a total duration of 14 hours in the 6 cm and 3 cm bands with centre frequencies 5.5 GHz and 9 GHz respectively, in a 2-pointing mosaic, with the pointing centers at (J2000 epoch coordinates) RA: 06h 58m 30s , DEC: − 55°57'00" and RA: 06h 58m 20s , DEC: − 55°56'00" respectively. Table 4.1 lists the total amount of time spent on these two pointings, and in slewing and calibration. Imaging from visibilities in this mosaic is described in section 4.3.

Observations were made in the H168 array that has a maximum baseline up to 192-m (using the five antennas in the array) and a minimum baseline of 61-m. A summary of the observations is in Table 4.1. Observations of the Bullet cluster were made in a pair of 2-GHz bands: a '5.5-GHz band' covering frequencies 4.5–6.5 GHz and a '9-GHz band' covering the range 8–10 GHz. Each of the 2-GHz wide bands were subdivided into 2048 frequency channels. All observations were in full polarization mode and recorded multi-channel continuum visibilities. In each observing session, antenna pointing corrections were updated every hour using a 5-point offset pattern observation on a bright calibrator, unresolved phase calibrators were observed every 60 min to monitor and correct for amplitude and phase drifts
in the interferometer arms, and PKS B1934–638 was observed once every session as a primary calibrator to set the absolute flux density scale. Visibilities were recorded with 10 sec averaging. PKS B1934–638 was used as the primary calibrator, and PKS B0823–500 was used as a phase and bandpass calibrator.

The synthesized beam is much larger than in Shimwell et al. (2014) because of our observations being made in the second-most compact configuration at the ATCA, namely, H168. This restricts the longest baseline to 168-m, or $\sim$ 3kλ .The Compact Array Broadband Backend, described in Wilson et al. (2011), was used, with two independent 2048 MHz windows (dual polarization) for correlation, with 1 MHz resolution, which is the standard setting for continuum observations.

4.3 DATA REDUCTION

Data were analysed using the Multichannel Image Reconstruction, Image Analysis and Display (MIRIAD, developed by ATNF-CSIRO); all image processing were also accomplished using utilities in this software package.
Adopted fluxes for the primary calibrator PKS B1934–638 were 4.965 and 2.700 Jy in the 6-cm and 3-cm bands respectively; the spectral index was adopted to be -1.23 in both bands (see Sault 2003). Outliers in the

amplitudes of visibility data on PKS B1934–638 were rejected—removing ~ 10% of data—and the reliable visibilities were used to set the absolute flux density scale as well as determine the instrument bandpass calibration.

When calibrated for the bandpass, the visibility amplitudes of PKS B0823–500 showed continuity across both the 2-GHz observing frequency ranges and a trend consistent with a single power-law: this was a check of the bandpass calibration. Drifts of up to 30° were observed in the interferometer arms over the observing sessions: calibrations for the time-varying complex gains in the antenna signal paths as well as calibrations for polarization leakages were derived from the visibilities on PKS B0823–500. RMS phase variations in antenna signal paths within the 1-min calibrator scan was within 0.5°, indicating that short timescale atmospheric and instrumental phase cycling would result in amplitude attenuation of less than 1%.

The visibility data in the 5.5 and 9 GHz bands were separately edited for interference and calibrated before bandwidth synthesis imaging. Visibility data in each of the 2 GHz wide bands were recorded over 2048 frequency channels, and 50 channels at each of the band edges were excluded from analysis to avoid data in frequency domains where signal path gains are relatively low. Frequency channels that appeared to have relatively large fluctuations in visibility amplitude owing to hardware faults in the digital correlator were also rejected prior to calibration and imaging.

Since no circular polarization is expected, Stokes V is expected to be consistent with thermal noise, and we make estimates of noise rms from Stokes V, following Subrahmanyan et al. (2000). Therefore, at times and frequency channels where Stokes V visibilities deviate more than four times rms thermal noise in the calibrated visibilities acquired towards the cluster pointings, data in all Stokes parameters were rejected. Stokes-V based clipping was therefore done, aimed at automated rejection of self-generated low-level interference. In order to carry out Stokes-V based clipping, the MIRIAD task TVCLIP was used to find the median and rms levels for every channel, and then all visibilities beyond the median +/- 5σ were flagged, and the same flagging was applied to all the other Stokes parameters. This procedure was then repeated for every Stokes parameter. This way, 25% of the data at 5.5 GHz and 20 % of the data at 9 GHz were flagged.

We note here that our observations were made in 2010, when the CABB system (Wilson et al. 2011) was relatively new, and therefore, noise per channel was higher, resulting in a higher T_{sys} , i.e. system temperature/lower sensitivity than is currently possible. Going through our raw ATCA data, we find that the typical T_{sys} in our data is ~ 80–100 K, whereas current estimates of T_{sys} is about 40–50 K.

4.4 RESULTS

4.4.1 RADIO IMAGE AT 5.5 GHZ

Following the analysis described in previous sections, we obtained a radio image of the bullet cluster field, which is shown in 4.1. This image was made with natural weighting, and so were all the subsequent images. It should be noted that the intrinsic resolution of this image is 50.5”x35.9”. A list of point sources, and of regions with diffuse emission, with their location and total

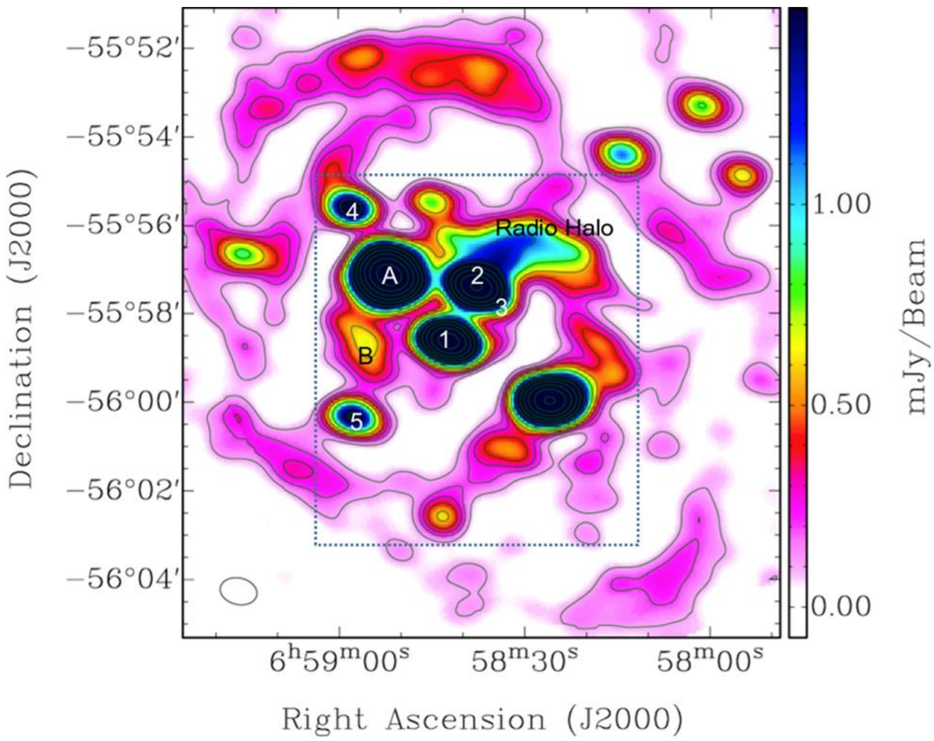

Figure 4.1: 5.5 GHz radio image of the Bullet cluster, observed with H168 array of the ATCA, with a synthesized beam 50.5” x 35.9” (indicated as an ellipse in the bottom left corner). This is a natural-weighted image, and the extent of this image is similar to the Figures in Shimwell et al. (2014). Noise RMS (σ_{RMS}) is 20 μJy/beam. Contour levels are at −5, 5, 10, 15, 20, 40, 80, 160, 320, 640 x σ

emission, is given in Table 4.2; locations of all point sources match with the values in Shimwell et al. (2014). There is clear evidence of diffuse emission at 5.5 GHz, which occurs in the same region as the 2.1 GHz image (Fig.5) in Shimwell et al. (2014). To facilitate comparison with the 2.1 GHz observations in Shimwell et al. (2014), another figure has been made with a synthesized beam of 57” x 57”. Most baselines in the Shimwell et al. (2014) 2.1 GHz image are >> 5kλ, so it is not surprising that the diffuse emission we find in the 5.5 GHz image is similar as compared to 2.1 GHz (Shimwell et al. 2014) – morphologically. The total amount of diffuse emission in these regions is stated in Table 4.2.

There is clear detection of the radio halo and two components of the radio relic, as described in Shimwell et al. (2014,2015)—these are clearly marked in Fig. 4.2. Qualitatively, diffuse emission in Fig. 4.2 is in good agreement with the 2.1 GHz image (Fig. 5) in Shimwell et al. (2014) – both in terms of extent and morphology. In particular, the radio halo at 5.5 GHz has a similar morphology and extent as the halo at 2.1 GHz in Shimwell et al. (2014). We also detect—at relatively low significance—a bridge between the radio halo and Region A. Like Shimwell et al. (2014), we detect more than one local maxima in the radio halo, and two of these local maxima coincide with the X-ray brightness centers, as in the 2.1 GHz image. The radio halo is extended along the merger axis, the physical extent of the radio halo is more along the merger axis than perpendicular to it, and there is a well-defined western edge, again, like the 2.1 GHz image in Shimwell et al. (2014).

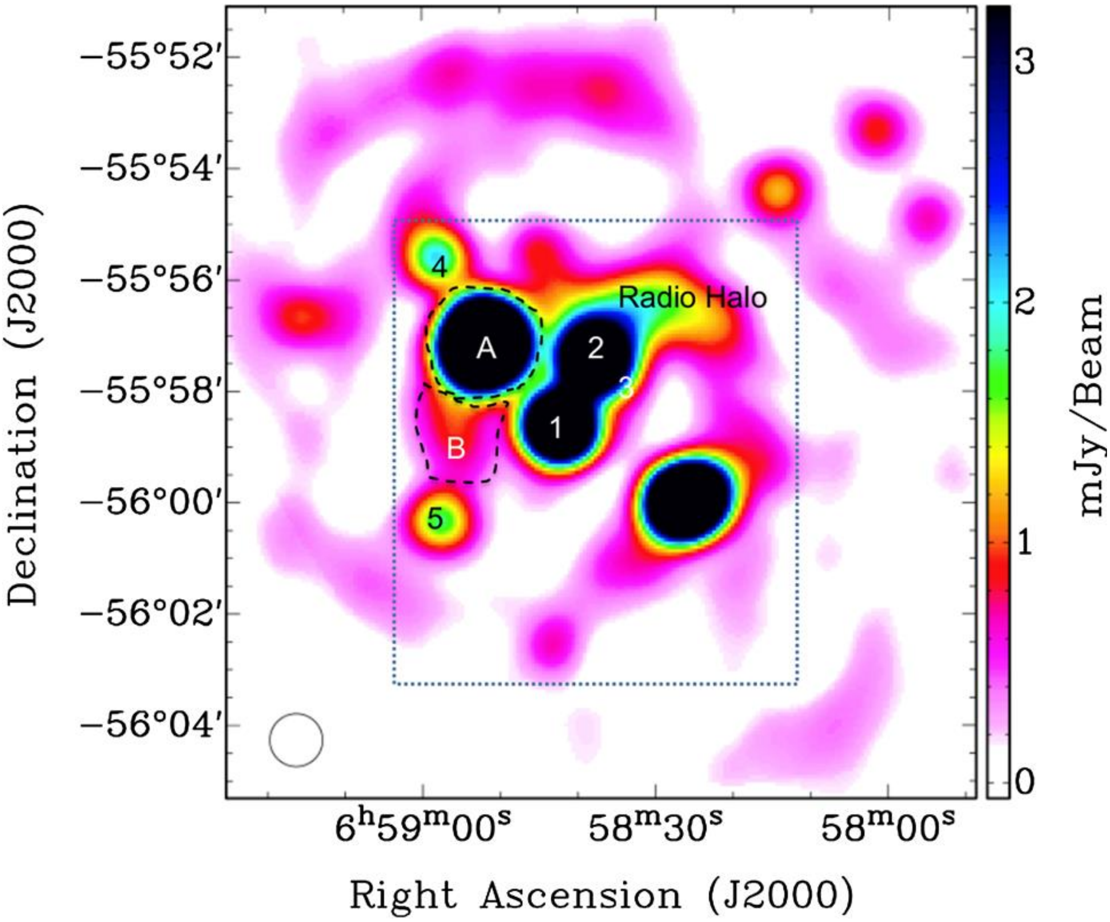

Figure 4.2: 5.5 GHz radio image of the Bullet cluster, observed with H168 array of the ATCA, with a synthesized beam 57" x 57" (indicated as an ellipse in the bottom left corner). This is a natural-weighted image, and the extent of this image is similar to the figures in Shimwell et al. (2014). Noise rms (σ_{RMS}) is 20 μJy/beam. Regions A and B, and the six point sources are marked in the figure. Properties of the point sources and regions A and B are given in Tables 2 and 3. The dashed box indicates the area in the image that we have described in this paper. The two dashed areas indicate roughly the extents of the regions A and B

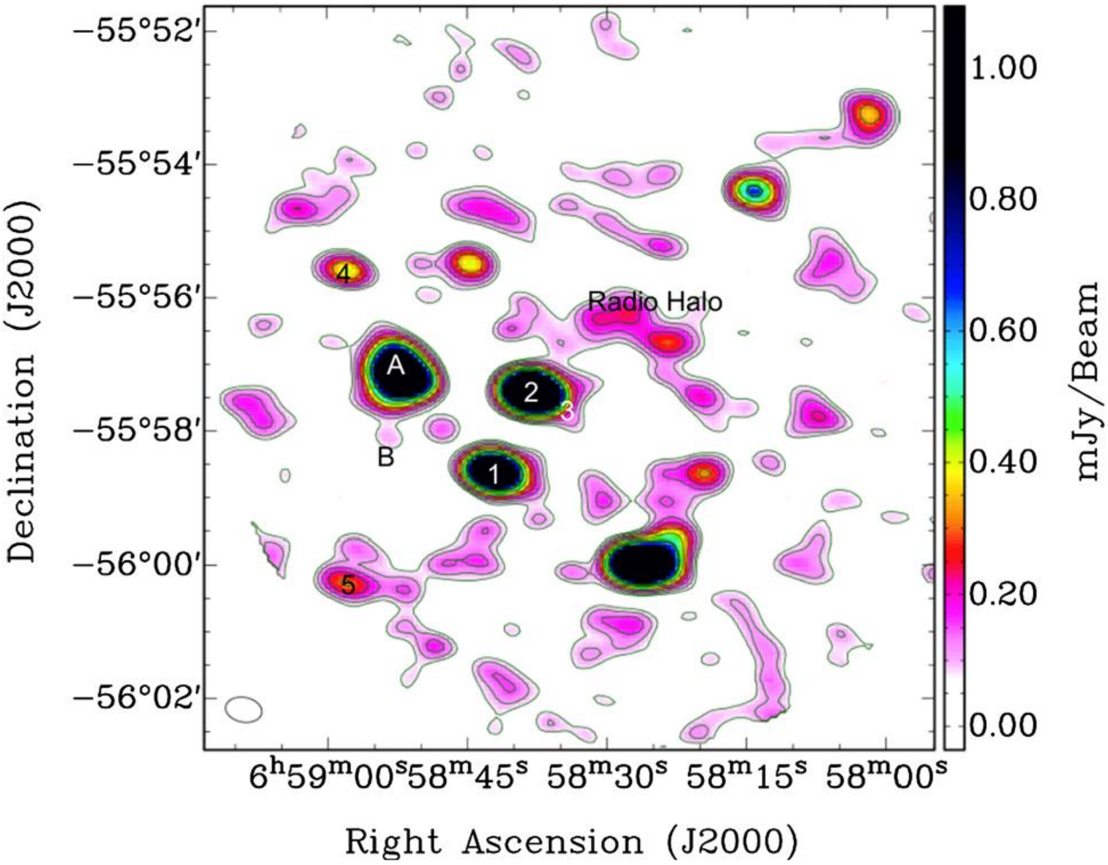

Figure 4.3: 9 GHz radio image of the Bullet cluster, observed with H168 array of the ATCA, with a synthesized beam 33.1" x 22.3" (indicated as an ellipse in the bottom left corner). This is a natural-weighted image, and the extent of this image is similar to the figures in Shimwell et al. (2014). Noise rms (σRMS) is 15 μJy/beam. Contour levels are at −5, 3, 5, 7.1, 10, 14, 20, 28, 40°øσ . Regions A and B, and the six point sources are marked in the figure.

Table 4.1 SUMMARY OF THE ATCA OBSERVATIONS

Array	**Frequency (GHz)**	**Observing time(hours)**	**Date**
H168	5.5	10.0	2010 July 30
H168	5.5	4.0	2010 July 31
H168	9.0	10.0	2010 July 30
H168	9.0	4.0	2010 July 31

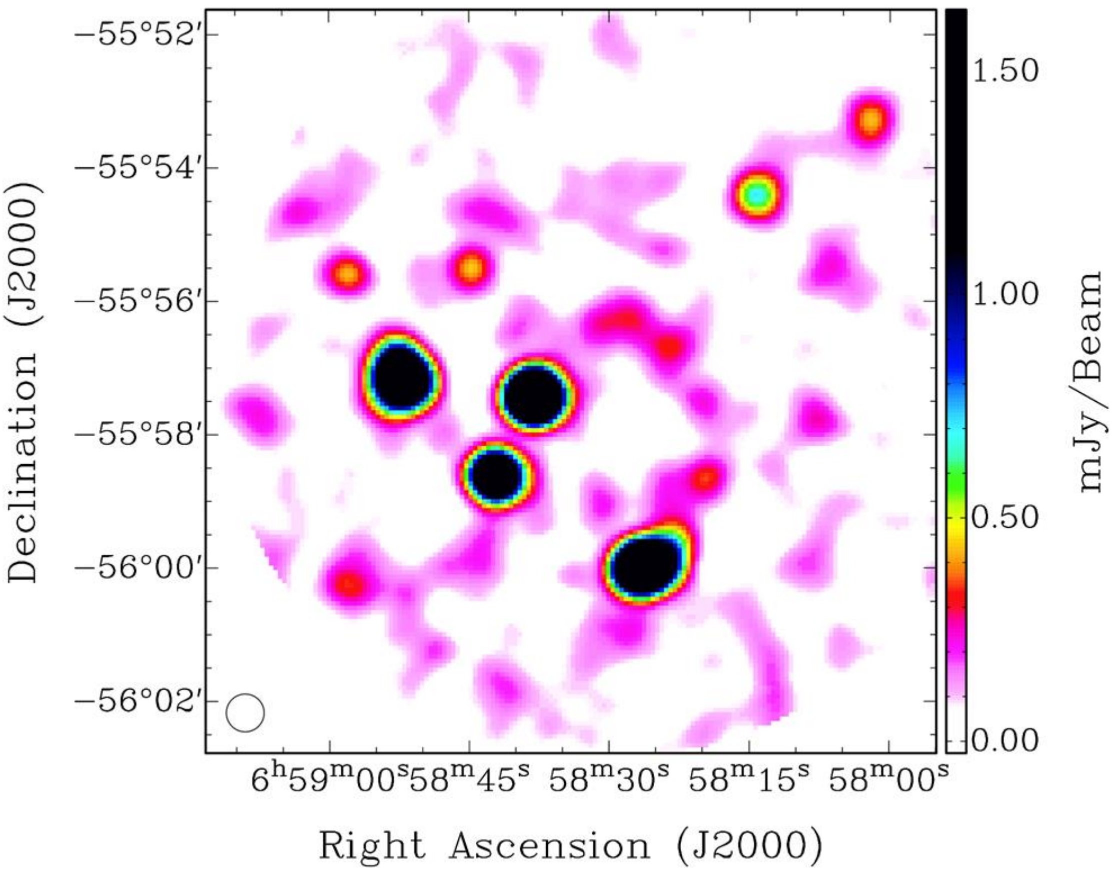

Fig. 4.4: 9 GHz radio image of the Bullet cluster, observed with H168 array of the ATCA, with a synthesized beam 34arcsec x 34arcsec (indicated as an ellipse in the bottom left corner). This is a uniform-weighted image, and the extent of this image is similar to the figures in Shimwell et al. (2014). Noise rms (σ_{RMS}) is 25 μJy/beam

4.4.2 RADIO IMAGE AT 9.0 GHZ

A low-resolution natural-weighted image at 9 GHz of the Bullet cluster, with a synthesized beam of 33.1”x22.3” is shown in 4.3 , and clearly shows diffuse emission is several regions—region A, region B and radio halo. Another image, with synthesized beam 34”x34” (Fig. 4.4) was made to compute the spectral index of regions A and B. Region A is very prominent, but region B is barely detectable, and part of region B are absent, implying that the spectrum might have steepened. There are several similarities with the 2.1 and 5.5 GHz images; for instance, just as in Shimwell et al. (2014) and Sect. 4.4.1, we detect more than one local maxima in the radio halo, and two of these local maxima coincide with the X-ray brightness centers, just as in the 2.1 and 5.5 GHz images – the third local maxima coinciding with the local maxima in radio halo at 5.5 GHz. The radio halo is extended along the merger axis, just as at 2.1 and 5.5 GHz, and there is a well-defined western edge, just as in the 2.1 and 5.5 GHz images. In other words, features of the radio halo at 9 GHz match

qualitatively with the features detected by Shimwell et al. (2014).

4.4.3 RADIO RELIC AT 5.5 AND 9.0 GHZ

Shimwell et al. (2015) have detected and characterized relics in the Bullet cluster at 2.1 GHz. They measured the brightness, substructure and polarization properties of the two relic regions. They interpret Region B as a second shock front, and also comment on the high brightness of Region A, and speculate on its origin.

In this study, we have detected both relic regions A and B in our 5.5 and 9 GHz observations (Figs. 4.1, 4.2 , 4.3 and 4.4). Peak emission occurs at RA: 06h 58m 51. 91s , DEC: − 55° 57’.7.88” at 5.5 GHz, and at RA: 06h 58m 51. 91s , DEC: − 55° 57’11.88” at 9 GHz, the difference between the two positions being 4” , which is a fraction of the beamsize. Our definitions of Relic Regions ‘A’ and ‘B’ are exactly the same as in Shimwell et al. (2015)—with the same extents in declination.

The general large-scale morphology of Regions A and B is roughly similar to Figs. 1 and 3 in Shimwell et al. (2015); however, our observations lack angular resolution, so it is not possible to tell whether the high-resolution structure at 5.5 and 9 GHz is similar to the 2.1 GHz structure.

We have measured the integrated flux of the diffuse radio emission as a function of frequency for regions A and B (see Fig. 4.5) and characterized the 4.5 to 6.5 GHz and 8 to 10 GHz emission. Following Shimwell et al. (2015), we calculated the uncertainty on our integrated flux density measurements by adding in quadrature the ATCA absolute flux calibration error of 2 per cent (Reynolds 1994), with the error on the integrated flux density derived from the image noise. Flux densities for regions A and B at 5.021, 5.468, 5.944 and 9.013 GHz are provided in Table 4.3.

In computing the spectral index, we have taken also taken into account the flux densities of regions A and B as presented in Fig. 2 in Shimwell et al. (2015). Following Fig. 4.5, we obtain the mean spectral index of region A to be $-1.41^{+0.09}{}_{-0.07}$

Table 4.2 UNRESOLVED AND DIFFUSE CONTINUUM RADIO SOURCES DETECTED IN THE BULLET CLUSTER FIELD

Source Label	RA Hour	(J2000) Min	sec	DEC Deg.	Arcmin.	Arcsec	Diffuse or point source	Int. flux density $S_{5.5\ GHz}$ (mJy)	Int. flux density $S_{9\ GHz}$ (mJy)	Shimwell et al. (2014) label
Region A	06	58	51.91	-55	57	07.9	Diffuse	18.04 ± 0.40	4.36 ± 0.15	Region A
Region B	06	58	55.26	-55	58	47.8	Diffuse	0.88 ± 0.08	0.09 ± 0.02	Region B
1	06	58	42.3	-55	58	37.5	Point	8.69 ± 0.20	2.65 ± 0.11	M
2	06	58	37.6	-55	57	24.0	Point	7.54 ± 0.18	4.36 ± 0.13	L
3	06	58	34.3	-55	57	40.0	Point	0.60 ± 0.10	Detected	K
4	06	58	58.1	-55	55	35.1	Point	2.16 ± 0.02	0.43 ± 0.02	Detected
5	06	58	57.8	-55	00	20.1	Point	1.89 ± 0.02	0.39 ± 0.04	Detected
6	06	58	14.6	-55	54	23.0	Point	0.99 ± 0.01	0.75 ± 0.04	N

Notes: Letters indicate diffuse sources; numbers indicate discrete (point) sources from our 5.5 and 9 GHz observations. Regions of diffuse emission are marked with letters on Fig. 4.2 and Fig. 4.4

between 1.1 and 9.0 GHz. For region B, we obtain a mean spectral index of $-1.70^{+0.35}_{-0.31}$ between 1.1 and 9.0 GHz. For region A, we have also fit for a 2-spectral index model: one between 1.1 and 5.0 GHz and the other between 5.0 and 9.0 GHz. 1.1 to 3.1 GHz data is from Shimwell et al. (2014) and Shimwell et al. (2015). The two mean spectral indices are $\alpha^{1.1}_{5.0} = -1.1$ and $\alpha^{5.0}_{9.0} = -2.4$.We present the spectrum of Relic Regions A and B in the 1.1–10 GHz range, in Fig. 4.5.

As can be seen from Fig. 4.5, the 2-spectral index model fits the data really well, which hints at the existence of a break in the power law between 1 and 9 GHz. A similar steepening was reported in Stroe et al. (2014) for the ‘Sausage’ cluster. It should be noted that such high-frequency steepening is inconsistent with Diffusive Shock Acceleration theory (Drury 1983). Stroe et al. (2014) state that high-frequency steepening could be caused by an inhomogeneous medium with temperature/density gradients, or by lower acceleration efficiencies of high-energy electrons. This is discussed in Sect. 4.2.5.

Table 4.3 DIFFUSE EMISSION IN RELIC REGIONS A AND B IN C AND X BANDS

Frequency (MHz)	**Region A (mJy)**	**Region B (mJy)**
5021	19.05 ± 0.20	0.88 ± 0.08
5468	18.04 ± 0.20	0.78 ± 0.07
5944	12.86 ± 0.13	0.66 ± 0.05
9013	04.36 ± 0.15	0.09 ± 0.02

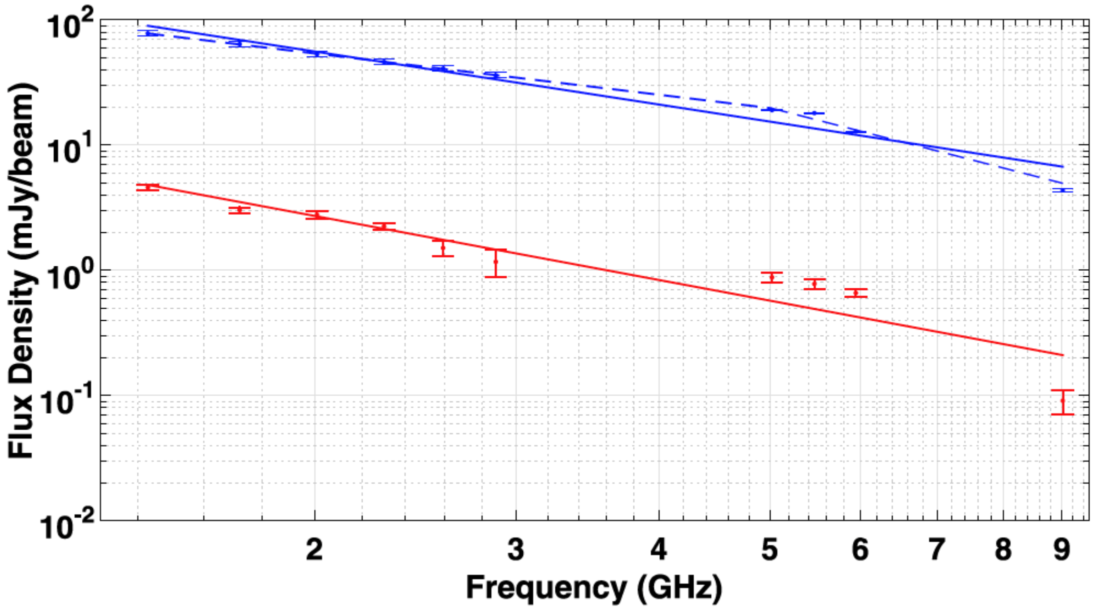

Figure 4.5: Spectral Energy Density of Relic Regions A and B between 1.1 and 9 GHz. Data points for 5.0 and 5.9 GHz are taken from 4.2 and data points for 9.0 GHz are taken from Fig. 4.4. Data points between 1.1 and 3.1 GHz are taken from Fig. 2 of Shimwell et al. (2015). Blue represents Region A and red represents Region B. The solid blue line indicates a single spectral index fit for region A, and dashed blue lines represent a 2-index model for region A. See the discussion in the text

4.4.4 A NOTE ON THE RADIO HALO AT 5.5 AND 9.0 GHZ

As mentioned in sections 4.4.1 and 4.4.2, the radio halo is easily detectable at both 5.5 and 9 GHz in our observations, and we also detect several peaks in the radio halo, spread along the merger axis of the cluster. Despite this, we have not done a detailed analysis at 5.5 and 9 GHz, because our observations lack the angular resolution to identify and characterize point sources, in order to exclude them from estimates of diffuse emission flux. The only details we provide here are as follows. Integrated flux of the radio halo within the 5σ contours is 7.1+/-0.3 mJy at 5.5 GHz and 1.6+/-0. 3 mJy at 9 GHz. We do not compute the spectral index for the radio halo, since point-sources were not subtracted to get the above estimates. Improved data at 5.5 and 9 GHz with other ATCA configurations are essential for estimating the spectral index of the radio halo.

4.5 DISCUSSION

The main results from the study of radio relics in the Bullet cluster at 5.5 and 9 GHz can be summarized as below:

1. The brightest part of diffuse emission in the cluster is a northern relic (referred to in Shimwell et al. 2015 and here as Region A)—significantly brighter than all other diffuse features, and unusually bright at 5.5 and 9 GHz, like the 2.1 GHz observations

2. There is a second shock front—named Region B - immediately to the south of Region A, which is elongated along N-S

3. At very low resolutions (57” at 5.5 GHz and 34” at 9.0 GHz), morphology of regions ‘A’ and ‘B’ are similar at 5.5 and 9 GHz compared to 2.1 GHz

4. Morphology and extent of the radio halo in the cluster are similar at 5.5, 9.0 and 2.1 GHz

5. Spectral index calculation shows a steepening at higher frequencies for Region A, which can best be characterized by a broken power law near 5.0 GHz.

Diffuse emission in cluster mergers has been detected at high frequencies (> 5 GHz) for the Bullet and other clusters (Malu et al. 2010 ; Malu and Subrahmanyan 2011); in particular, Stroe et al. (2016) have characterized the spectrum of the ‘Sausage’ and ‘Toothbrush’ radio relics (van Weeren et al. 2010 , 2012) from 150 MHz to 30 GHz. Therefore, a detection of the radio relic in the Bullet cluster at 5.5 and 9 GHz is unsurprising.

While an ideal Diffusive Shock Acceleration (DSA) model (e.g. Drury 1983) does not predict a break in the spectrum, more realistic models predict a gradual steepening in the 0.1–10 GHz range (Kang 2015 , 2016). Breaks in the spectrum are usually observed to be in the 1–2 GHz. In Stroe et al. (2016) especially, the breaks in the spectra of the ‘Sausage’ and ‘Toothbrush’ radio relics are in the range 2–2.5 GHz. In the case of the observations presented in this paper, the break occurs close to 5 GHz. It is worth pointing out that the possibility of the break in the spectrum of the Bullet cluster occurring in the range 4.8–8.8 GHz has been pointed out (Siemieniec-Ozieblo 2004), based on DSA modeling of the radio relic.

The change/steepening in the spectral index in DSA models with radiative cooling is ∼ 0.5 (e.g. Ensslin et al. 1998), whereas the change we measure for our observations are ≥ 1. In Stroe et al. (2016), the change in the spectral index is ∼ 0.5 for the 'Toothbrush' relic, and ~ 0.8 for the 'Sausage' relic. Therefore, it is safe to say that there may be variations in the spectral index change due to steepening.

Fujita et al. (2015) point out that the turbulent reacceleration of cosmic ray (CR) electrons behind the shock can explain the spectral steepening—which cannot be explained by the standard DSA model—in a few cluster mergers, including the Bullet cluster. Interestingly, they point out possible obscurations of relics by turbulent reacceleration-formed radio halos; while no obscuring is observed in our observations

or Shimwell et al. (2014), both these observations detect a diffuse emission 'bridge' between the relic and the halo, which may be due to the reacceleration of the CR electrons behind the shock.

In order to explain the structure of radio relic spectra, Kang and Ryu (2015) explored DSA models where a spherical shock impinges on a population of relativistic electrons, as shown in their Fig. 1, which details a shock front meeting an elongated structure of fossil relativistic electrons. On comparison with 'Sausage' cluster data from Stroe et al. (2016), they were able to explain the break in the spectrum, but not the complete shape of the spectrum. Interestingly, Shimwell et al. (2015) have pointed out the possibility of fossil relativistic electrons leftover from a radio galaxy causing the bright relic A, so that the modeling done by Kang and Ryu (2015) is directly applicable.

In this context, Kang and Ryu (2016) have considered the model of radio relic formation that is perhaps most relevant for the radio relic in the Bullet cluster, wherein the merger shock goes through a small-size collection of fossil electrons—this causes the spectrum to be steeper than it would be only through radiative aging. Using their simulations, Kang and Ryu (2016) were able to reproduce the spectral curvature in the Sausage cluster as measured in Stroe et al. (2016). Figures 5 and 6 in Kang and Ryu (2016) show their models, with data points from Stroe et al. (2016), in good agreement with their model.

A salient feature of the diffuse emission in the Bullet cluster is the connection between the bright radio relic A (Region A) and the radio halo. This connection is clearly visible in figures 4.1 and 4.2 at 5.5 GHz, and in Shimwell et al. (2014), i.e. at 2.1 GHz. The connection between the two, i.e. the radio halo and the radio relic, may be indicative of the fact that diffuse emission in both regions is caused by merger shock – in the case of the radio halo, it is the turbulence behind the shock that causes the synchrotron emission, whereas in the case of relic A (or Region A), it may be due to the shock passing through a region that contains relativistic electrons left over, perhaps from a radio galaxy (Shimwell et al. 2014). It is also possible that the physical extent of these fossil / left-over non-thermal electrons is large enough that a portion of the relic A appears to be a bridge to the radio halo.

In the case of both the relic regions A and B, the break frequency is found to be ~ 5 GHz. In other clusters – notably the radio halo in Abell 521 (Brunetti et al. 2008, Nature) – the break frequency is significantly lower at < 1 GHz. This implies that this cluster merger is significantly more energetic, which is apparent from its X-ray temperature as well.

In conclusion, from our study of the Bullet cluster radio relics at 5.5 and 9 GHz, we find a steepening of the spectra of both the radio relics at ~ 5 GHz. Recent theoretical models may help explain spectral characteristics of these radio relics in the Bullet cluster. There is also a prominent connection between the radio relic A and the radio halo in this cluster, which may be indicative of the common origins of radio halo and relics.

CHAPTER 5

THE CLUSTER MACS J0417.5-1154 AT 5.5 AND 9 GHz

(Based on "The peculiar cluster MACSJ0417-1154 in the C & X- bands", Astrophysics and Space Science, 363:133 (https://doi.org/10.1007/s10509 - 018 -3354 - 6))

In the previous chapter, we studied the radio relics in the Bullet cluster, which is perhaps the most well-known cluster merger, at 5.5 and 9 GHz. The spectrum from 2 to 9 GHz was presented, and we were able to fit this spectrum well with two spectral indices, with the break or 'knee' in the spectrum occurring at ~ 5 GHz.

In this chapter, we study the other kind of diffuse emission associated with cluster mergers, i.e. a giant radio halo, in MACS J0417.5-1154. This is one of the most massive clusters in the MAssive Cluster Survey catalogue, and is also one of the most X-ray luminous. Its disturbed X-ray contours pointed to the possibility of this cluster being in a non-relaxed / merging state, which is why it was observed using the GMRT by Dwarakanath et al. (2011), at 235 and 610 MHz.

Dwarakanath et al. (2011) found diffuse emission in the central regions of this cluster, i.e. a giant radio halo, from their observations. They also found that the spectrum between 235 and 610 MHz of this radio halo was one of the flattest ever observed, at -0.38. In a later study, Parekh et al. (2017) found, from JVLA observations at 1575 MHz, that this radio halo also has one of the sharpest known cutoffs or 'knee' at 610 MHz, with the spectral index changing from -0.38 to -1.72.

Such sharp cutoffs in the spectrum have been observed earlier (Brunetti et al. 2008), but the low frequency at which the cutoff occurs, while not unprecedented, is peculiar. The reason that the low frequency of the cutoff is strange is that this feature is expected in relatively older cluster mergers, where synchrotron aging has played a role, and the diffuse emission at higher frequencies is significantly lower.

However, this extremely X-ray bright cluster does not demonstrate any other trait of an older merging system – there are no signs of a relic, or any relic-like structure, at any frequency. In this chapter and the next, we investigate the properties of diffuse emission that is found in the centre of this cluster at different frequencies, ranging from 150 MHz to 18 GHz, i.e. more than 2 orders of magnitude in frequency. We begin by examining the diffuse emission in the cluster at 5.5 and 9.0 GHz using data from the Australia Telescope Compact Array (ATCA).

5.1. INTRODUCTION

MACS J0417.5− 1154 is a hot (T ~ 11 keV), X–ray luminous ($L_X \sim 3.66\text{x}10^{45}$ ergs s^{-1}) and the most massive ($M \sim 10^{15} M_{sun}$) cluster that was discovered by the MAC Survey (Ebeling et al. 2010). The first radio observations were done with GMRT at 235 and 610 MHz by Dwarakanath et al. (2011), who were motivated by the peculiar nature of the cluster/merger, specifically the extremely flat spectrum of the diffuse emission in the cluster − the flattest observed so far between 235 and 610 MHz (Dwarakanath et al. 2011).

In both Dwarakanath et al. (2011) and Parekh et al. (2017), the cluster shows diffuse emission in its centre, that is co-located with the X-ray emitting hot gas, and has a south-east to north-west extension. The cluster centre has two unresolved point sources, detected at 235 and 610 MHz (Dwarakanath et al. 2011) and also at 1575 MHz, from Very Large Array (VLA) observations (Parekh et al. 2017). Since the low-frequency end of diffuse emission in this cluster has been studied, we are interested primarily in pushing the high-frequency end. Our high-frequency radio observations constitute a complement to the work of Dwarakanath et al. (2011)
and Parekh et al. (2017).

We present our observations, the estimation of diffuse emission, and the spectrum thus obtained, and discuss our results and future directions in the last section.

5.2. RADIO OBSERVATIONS AND IMAGING

MACS J0417− 1154 was observed for a total of 8 hours in the H168 array of the Australia Telescope Compact Array (ATCA), at 5.5 and 9.0 GHz. ATCA continuum mode with 1 MHz resolution (Wilson et al. 2011) with all four Stokes parameters and 2048 channels was used for these observations, in each of the two bands, centered at 5.5 and 9.0 GHz respectively. 1934− 638 was used as the primary/amplitude calibrator and 0403− 132 as the secondary/phase calibrator. Data were analyzed using Multichannel Image Reconstruction, Image Analysis and Display (MIRIAD, developed by ATNF; see Sault et al. (2011, 1995) for details). Radio frequency interference induced bad data was excised. The secondary/phase calibrator was observed once every 30 minutes to keep track of variations in phase due to atmospheric effects.

Our radio data reduction technique for ATCA data is described in Malu et al. (2016); we summarize the self-calibration steps here. Self–calibration was done in three steps of phase self–calibration and one of amplitude & phase self–calibration. A natural weighted image at 5.5 GHz is shown in Fig. 5.1, and at 9 GHz in Fig. 5.2.

A natural weighted image with about 4 times the size as Fig.(2) in Dwarakanath et al. (2011) is shown in Fig. 5.1. There is evidence of diffuse emission in this figure, with the central region significantly larger than the synthesized beam, and with a distinct morphology, which is similar in the 5.5 and 9.0 GHz images, in Figs. 5.1 and 5.2. The 9 GHz image in Fig. 5.2 has been convolved to the beam of the 5.5 GHz image in Fig. 5.1, i.e. 46.3″x 31.9″ with PA 74.02°.

5.3. ESTIMATION OF DIFFUSE EMISSION AT 5.5 AND 9 GHZ

Figs. 5.1 and 5.2 are low-resolution, i.e. they do not have data from Antenna 6 of ATCA (at a distance of ~ 3-6 km from the rest of the array, depending on the array configuration). Baselines involving Antenna 6 are able to provide a resolution of up to 5″ at 5.5 GHz and 2″ at 9 GHz. Being low-resolution images, it is not possible to estimate the amount of diffuse emission without data from Antenna 6. These low-resolution images are useful for estimating large-scale diffuse emission.

In order to estimate the amount of diffuse emission in the cluster at 5.5 and 9 GHz, we adopted the following approach.

1. First the total integrated flux of the central region, shown in Fig. 5.1 and Fig. 5.2 was estimated, at 5.5 and 9 GHz. To do this, the 9.0 GHz image was convolved to the beam size of the 5.5 GHz image, i.e. 46.3″x31.9″ and PA 74.02° .
2. Then, images were made with a synthesized beam of 3″ at 5.5 and 2″ at 9 GHz (the best resolution available at the two frequencies respectively).
3. Integrated flux densities for the two sources, A and B (following labels from Parekh et al. (2017)) were estimated by Gaussian fitting.
4. Finally, the fluxes of A and B were subtracted from the total integrated flux of the central regions obtained from the 46.3″x31.9″ PA 74.02° images at 5.5 and 9.0 GHz.

Flux density of the diffuse emission in the central region of the cluster thus estimated is presented in Table 5.2, with details of the two point sources.

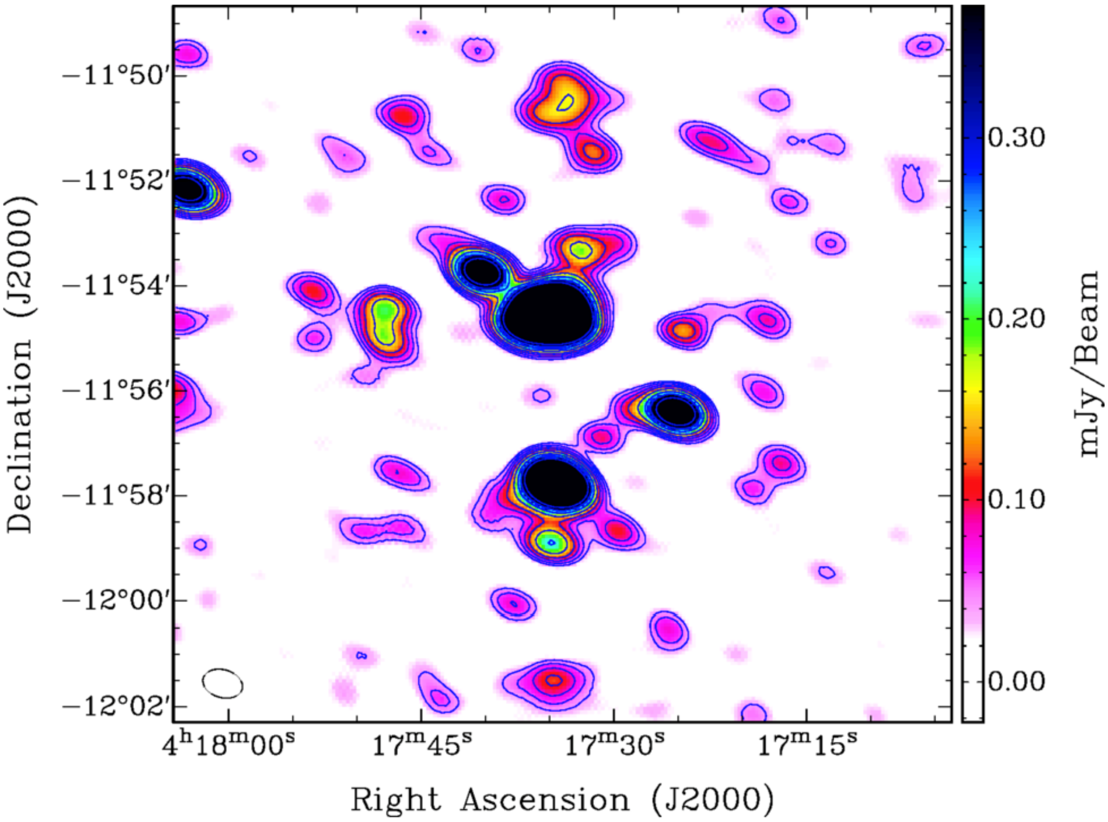

Figure 5.1: A natural-weighted image of the entire region of the cluster MACS J0417-1154 at 5.5 GHz from ATCA. The beam, which is 46.3 arcsec x 31.9 arcsec with PA 74.02◦ is shown in the bottom left-hand corner. Noise rms is σ = 8 μJy/beam. Contour levels start at 5σ, and increase by factors of √2

Table 5.1 SUMMARY OF THE ATCA OBSERVATIONS

Array	Frequency (GHz)	Observing time (hours)	Date
H168	5.5	8.0	2012 March 17
H168	9.0	8.0	2012 March 17

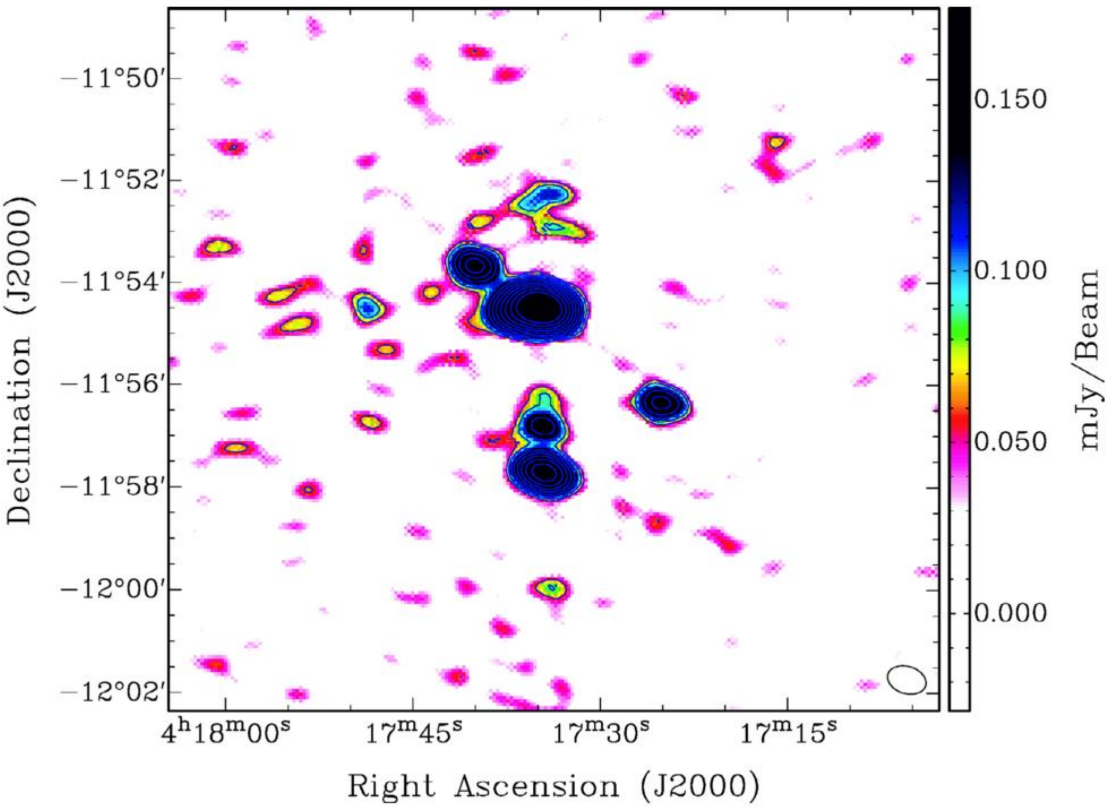

Figure 5.2: A natural-weighted image of the central region of the cluster MACS J0417-1154 at 9 GHz from ATCA. The image has been convolved to the same beam as the 5.5 GHz image in Fig. 1, i.e. 46.3arcsec x 31.9arcsec with PA 74.02^o, and is shown in the bottom left-hand corner. Noise rms is 12 μJy/beam. Contours start at 5σ (outermost contour) and increase by a factor of √2

5.3.1 RESULTS

Diffuse emission obtained after subtracting estimated fluxes of the sources 'A' and 'B' is presented in Table (3) and as a spectrum, from 0.235 to 9.000 GHz, in Fig. (3).

The calculation of spectral index from Table 3 yields $\alpha^{0.23\ \mathrm{GHz}}{}_{9.00\ \mathrm{GHz}}$ $=1.45^{+0.08}{}_{-0.06}$ – this is the best-fit spectral index for the entire spectrum. However, as shown in Fig. 5.3, two fits – one from 0.235 to 0.61 GHz, and the other from 0.61 GHz to 9 GHz – are a better fit to the data. Note from Fig. 5.3 that the spectrum is extremely flat at frequencies lower than 1 GHz, and then steepens very sharply, starting at 0.61 GHz. This sudden shift in the spectral index at 0.61 GHz that makes this a peculiar cluster. This sharp "knee", noticed by Parekh et al. (2017), at 610 MHz, yields a spectral index of $\alpha = -1.72^{+0.08}{}_{-0.10}$, which appears to be a good fit up to 9 GHz, from Fig. 5.3, and is consistent with the spectral index from 0.61 to 1.575 GHz from earlier low-frequency observations.

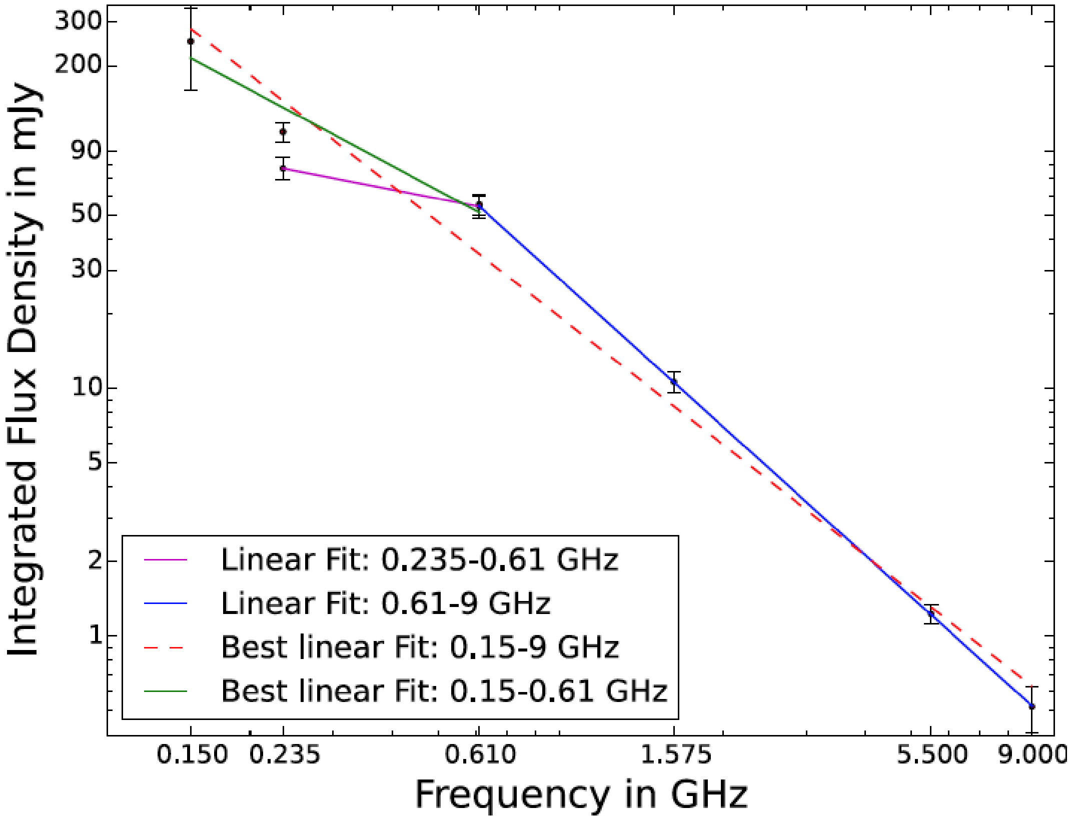

Figure 5.3: The spectrum of diffuse emission in MACS J0417-1154, from 0.150 to 9 GHz. The best-fit spectral index is $\alpha = -1.45$, denoted by a dotted red line. The dotted red line is the single spectral index fit from 0.15 to 9 GHz, considering the upper limit on the diffuse emission at 0.235 GHz, as deduced from the GLEAM survey. Notice that a two-index fit, as shown through a green-line fit from 0.15 to 0.61 GHz, and a blue-line fit from 0.61 to 9 GHz fits the data better. Of the two data points at 0.235 GHz, the lower one is from earlier texts, i.e. Parekh et al. (2017), and the upper one is deduced from the GLEAM survey, as described in the text. The estimate at 0.15 GHz is deduced from the GLEAM and TGSS surveys, as described in the text

Alternatively, the radio image (Fig. 5.4) from the GLEAM Survey (Wayth et al. 2015; Hurley-Walker et al. 2017) suggests that the reported 235 MHz diffuse emission flux may have been underestimated. We found from the GLEAM survey images at 223–231 MHz that the total intensity in the central region of the cluster is ~ 171 mJy, and the total flux of the two sources, from Parekh et al. (2017), is ~ 63 mJy. This would imply a total diffuse emission flux _ 108 mJy, which is significantly greater than the estimate of 77 mJy provided in Parekh et al. (2017). Unlike Parekh et al. (2017), we did find diffuse emission from TGSS (Intema et al. 2017). A total flux density of ~

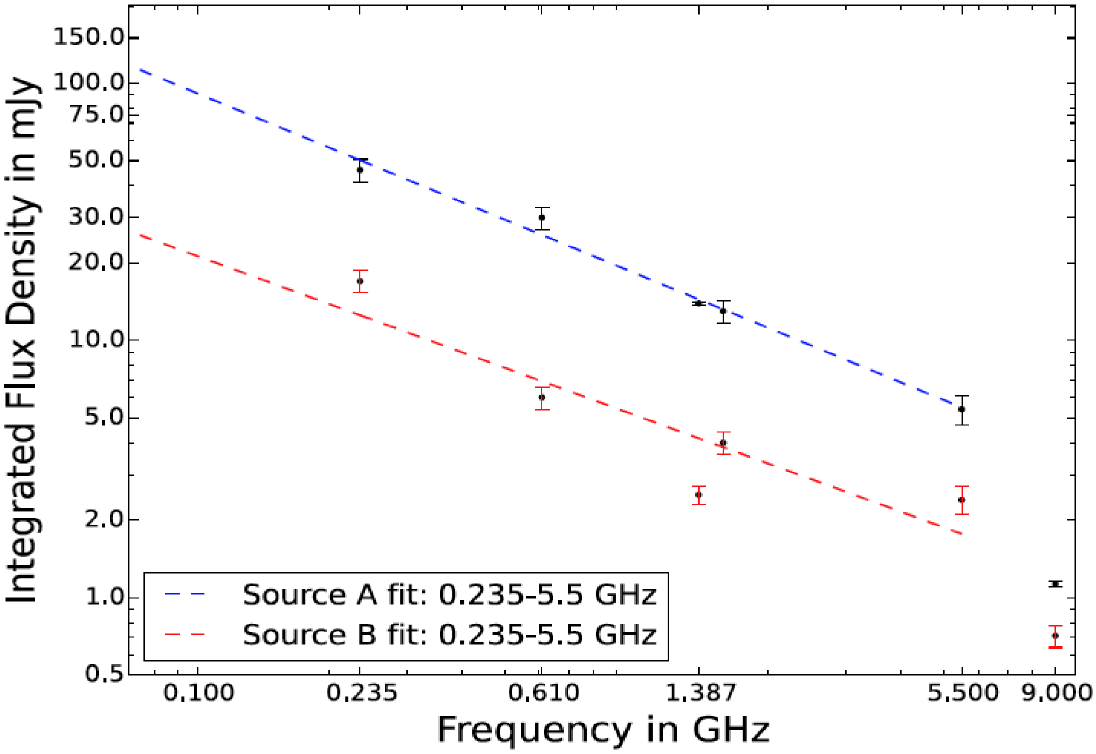

Figure 5.4: The spectrum of the two point sources A and B. Black labels represent the source A and red ones represent B. Notice that the spectrum for both the sources steepens beyond 5.5 GHz. For this reason, the spectrum has been fit to a single spectral index up to 5.5 GHz. These single spectral index fits have been plotted down to 70 MHz

154 mJy was found at 150 MHz in the central region, and a total flux density of ~ 108 mJy was found for the two point sources A and B. We made estimates of point source fluxes of A and B at this frequency from the TGSS data and deduced the diffuse emission flux density, since the GLEAM survey provides images at 150 MHz as well. From the 150 MHz image, we deduced a total emission of ~ 360 ± 90 mJy from the central region. This implies that the flux density of diffuse emission at 150 MHz is ~ 250 mJy. These observations at 150–235 MHz from GLEAM may mean that the ‘knee’ in the spectrum at 610 MHz is not as dramatic as it appears to be, and that the sharp cutoff at 610 MHz is at least in part due to the underestimation of diffuse emission at 235 MHz. As can be seen in Fig. 5.3, the entire spectrum from 150 MHz to 9 GHz needs two-spectral-index fit, but the change in the spectral index is no longer sharp. Instead of the spectral index of − 0. 37 between 0.235 and 0.61 GHz, we now get a spectral index of $-1.04^{+0.35}_{-0.26}$ between 0.15 and 0.61 GHz, a change by a factor > 2. The change to a spectral index of $-1.72^{+0.08}_{-0.10}$, for 0.61 to 9 GHz, is significantly less dramatic.

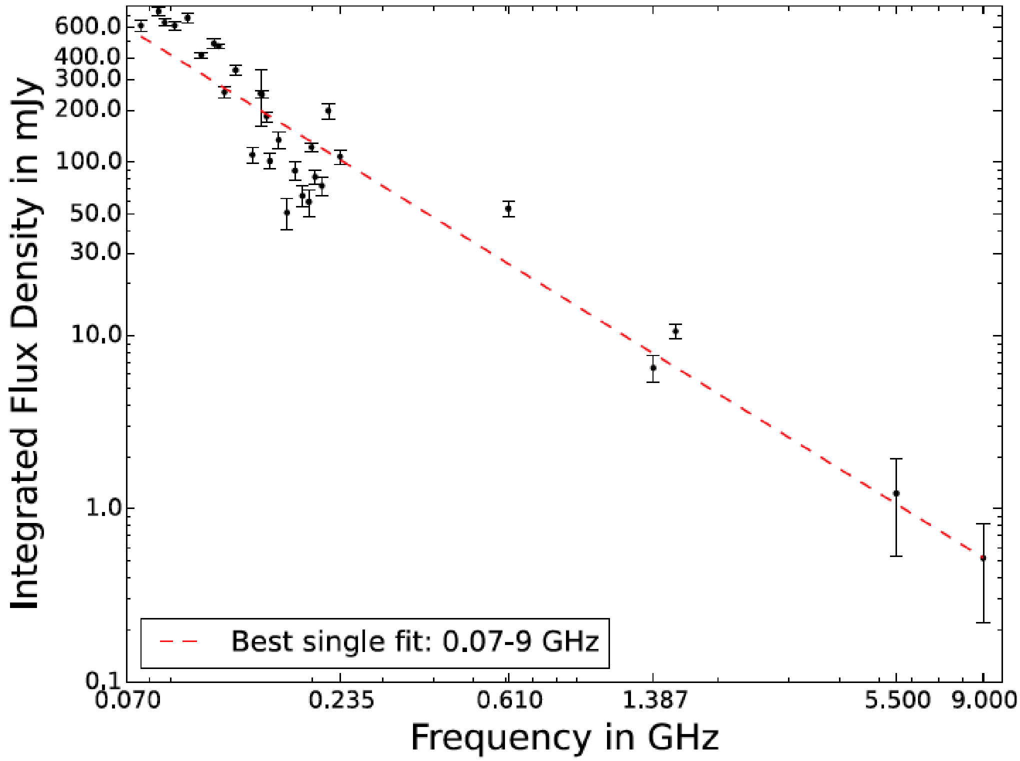

Figure 5.5: The spectrum of diffuse emission at low frequencies estimated from GLEAM data.

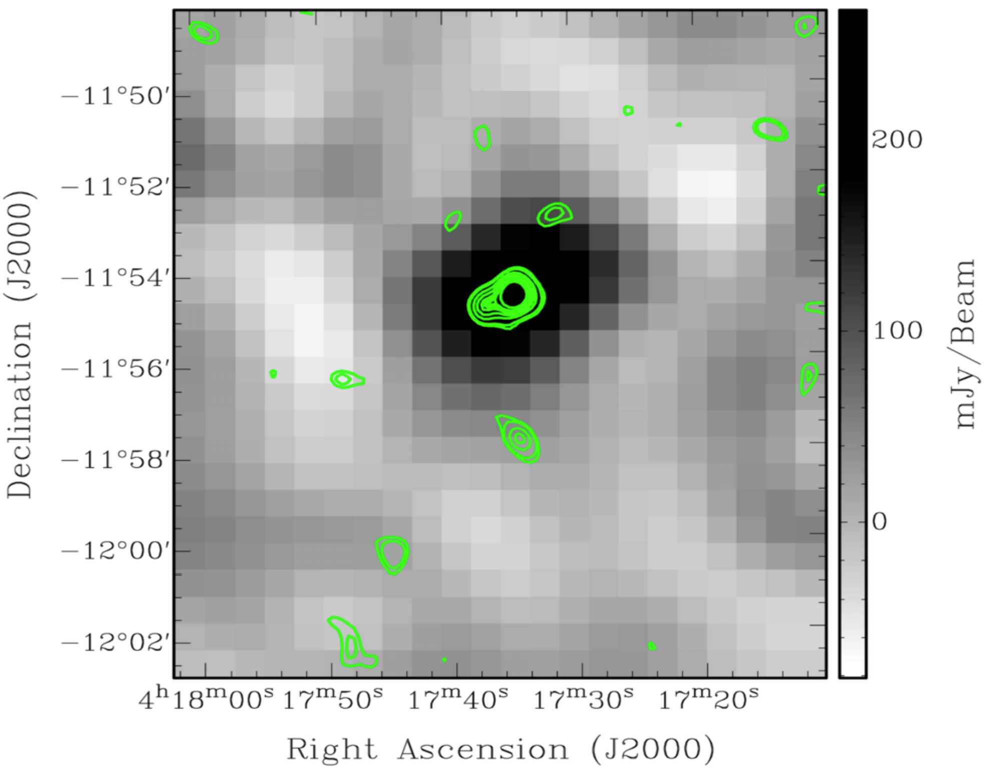

Figure 5.6: TGSS contours overlaid on 150 MHz GLEAM image of MACS J0417.5-1154. Contour levels are (2.5, 3, 5, 7, 9, 10, 11, 15) °σ, where σ is 3 mJy/beam.

Table 5.2 UNRESOLVED AND DIFFUSE CONTINUUM RADIO SOURCES DETECTED IN THE CENTRAL REGION OF MACSJ0417-1154

Source label	RA			DEC			Diffuse or point source	Int. flux density $S_{5.5\ GHz}$	Int. flux density $S_{9\ GHz}$
	hour	min	sec	Deg.	arcmin	arcsec		mJy	mJy
Source A	04	17	34.7	-11	54	30.6	Point	5.40 $\pm$ 0.70	2.40 $\pm$ 0.30
Source B	04	17	36.7	-11	54	38.7	Point	1.13 $\pm$ 0.03	0.71 $\pm$ 0.07
Central region	04	17	42.3	-11	54	37.5	Diffuse + Point	7.76 $\pm$ 0.10	3.63 $\pm$ 0.10

Table 5.3 DIFFUSE EMISSIONS IN THE CENTRAL REGION

Frequency (MHz)	Diffuse emission (mJy)
235*	77.0 $\pm$ 8.0
610*	54.0 $\pm$ 5.5
1575°	10.6 $\pm$ 1.0
5500	1.23 $\pm$ 0.7
9000	0.52 $\pm$ 0.3

Our estimates of diffuse emission in the cluster indicate that the spectrum at higher radio frequencies is consistent with the steep spectrum up to the L band, reported earlier Parekh et al. (2017); that is, there is no break in the spectrum from 1.575 to 9.000 GHz. Considering this is the most massive and X-ray luminous cluster in the MACSurvey, it is curious that it contains little diffuse emission, indicating low activity in radio.

5.4. DISCUSSION AND SUMMARY

We have presented 5.5 and 9.0 GHz observations of MACS J0417.5− 1154, a hot, X-ray luminous, massive galaxy cluster with disturbed X–ray contours, using the H168 array of the ATCA, and found that diffuse emission is present at these two frequencies. Our data is able to constrain the diffuse emission present in the cluster, at 5.5 and 9.0 GHz.

This cluster – which was earlier known to host a radio halo with one of the flattest spectra known – shows the peculiarity of one of the sharpest 'turn-off' point or 'knee' in the spectrum, at 610 MHz. Such 'knees' have been observed in other clusters (Brunetti et al. 2008), though the sudden transition from such a flat spectrum to a steep one, is interesting.

We point out that the images in Parekh et al. (2017), with a resolution of 20″x20″ , do not show any structure for the two sources 'A' and 'B'. It is, however, not clear what fraction, if any, of the diffuse emission in the central region is to be attributed to the two compact sources – which may be radio galaxies – and what fraction is part of the radio halo. Moreover, the spectral index in both radio halos and radio relics demonstrates large variations across the cluster. Unless the two sources are studied closely at multiple wavelengths, with high-resolution data, it may not be possible to make definite comments about the source of the diffuse emission in this cluster. Since we have subtracted the flux obtained at and in the vicinity of sources 'A' and 'B', our estimates of diffuse emission at 5.5 and 9.0 GHz are really lower limits.

While recent literature on the subject (Fujita et al. 2015; Kang and Ryu 2015) discusses spectral curvature, and how it is affected by the morphology of non-thermal particles, this spectrum does not indicate any curvature, but just a two-spectral index fit, with the second spectral index yielding an excellent fit to the data up to 9 GHz. In this context, Kang and Ryu (2016); Kang and Ryu (2016, 2015) have considered a cluster merger shock that passes through a small region containing fossil non-thermal electrons. They show that in such a scenario, the spectrum would be significantly steeper than expected through radiative cooling. Kang and Ryu (2015) consider such a model with the small region of fossil non-thermal particles elongated perpendicular to the direction of the shock, as a way to reproduce the spectral curvature of the "Sausage" radio relic (Stroe et al. 2014; Kang 2016). Even though their model pertains to relic formation, it may be possible to use a model with a different morphology of the fossil non-thermal particles, in order to explain the hard break in the spectrum of MACS J0417− 1154 at 610 MHz.

Kang and Ryu (2016) point out the role of turbulent re-acceleration of cosmic ray (CR) electrons, which have been weakly accelerated by the cluster merger shock. They show that strong turbulence behind the shock can accelerate the CR electrons – this may be a possible reason for the spectral index continuing without a break from 0.61 to 9 GHz. A break at 0.61 GHz in this model may indicate a less energetic cluster merger.

The sudden steepening of the spectral index may be indicative of spectral aging, but the steepened spectrum extending from 0.61 to 9.00 GHz (i.e. more than an order of magnitude in frequency) is, to the best of our knowledge, unprecedented. This sharp change suggests that the integrated flux of this radio halo should be measured at frequencies between 235 and 1575 MHz, to study the steepening of the spectrum, and above 10 GHz, to study spectral curvature.

However, we have shown, through archival GLEAM and TGSS data, that the flux of diffuse emission may have been underestimated in earlier studies. This changes the behaviour of the spectrum considerably, from one that exhibits a sharp turnover at 0.61 GHz, to one that exhibits a much gentler steepening. This steepening may not require a unique, exotic explanation, and is likely a signature of a relatively new/young galaxy cluster merger, which seems to be the case here.

In conclusion, we have shown, through data at 5.5 and 9 GHz from ATCA, that the cluster merger MACS J0417−1154 has several peculiarities in the synchrotron emission from its centre, and that these peculiarities point to a need to study both effects of fossil non-thermal electrons lurking in one of the clusters before the merger, as well as the role of turbulent re-acceleration in the formation of radio halos.

The aforesaid discussion assumes that the diffuse emission in the central region of this cluster is part of a radio halo, due to a cluster merger. However, the two sources in the central region may not be compact, and may have some diffuse emission associated with them, a detail that cannot be deduced from a simple Gaussian modeling of the sources, as in Parekh et al. (2017). Additionally, diffuse emission at 235 MHz is likely underestimated, from the GLEAM survey data. This implies that the break in the spectrum is likely not as sharp as it appears to be. For these reasons, we stress the need for high-resolution multi-frequency images of the central region of this cluster, at frequencies in the range 0.2–1.57 GHz, in order to characterize the variation of the spectral index of diffuse emission.

CHAPTER 6

MULTI-FREQUENCY RADIO OBSERVATIONS OF THE CLUSTER MACS J0417.5-1154

(Based on "Radio Observations of the cluster MACSJ0417.5-1154", Raja, R., Kaur, P. et al. 2018, under review for publication in Journal of Astrophysics and Astronomy)

6.1. INTRODUCTION

In the last chapter, we studied the diffuse emission in the cluster MACS J0417.5-1154 at 5.5 and 9 GHz. We found diffuse emission in the central region of the cluster at both frequencies, and concluded that this cluster is radio-quiet, even though it has the characteristics of a merging system – extremely massive, extremely hot, and with extended X-ray luminosity contours. This presents a puzzle – why is there so little diffuse emission, even though this cluster is supposed to be undergoing a merger, and is extremely X-ray luminous and hot?

Several merging clusters have been found to be in the radio-quiet state, and these have been studied well by now (Brown et al. 2011). Nevertheless, steepening of the spectrum at a low frequency is indicative of a relatively larger merger age, or a less energetic merger. However, neither of these possibilities is supported by the existing data, which points to a young, energetic cluster merger. Therefore, we need to address this issue.

As pointed out in the previous chapter, GLEAM and TGSS data show that diffuse emission may have been underestimated at 235 MHz – this may imply that either there is not a break in the spectrum of this cluster at 610 MHz, or that the break occurs at a higher frequency.

In this chapter, we investigate the diffuse emission in this cluster at 16-20 GHz (18 GHz central frequency), looking for a break in the spectrum. We describe our results in the last section, and discuss them in the context of the apparent sharp break in the spectrum at 610 MHz. We present a resolution of the above issues, based on our data, and show that this is consistent with expectations.

6.2. RADIO OBSERVATIONS AND DATA REDUCTION

Array	Frequency (GHz)	Observing Time (hours)	Date
GMRT	1.387	7.5	2014 June 17
ATCA	18.000	8.0	2011 October 11

Table 6.1 SUMMARY OF THE GMRT AND ATCA OBSERVATIONS

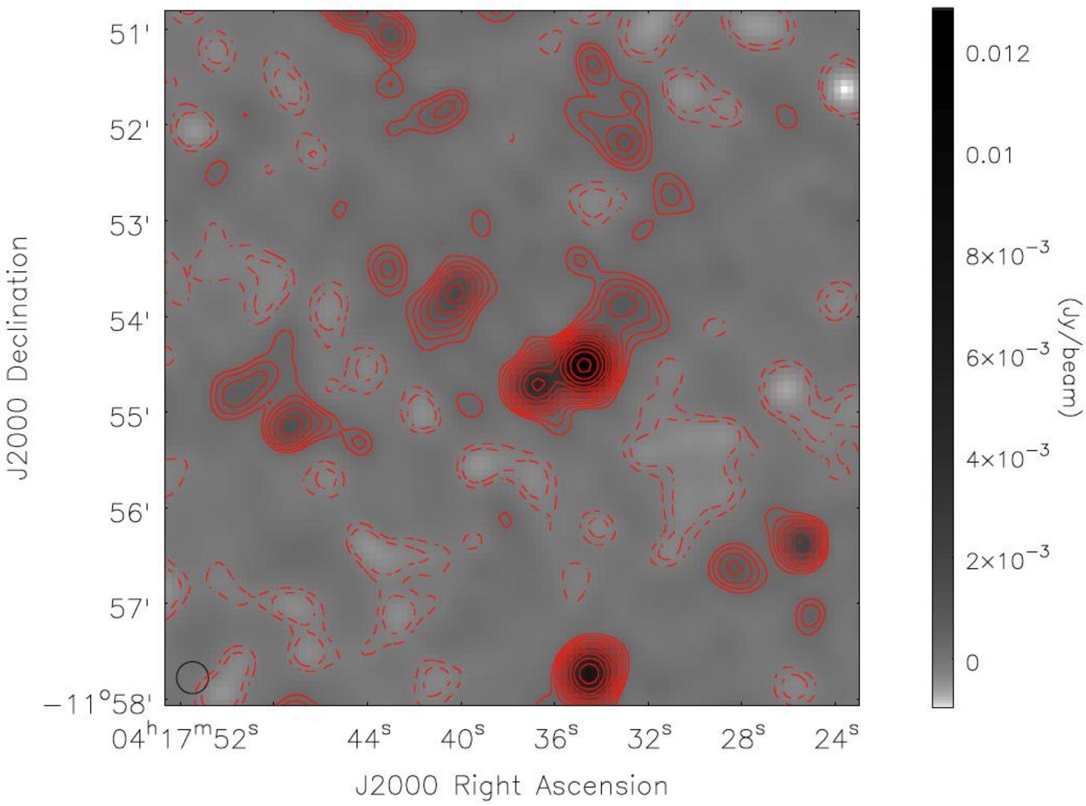

Figure 6.1. The GMRT radio image at 1387 MHz. The resolution of this image is 20'' with rms noise of 50μJy/beam. The contours levels start at 5 σ and increase by factor of $\sqrt{2}$. Dashed lines are negative contours at 3 and 5σ.

6.2.1 L-BAND GMRT DATA

MACSJ0417.5−1154 was observed from GMRT (Giant Metrewave Radio Telescope) for 7.5 hours at 1387 MHz. Full stokes observations were done with 256 channels over 32 MHz bandwidth with integration time 16 sec. Data analysis was done using the Common Astronomy Software Applications (CASA) package (developed by NRAO). The data were inspected for RFI

(Radio Frequency Interference) and other issues and excised. Total flagged data is approximately 60%. The flux density of the primary/flux calibrator was set according to the Perley & Butler (2013). 3C147 was used as primary calibrator. Initial phase calibration was done for the primary calibrator followed by delay and bandpass calibration. Gain calibration was done for both primary and secondary calibrator (0405−131) followed by the scaling of the amplitude gain of the secondary calibrator. Then the calibration solutions were applied to the target data. From the calibrated data imaging was done by standard Fourier transform deconvolution method using CASA task ‘clean’˙Imaging was done

with multi-frequency synthesis along with wide-field imaging (using 256 w-projection planes). The image (Fig. 6.1) was convolved with 20″ x 20″ beam, in order to keep our resolution same as that of Parekh et al. (2017) results at L-band. It should be noted that Parekh et al. (2017) used this restoring beam size in order to match the TGSS beam, so in order to estimate the spectral index between the frequencies. The off-source RMS noise near the centre of the image is 50 µJy/beam.

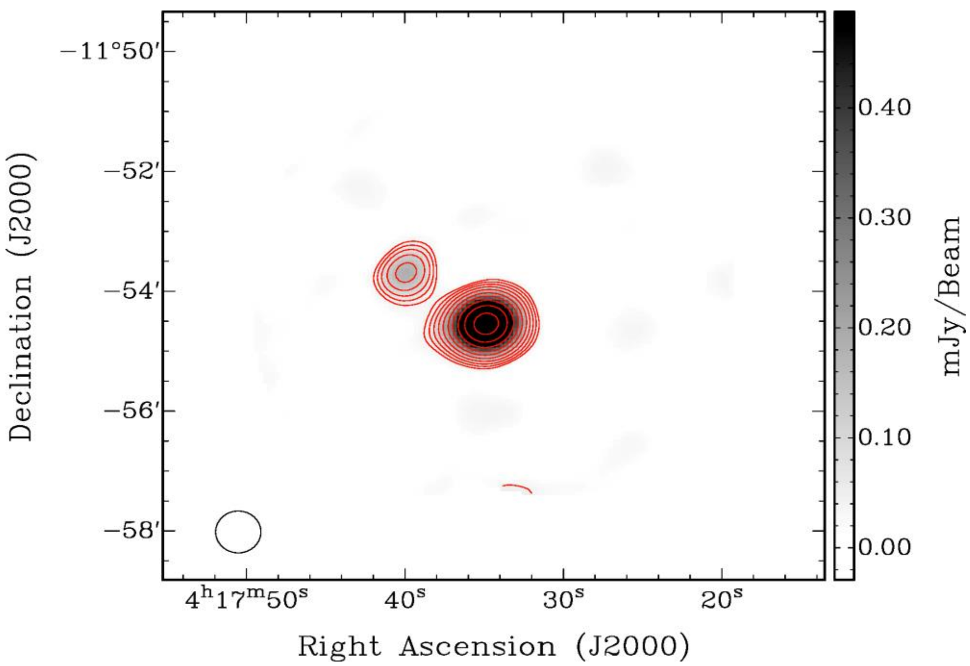

Figure 6.2. The ATCA radio image of the Galaxy cluster at 18 GHz. The resolution of this image is 42″ with rms noise of 8µJy/beam. The contours start at 5 and increase by factors of √2.

6.2.2 18 GHZ ATCA DATA

MACSJ0417.5−1154 was observed for 8 hours from ATCA (Australia Telescope Compact Array) with the H75 array, the most compact array configuration, and the upgraded Compact Array Broadband Backend (CABB; Wilson et al. 2011). Observations were done in full stokes mode with 2048 channels of width 1 MHz with central frequencies of the two bands at 17 and 19 GHz. Bad data were searched and excised. Both bands were calibrated separately using 1934−638 as primary/amplitude calibrator and 0403−132 as secondary/phase calibrator. Data reduction was done using the package Multichannel Image Reconstruction, Image Analysis and Display (MIRIAD). Standard calibration method was followed in calibrating primary and secondary calibrators, followed by the application of the calibration tables on the target data. After averaging visibilities over a 5-minute interval, data having in excess of 4 times the standard deviation in amplitude were excised to get rid of any remaining interference. Calibrated data of both band centered at 17 and 19 GHz were taken to make a combined image. MIRIAD task 'invert' was used to transform mosaicked visibility data into a map followed by 'mossdi' to perform a steer CLEAN on the mosaicked image. To restore the clean component to make the CLEAN map task 'restor' was used. The image (Fig. 6.2) was convolved with 42″ beam to highlight large-scale diffuse emission. Stokes-V does not contain signal and was therefore used to estimate the rms noise in the image which was found to be 8 μJy/beam.

6.2.3 DIFFUSE EMISSION ESTIMATION AT 1.387 GHZ AND 18 GHZ AND ANALYSIS

To estimate the amount of diffuse emission present in the halo region in both 1.387 and 18 GHz frequencies we have used the approach taken by Parekh et al. (2017), and subsequently by Sandhu et al. (2018). First, we estimated the total flux in the central region of the cluster at the two frequencies. Then, images were made with the best resolution at the two frequencies (2″) – from these images, the integrated flux densities of the two point sources were estimated, using Gaussian fitting. Finally, the integrated fluxes of the two point sources were subtracted from the total integrated flux of the central region, at both the frequencies. The above method makes no assumption about the spectral index of the point sources, or the diffuse emission, and has ensured the use of high-resolution data from the same observation.

The integrated flux densities of the radio halo region of MACSJ0417.5−1154 at different frequencies are listed in Table 6.2. The spectrum of the radio halo region is presented in Fig. 6.3. We have used different combinations of data points to derive spectral indices at several parts of the total bandwidth 150 MHz and 18 GHz, as given below (see Table 6.2 for source of the data points).

(i) between 610 MHz and 18 GHz

– using d,e,f,g,h,i : $\alpha = -1.79^{+0.09}_{-0.12}$

– using d,f,g,h,i : $\alpha = -1.87^{+0.10}_{-0.12}$

– using d,e,g,h,i : $\alpha = -1.77^{+0.09}_{-0.12}$

(ii) between 150 MHz and 610 MHz

– using a, b, d : $\alpha = -1.04^{+0.35}_{-0.26}$

(iii) between 150 MHz and 18 GHz

– using a, b, d, e, f g, h, i : $\alpha = -1.61$ +/- 0.12

– using a, b, d, f, g, h, i : $\alpha = -1.61$ +/- 0.11

– using a, b, d, e, g, h, i : $\alpha = -1.61$ +/- 0.11

6.3 DISCUSSION AND SUMMARY

We have presented radio observations of the galaxy cluster MACS J0417.5-1154 at 1.387 and 18 GHz (obtained using GMRT and ATCA respectively), and the spectrum of diffuse emission in the central region of the cluster, from 0.235 to 18 GHz. This is a very massive and the second most X-ray luminous cluster in the MACSurvey (Ebeling et al. 2010) with one of the flattest radio spectra in the frequency range 235 to 610 MHz with spectral index □ = −0.38 (Parekh et al. 2017), followed by a very steep spectrum in the frequency range 0.610 to 18 GHz. We have presented here two spectral index fitting and a single spectral index fit for the entire radio data available.

Our observations reconfirm the radio-quiet nature of this cluster at frequencies higher than 610 MHz. However, our discovery of diffuse emission in the central

Table 6.2 INTEGRATED FLUX DENSITY OF THE RADIO HALO REGION

Label	Frequency (GHz)	Flux density (mJy)	Source
a	0.150	250 ± 90	Sandhu et al. (2018)∘
b	0.235	108 ± 10	Sandhu et al. (2018)*
c	0.235	77 ± 8	Parekh et al. (2017)
d	0.610	50 ± 5.5	Parekh et al. (2017)
e	1.387	6.51 ± 1.1	Current Work
f	1.575	10.6 ± 1	Parekh et al. (2017)
g	5.5	1.23 ± 0.11	Sandhu et al. (2018)
h	9.0	0.51 ± 0.11	Sandhu et al. (2018)
i	18.0	0.08 ± 0.03	Current Work

∘ *GLEAM data at 150 MHz was used, and TGSS data was used to subtract point sources at 150 MHz*
* *GLEAM data at 235 MHz was used.*

region of this cluster at 18 GHz provides another puzzle for this peculiar cluster. The north-west elongation in the diffuse emission at 18 GHz is missing, as in the 9 GHz data in Sandhu et al. (2018). Interestingly, our 1.387 and 18 GHz data ensure that the spectral index between 0.61 and 18 GHz matches with the estimates provided in Parekh et al. (2017) and Sandhu et al. (2018), i.e. the previous chapter.

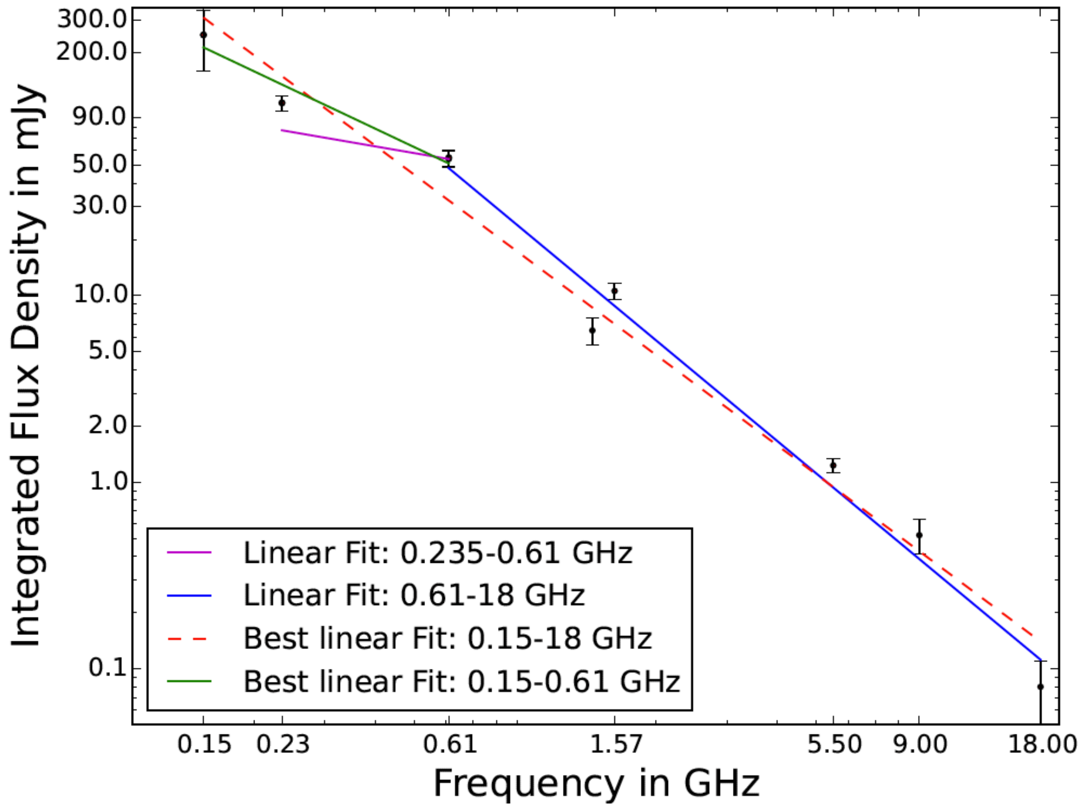

Figure 6.3. The spectrum of diffuse emission in MACSJ0417.5-1154. Different linear fits are shown here for data ranging from 150 MHz to 18 GHz. The best single line fit spectral index is _ = −1.61 Å} 0.12, shown here as a dotted red line. 150 MHz and 235 MHz data are taken from the GLEAM survey, and are really upper limits to the diffuse emission. The magenta line from 235 MHz to 610 MHz is the spectrum, considering only the previously published value of diffuse emission at 235 MHz, which is likely underestimated (see Sandhu et al. 2018 for details).

We found non-trivial structure of the point sources embedded in the halo region. Therefore, it is not clear how much contribution these point sources make in the diffuse emission estimation, and simple Gaussian fitting of these point sources may not provide reliable estimates of diffuse emission. High resolution images are needed at several radio frequencies for better understanding of these sources, in order to obtain better estimates of diffuse emission. We point out the fact that our estimation of point-source fluxes is more accurate, due to the high-resolution data available at 1.387 and 18 GHz in the current work, and 5.5 and 9 GHz in earlier work (Sandhu et al. 2018).

The sharp fall in the spectrum is not well understood yet. According to Parekh et al. 2017, ∼ 1 Gyr has passed since merger and turbulence has decayed and due to less efficient re-acceleration the kink in the spectrum has shifted to < 1 GHz frequency. Brown et al. 2011 discuss two scenarios for clusters with subluminous diffuse emission at GHz frequencies. They state that high LX and disturbed X-ray morphology clusters can exist in an 'off' state; these clusters may exhibit some Mpc-scale diffuse emission at low radio frequencies (i.e. below 1.4 GHz), but at GHz frequencies are sub-luminous. For such clusters, one scenario according to Brown et al. is that the cluster merger with which the diffuse emission is associated may be less energetic – this can give rise to extremely steep spectra of diffuse emission. In the other scenario, cosmic ray (CR) protons and their secondary products CR electrons are re-accelerated by MHD turbulence, and synchrotron emission scales with turbulence – in such systems, radio halos gradually gain luminosity with time, as the ICM becomes increasingly turbulent. It is not clear with the current data whether either of these scenarios is possible/feasible for MACS J0417.5−1154.

A third possibility, also mentioned by Brown et al. (2011), is that of a non-thermal population of electrons in the cluster core due to the presence of radio galaxies / AGNs and their jets. This is relevant in the present case, since sources in the central regions of this cluster exhibit non-trivial structure, which may well be parts of radio galaxy jets. It is possible that a portion of the diffuse emission in the central region of this cluster is due to turbulent re-acceleration of this non-thermal plasma.

A recent study by Sandhu et al. (2018) of this cluster has pointed out the possibility of the diffuse emission being underestimated at 235 MHz – this implies that the spectral cutoff may not be as sharp as it seems, as pointed out by them. In that case, the spectral cutoff or turnover may not occur, i.e. the data may be consistent with a single spectral index. This fact makes way for yet another interpretation of the merger age to be recent. Hence, there is no break in the spectrum. Here, we have tried to investigate whether there is a higher frequency cut-off in the spectrum. We used our 18 GHz observations on the same cluster to do the same. But we could not find any evidence of such a break.

Skillman et al. (2013) have pointed out that peak X-ray emission precedes peak radio emission by 0.2–0.5 Gyr. In addition, absence of any radio relic also points out to the lack of radio emission in the cluster. The combination of these two facts points to the cluster merger being recent, which is exactly the conclusion we reached above. Thus, the lack of radio emission in this cluster is consistent with the merger being too recent to be detectable in radio.

In conclusion, we have presented the spectrum of the diffuse emission in the cluster MACS J0417.5−1154 from 0.235 to 18 GHz, i.e. over a large frequency range. Though this cluster appears to be a recent merger event, it exhibits a spectral cutoff or break at a low frequency (0.61 GHz). We have speculated the reasons for this behaviour, and presented a few scenarios that would cause such a low-frequency cutoff. We have also presented an explanation for the lack of radio emission in this merger.

CHAPTER 7

CONCLUSIONS AND SCOPE FOR FUTURE WORK

In this thesis, we have presented our study of diffuse emission from two clusters:

(a) Bullet cluster – 5.5 and 9.0 GHz
(b) MACS J0417.5-1154 – 150, 235, 610 MHz; 1.387, 5.5, 9.0 and 18 GHz

Both clusters are hot (T_X > 10 keV), extremely X-ray luminous, very massive (M > 10^{15} M_{sun}), and have disturbed X-ray luminosity contours. In the case of the Bullet cluster, the X-ray contours are clearly non-concentric, and show two obvious concentrations of matter, corresponding to the two sub-clusters, or the two merging clusters – these sub-clusters are separated in the E-W direction. Both the galaxy clusters are relatively young, in that << 1 Giga-years have passed since the merger event (Skillman et al. 2012).

While the Bullet cluster has diffuse emission in the form of both radio relics at the periphery as well as a radio halo in the central region, MACS J0417.5-1154 has diffuse emission only in the central region, i.e. a radio halo.

Radio observations of the Bullet cluster have revealed two radio relics, corresponding to two shock fronts (Shimwell et al. 2015) in X-ray data – these radio relics are situated on the eastern edge of the cluster. These radio relics were studied in the frequency ranges 1.1-3.1 GHz by Shimwell et al. (2015).

We examined these radio relics in the frequency ranges 4.5-6.5 GHz and 8-10 GHz using data from the ATCA, and found that the spectrum of these radio relics has a break at about 5 GHz. Similar breaks in the spectrum of diffuse emission have been found, albeit at significantly lower frequencies (Brunetti et al. 2008).

This feature in the spectrum is consistent with the expectation that a non-thermal population of electrons that loses energy only through synchrotron radiation would develop a break in the spectrum. It is expected that as the non-thermal plasma ages, this break in the spectrum would move to lower frequencies (Blundell & Rawlings 2001). The fact that the break in the spectrum of the radio relics in the Bullet cluster occurs at high frequencies points to the cluster merger being relatively young.

In this context, and with this observation about the Bullet cluster relic break frequency, we observed yet another cluster merger – MACS J0417.5-1154 – with known diffuse emission at low frequencies, expecting to observe a break in the spectrum at relatively higher frequencies.

However, the diffuse emission at the centre of this merger has an extremely flat spectrum from 235 to 610 MHz, which then steepens greatly by a factor of more than three (3) – this extremely low cutoff or break frequency is consistent with a non-thermal plasma that has undergone aging, and consequently, the cutoff or break has shifted to lower frequencies due to synchrotron losses.

This presents a major problem in explaining the dynamical state and the spectrum of diffuse emission of the cluster MACS J0417.5-1154. X-ray data clearly shows extended contours, which, when combined with the large mass and high temperature of the ICM in the cluster, describes a cluster that is in the process of a merger, and where the merger process has begun not too long ago.

But, as described above, the age of the merger as deduced from the spectrum of diffuse emission in the central region contradicts this.

To reconcile these differences, we examined the properties of the diffuse emission at the centre of the cluster MACS J0417.5-1154 at frequencies ranging from 150 MHz to 18 GHz; specifically, at 150 MHz, 235 MHz, 610

MHz, 1.387 GHz, 1.575 GHz, 5.5 GHz, 9 GHz and 18 GHz. Of these, 5.5, 9 and 18 GHz data were taken from ATCA; 235, 610 and 1387 MHz data from GMRT; 1.575 GHz data from JVLA; 150 MHz data from the GLEAM and TGSS surveys, and 235 MHz data from GLEAM.

As can be seen from the figure in Parekh et al. (2017), the spectrum for this cluster is flattest between 235 MHz and 610 MHz (□□0.37), and steepens significantly at 610 MHz (□□1.72). In other words, the extremely flat portion of the spectrum of diffuse emission depends on the emission at one frequency – this is why, the diffuse emission at 235 MHz needs to be carefully examined.

This is why, we examined the diffuse emission at 235 MHz from an independent source – the GLEAM survey. With its 2 arcmin beam, the GLEAM survey is suited well to detect large-scale diffuse emission. We used the estimates of point sources in the diffuse emission region from Parekh et al. (2017), and estimated the net diffuse emission at 235 MHz. It turns out that the diffuse emission at 235 MHz has been underestimated by Parekh et al. (2017).

We also estimated the diffuse emission at 150 MHz using the GLEAM survey; we used data from the TGSS survey to estimate point source fluxes.

The increase in the estimate of diffuse emission at 235 MHz changes the spectral index up to 610 MHz, making it sharper, such that the change in spectral index at 610 MHz is much less significant. We showed, effectively, that it is possible to fit a single spectral index for the whole data, from 150 MHz up to 9 GHz.

At the same time, we examined the diffuse emission at 18 GHz, to figure out if there could be any steepening of the spectrum at this high frequency. However, no steepening was detected. Therefore, it was found to be possible to fit a single spectral index from 150 MHz to 18 GHz. This would be consistent with this cluster merger being young.

This change in the spectral index due to a correction in the estimate of diffuse emission at lower frequencies is therefore critical – it is possible that there exist other cases of merging clusters, for which underestimates at lower frequencies have led to apparent sharp breaks in the spectrum.

This thesis, therefore, points to the need for examining diffuse emission at low frequencies carefully, in order to extract information about the dynamics of cluster mergers, particularly their ages, properly.

APPENDIX

We therefore demonstrate a simple total power measurement at 21 cm of neutral hydrogen in the galaxy, as an example of the single-dish or single-element observations that need to be carried out in order to constrain the total power received from an extended object. We present the details of

i) Student/amateur friendly radio observational set-up for the detection of HI line (1420.62 MHz) in our Galactic Plane (RA: 17h 45m 10s, DEC: -29^{o} S), This also covers in-depth description of the observational set-up which includes the characterization of front-end and back-end receiving systems along with the calibration details. The equipment and the methodology mentioned herewith has the potency to monitor and continuously observe the galactic/extragalactic radio sources such as Cygnus, Cassiopeia to name a few and HI regions in our Galactic plane respectively. In this article we provided quantitative drift scan observations of HI regions of our Galactic Plane as it transits over the local meridian of Gauribidanur radio observatory (Latitude 13.6^{o} N, Longitude 77.525^{o} E).

ii) An analysis of observed data with the conclusions and possible plans for future improvements.

21 CM EXPERIMENT AS A PRECURSOR TO RADIO OBSERVATIONS

The neutral hydrogen line (1420.4 MHz) is very abundant in our universe. The hyperfine emission of this radio line is due to the change in the energy state of neutral hydrogen. The theoretical foundations of this emission and detectability was laid by Dutch physicist Van de Hulst. But until 1950, physicist Ewen under the guidance of Ed Purcell completed a radio receiver which successfully detected this 21 cm line. Using a home brew radio equipment (a horn aperture) with relatively inexpensive electronics, this line can be easily detectable in the comfort of one’s backyard. The front-end receiver is therefore a radio antenna, which would be wide enough to capture the radio emission efficiently.

The first real world microwave antenna was a cylindrical parabola developed by Heinrich R. Hertz in 1888. Hertz wrote, ``As soon as I had succeeded in proving that the action of an electric oscillation spreads out as a wave in space, I planned experiments with the object of concentrating this action and making it perceptible at greater distances by putting the primary conductor in the focal line of a large concave parabolic mirror."

In 1894, Sir Oliver Lodge first demonstrated wave-guide microwave transmission lines at London's Royal Institution. After three years at the University of Calcutta, Indian physicist J. C. Bose flared out the end of a wave-guide, demonstrating the horn aperture antenna. In 1897, Marconi employed wave-guide horn antenna to recover microwave communications over a four-mile path in a demonstration for the British post office. But, this promising antenna configuration was not applied till 1951 to the challenges of radio astronomy. In one of radio astronomy's landmark experiments, Harvard University graduate student Harold I. ``Doc" Ewen built a horn antenna, to first measure the 1420 MHz hyperfine transition line of interstellar hydrogen. His antenna was based on the design of the earlier work of University of California professor Samuel Silver at the MIT Radiation Laboratory, with its physical dimensions constrained by the size of the parapet in Harvard's Lyman laboratory where his receiver apparatus was installed.

A COST-EFFECTIVE SETUP FOR 21 CM DETECTION FROM THE GALAXY

With a motivation to observe the 21 cm line with less expenditure, we designed a home brew radio receiver. The complete block diagram of this receiver is shown in Figure 3.1.

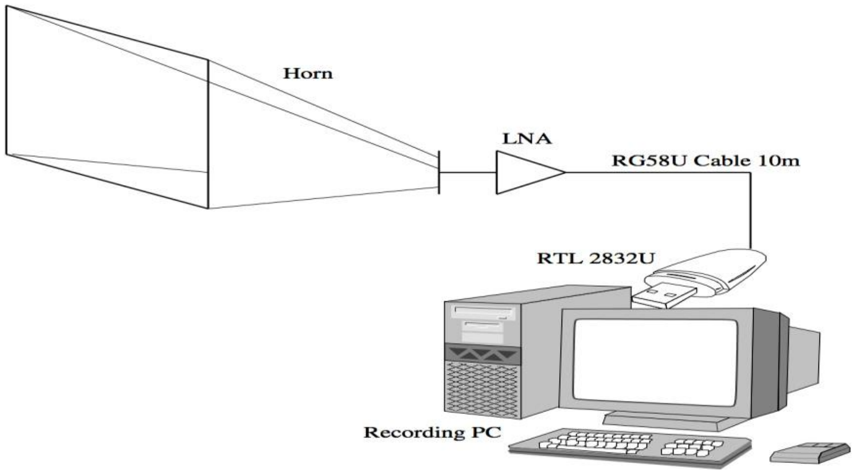

Figure 3.1: The experimental setup used for the 21 cm line detection

The front end of this receiver is a horn aperture antenna whose dimensions are 76" x 71". The horn antenna aperture and dimensions are chosen such that the maximum half power beam-width would be around 20^{o}; in-order to cover larger portions of Galactic Plane [4]. The sides of the horn are extended to a flaring angle of approx 55^{o} to i) maximize the collecting aperture as well as ii) the sensitivity. This horn antenna has a gain of approx 20 dB and VSWR < 2 in the frequency range 1420 -1421 MHz, serves primary receiving element.

This rectangular wave guide feed is constructed from an aluminium sheet (cross-section dimensions: 6.7" x 3.5") to detect the 21 cm emission line. The horn is fed by a Low Noise Amplifier of Gain approx 28 dB with Noise Figure of approx 0.5 dB. After amplification of 28 dB by a broadband amplifier (kept near the antenna base), the RF signal was later transmitted via a coaxial cable of length 10 m. Later the signal is fed to an RTL 2832U dongle controlled by a host computer under SDR (Software Defined Radio) environment. This dongle serves as the main back-end receiver. The required libraries (RTL-SDR) and necessary software is installed in the host computer.

RTL2832 SDR DONGLE

It is a popular, low cost hardware priced in the range of Rs. 3000/- that can be useful in numerous wireless/radio applications. The RTL-SDR dongle features the Realtek

RTL2832U chip, which provides I-Q samples through the USB interface. It can receive and demodulate various wireless signals across a broad frequency range. Thus, it is can be configured as a radio receiver under the SDR environment. The important specification of the dongle are:

- Tunable Bandwidth : 24 MHz-1700 MHz
- Instantaneous bandwidth: 3.2 MHz
- Antenna input impedance: 50 ohms
- ADC 8 bit resolution

The above described SDR satisfies our requirement and is therefore used for longer duration scans. The moderate cost of RTL-SDR and minimal hardware requirements is also one of the reasons to use it as a standalone spectral capturing device.

The raw I, Q samples from the dongle are Fourier transformed with fftw algorithm; by making use of a powerful script called{rtl_power_fftw}.
[https://github.com/AD-Vega/rtl-power-fftw/blob/master/doc/rtl_power_fftw.1.md].
This program is capable of continuous real-time data acquisition and processing on the fly. It uses the rtl-sdr library to access the RTL2832U device and the FFTW library to do the FFT processing. Data acquisition and Fast Fourier transform are done in separate program threads for maximum efficiency [ref]. The resulting power spectrum is written to the standard output. The power spectrum thus obtained can be helpful to perform several scientific studies. It can also averages a number of such spectra to gain a better signal-to-noise ratio. This script also offers to set several observing parameters with flexible file formats to acquire the data.

OBSERVATIONS

Prior to the start of observation the Local Sidereal time has to be noted. We carried the observations in drift scan mode. In this mode, the horn is pointed due South and pointed approximately to the declination of the Centre of Galactic plane, i.e.,
-28^{o} South. The antenna is fixed to this position throughout the observation. As the Galactic Plane transits the local meridian (Latitude 13^{o} N), the hydrogen line spectra is accumulated and saved to the PC.

CALIBRATION

The spectral power estimates of the observed data corresponds to a temperature given by

$$W = k\, T_A\, B \qquad (1)$$

where W is the received power spectral noise (Watts/Hz), k is Boltzmann constant, T_A is the antenna temperature, B is the observation bandwidth. The true estimate of the temperature from the observed data can be found by subtracting the observed temperature from the receiver noise temperature. It can be estimated by running several trail observations before the target source. In order to estimate the receiver noise temperature, an observational run with a short time is performed with a matched load (50 Ohms). Thus, the true antenna temperature is thus estimated this way.

To cover the observation for 8 hours of drift scan with reduced verbosity and writing to a binary file with text metafile, we used the rtl_power_fftw in the following syntax:

rtl_power_fftw -f 1420M:1421M -b 1024 -g 100 -e 8h -t 10s -q -m myscanfilename

here -f corresponds to the upper and lower limits of frequency in MHz,

-b corresponds to the number of FFT bins,

-g for setting the gain in RTL 2832 dongle,

-t for effective integration time,

-e for exit the acquisition at the pre-determined time.

We have done instrumental calibration for 10 seconds, followed by detailed observational scans for 8 hours. Later the data is processed in Octave to interpret the results.

RESULTS AND DISCUSSION

The 8 hours observational data is analysed and plotted as power spectrum as shown in Figure 3.2. The neutral hydrogen line is clearly visible from this spectrum.

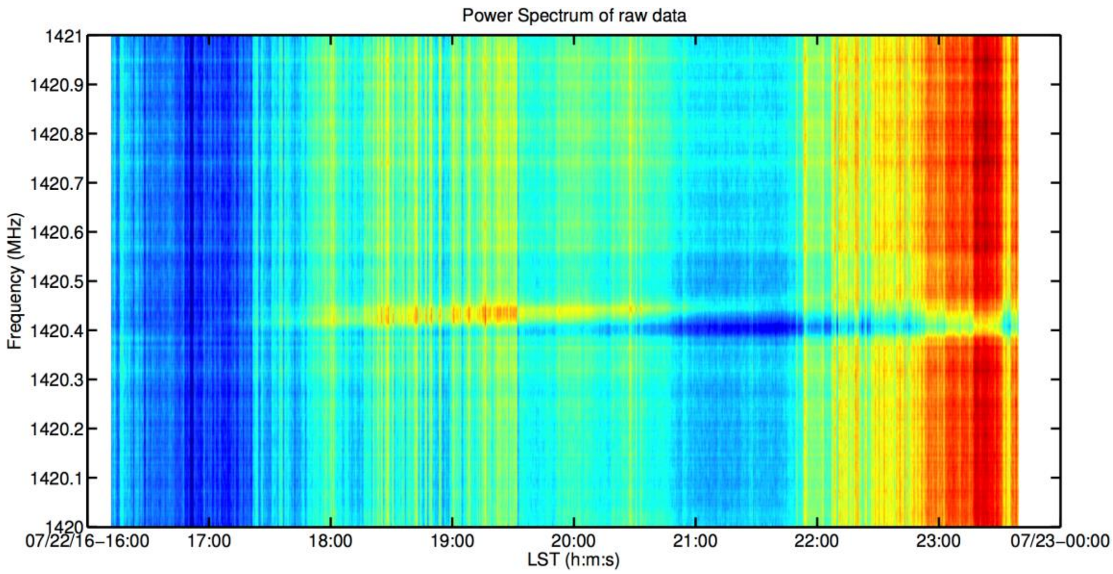

Figure 3.2: The HI line power spectrum of 8 hours data

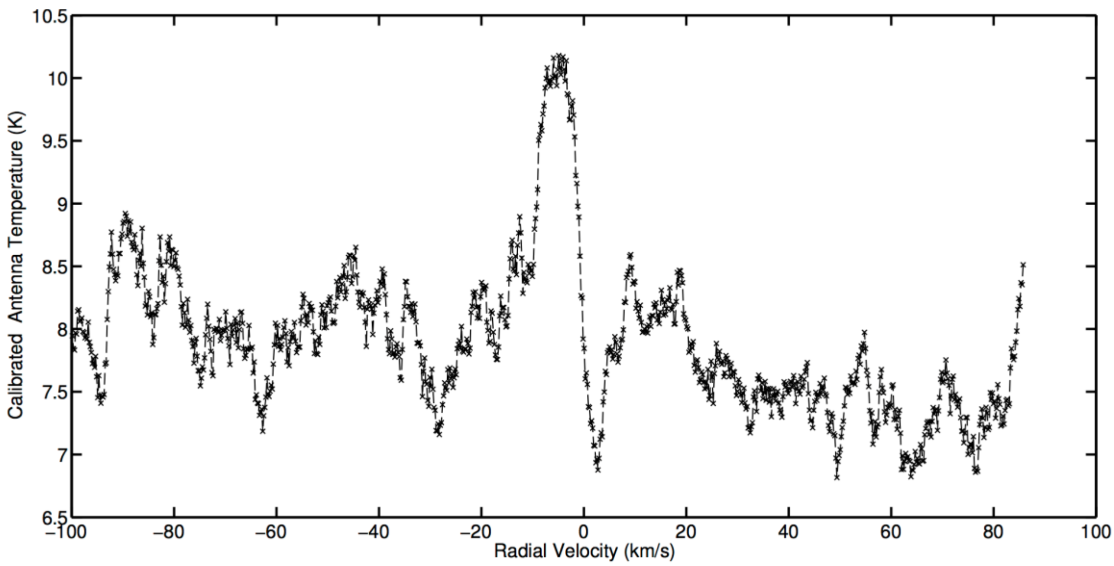

Figure 3.3: shows the typical hydrogen line calibrated to the antenna temperature (K). This line velocity is observed at approx 18.74 LST.

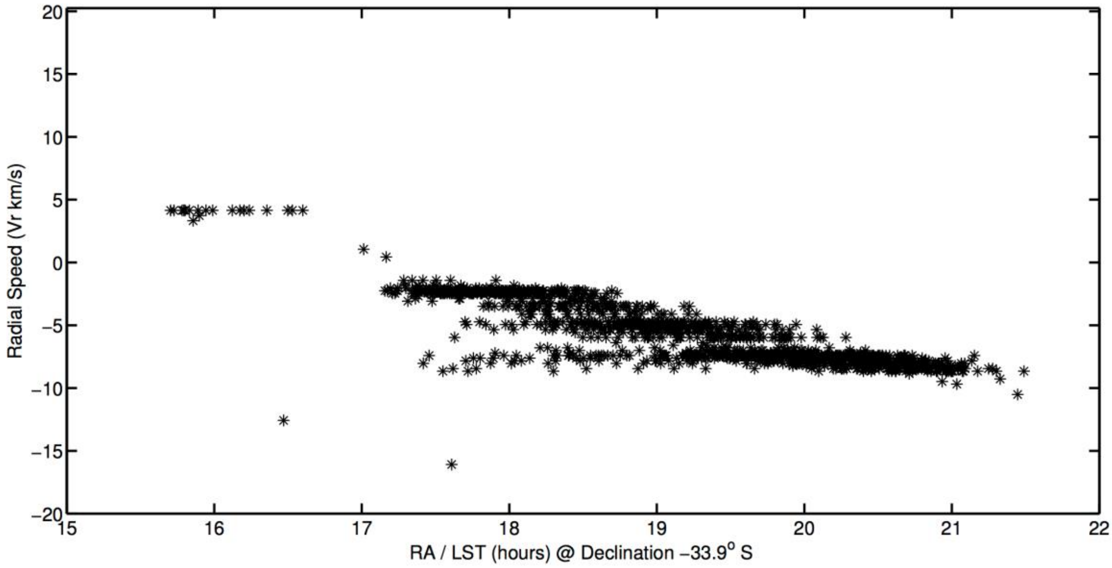

Figure 3.4: A plot of radial velocity at various RAs

The radial speed has been calculated at each and every RA/LST interval and plotted as shown in figure 4. We thus therefore presented the details of radio receiver and summarized the results. The preliminary results are found to be satisfactory but the observations has to be rigorously carried for obtaining the useful results.

FUTURE SCOPE

We summarize the improvements to this existing setup and observation methods to improve the results using cardboard Horn antenna :

- Improvements in the card board antenna to cope up with rotations in altitude and azimuth angles.
- To plot the rotation curve, observational at different galactic declinations are needed which is planned as extension to this observations.
- Finally, this project can make into progress for building a two-element interferometer for follow-up studies.

REFERENCES

[1] Brunetti, G., Jones, T.W.: Int. J. Mod. Phys. D 23, 30007 (2014). arXiv:1401.7519. doi:10.1142/S0218271814300079

[2] Clowe, D., Bradaˇc, M., Gonzalez, A.H., Markevitch, M., Randall, S.W., Jones, C., Zaritsky, D.: Astrophys. J. Lett. 648, 109 (2006). arXiv:astro-ph/0608407. doi:10.1086/508162

[3] Datta, A., Schenck, D.E., Burns, J.O., Skillman, S.W., Hallman, E.J.: Astrophys. J. 793, 80 (2014). arXiv:1408.5123. doi:10.1088/0004-637X/793/2/80

[4] Drury, L.O.: Rep. Prog. Phys. 46, 973 (1983). doi:10.1088/0034-4885/46/8/002

[5] Ensslin, T.A., Biermann, P.L., Klein, U., Kohle, S.: Astron. Astrophys. 332, 395 (1998). arXiv:astro-ph/9712293

[6] Feretti, L., Giovannini, G., Govoni, F., Murgia, M.: Astron. Astrophys. Rev. 20, 54 (2012). arXiv:1205.1919. doi:10.1007/s00159-012-0054-z

[7] Fujita, Y., Takizawa, M., Yamazaki, R., Akamatsu, H., Ohno, H.: Astrophys. J. 815, 116 (2015). arXiv:1511.01897. doi:10.1088/0004-637X/815/2/116

[8] Halverson, N.W., Lanting, T., Ade, P.A.R., Basu, K., Bender, A.N., Benson, B.A., Bertoldi, F., Cho, H., Chon, G., Clarke, J., Dobbs, M., Ferrusca, D., Güsten, R., Holzapfel, W.L., Kovács, A., Kennedy, J., Kermish, Z., Kneissl, R., Lee, A.T., Lueker, M., Mehl, J., Menten, K.M., Muders, D., Nord, M., Pacaud, F., Plagge, T., Reichardt, C., Richards, P.L., Schaaf, R., Schilke, P., Schuller, F., Schwan, D., Spieler, H., Tucker, C., Weiss, A., Zahn, O.: Astrophys. J. 701, 42 (2009). arXiv:0807.4208. doi:10.1088/0004-637X/701/1/42

[9] Kang, H.: J. Korean Astron. Soc. 48, 9 (2015). arXiv:1411.7513. doi:10.5303/JKAS.2015.48.1.9

[10] Kang, H.: ArXiv e-prints (2016). arXiv:1603.07444

[11] Kang, H., Ryu, D.: Astrophys. J. 809(2), 186 (2015)

[12] Kang, H., Ryu, D.: Astrophys. J. 823(1), 13 (2016)

[13] Liang, H., Hunstead, R.W., Birkinshaw,M., Andreani, P.: Astrophys. J. 544, 686 (2000). arXiv:astro-ph/0006072. doi:10.1086/317223

[14] Malu, S.S., Subrahmanyan, R.: J. Astrophys. Astron. 32, 541 (2011). doi:10.1007/s12036-011-9111-7

[15] Malu, S.S., Subrahmanyan, R., Wieringa, M., Narasimha, D.: ArXiv e-prints (2010). arXiv:1005.1394

[16] Owers, M.S., Nulsen, P.E.J., Couch, W.J., Markevitch, M.: Astrophys. J. 704, 1349 (2009). arXiv:0909.2645. doi:10.1088/0004-637X/704/2/1349

[17] Plagge, T., Benson, B.A., Ade, P.A.R., Aird, K.A., Bleem, L.E., Carlstrom, J.E., Chang, C.L., Cho, H.-M., Crawford, T.M., Crites, A.T., de Haan, T., Dobbs, M.A., George, E.M., Hall, N.R., Halverson, N.W., Holder, G.P., Holzapfel, W.L., Hrubes, J.D., Joy, M., Keisler, R., Knox, L., Lee, A.T., Leitch, E.M., Lueker, M., Marrone, D., McMahon, J.J., Mehl, J., Meyer, S.S., Mohr, J.J., Montroy, T.E., Padin, S., Pryke, C., Reichardt, C.L., Ruhl, J.E., Schaffer, K.K., Shaw, L., Shirokoff, E., Spieler, H.G., Stalder, B., Staniszewski, Z., Stark, A.A., Vanderlinde, K., Vieira, J.D., Williamson, R., Zahn, O.: Astrophys. J. 716, 1118 (2010). arXiv:0911.2444. doi:10.1088/0004-637X/716/2/1118

[18] Reynolds, J.E.: A revised flux scale for the at compact array. Technical Report 39.3/040, ATNF Technical Document Series (1994). http://www.atnf.csiro.au/observers/memos/

[19] Sarazin, C.L.: X-ray Emission from Clusters of Galaxies (1988)

[20] Sault, R.J., Staveley-Smith, L., Brouw, W.N.: Astron. Astrophys. Suppl. Ser. 120, 375 (1996)

[21] Sault, R.J.: ATCA flux density scale at 12 mm. Technical Report 39.3/124, ATNF Technical Document Series (2003). http://www.atnf.csiro.au/observers/memos/

[22] Shimwell, T.W., Brown, S., Feain, I.J., Feretti, L., Gaensler, B.M., Lage, C.: Deep radio observations of the radio halo of the bullet cluster 1e 0657-55.8 (2014). doi:10.1093/mnras/stu467

[23] Shimwell, T.W., Markevitch, M., Brown, S., Feretti, L., Gaensler, B.M., Johnston-Hollitt, M., Lage, C., Srinivasan, R.: Another shock for the bullet cluster, and the source of seed electrons for radio relics (2015). arXiv:1502.01064. doi:10.1093/mnras/stv334

[24] Intema, H.T., Jagannathan, P., Mooley, K.P., Frail, D.A.: Astron. Astrophys. 598, 78 (2017). https://doi.org/10.1051/0004-6361/201628536. arXiv:1603.04368

[25] Malu, S., Datta, A., Sandhu, P.: Astrophys. Space Sci. 361, 255 (2016). https://doi.org/10.1007/s10509-016-2844-7. arXiv:1606.08700

[26] Molnar, S.: Front. Astron. Space Sci. 2, 7 (2015). https://doi.org/10.3389/fspas.2015.00007

[27] Parekh, V., Dwarakanath, K.S., Kale, R., Intema, H.: Mon. Not. R. Astron. Soc. 464, 2752 (2017). https://doi.org/10.1093/mnras/stw2521. arXiv:1608.02796

[28] Perley, R.A., Chandler, C.J., Butler, B.J., Wrobel, J.M.: Astrophys. J. Lett. 739, 1 (2011). https://doi.org/10.1088/2041-8205/739/1/L1. arXiv:1106.0532

[29] Sault, R.J., Teuben, P.J., Wright, M.C.H.: In: Shaw, R.A., Payne, H.E., Hayes, J.J.E. (eds.) Astronomical Data Analysis Software and Systems IV. Astronomical Society of the Pacific Conference Series, vol. 77, p. 433 (1995). arXiv:astro-ph/0612759

[30] Sault, R.J., Teuben, P.J.,Wright, M.C.H.: MIRIAD: Multi-channel Image Reconstruction, Image Analysis, and Display. Astrophysics Source Code Library (2011). http://ascl.net/1106.007

[31] Stroe, A., Rumsey, C., Harwood, J.J., van Weeren, R.J., Röttgering, H.J.A., Saunders, R.D.E., Sobral, D., Perrott, Y.C., Schammel, M.P.: Mon. Not. R. Astron. Soc. 441, 41 (2014). https://doi.org/10.1093/mnrasl/slu045. arXiv:1403.4255

[32] Wayth, R.B., Lenc, E., Bell, M.E., Callingham, J.R., Dwarakanath, K.S., Franzen, T.M.O., For, B.-Q., Gaensler, B., Hancock, P., Hindson, L., Hurley-Walker, N., Jackson, C.A., Johnston-Hollitt, M., Kapi´nska, A.D., McKinley, B., Morgan, J., Offringa, A.R., Procopio, P., Staveley-Smith, L., Wu, C., Zheng, Q., Trott, C.M., Bernardi, G., Bowman, J.D., Briggs, F., Cappallo, R.J., Corey, B.E., Deshpande, A.A., Emrich, D., Goeke, R., Greenhill, L.J., Hazelton, B.J., Kaplan, D.L., Kasper, J.C., Kratzenberg, E., Lonsdale, C.J., Lynch, M.J.,McWhirter, S.R., Mitchell, D.A., Morales, M.F., Morgan, E., Oberoi, D., Ord, S.M., Prabu, T., Rogers, A.E.E., Roshi, A., Shankar,

N.U., Srivani, K.S., Subrahmanyan, R., Tingay, S.J., Waterson, M., Webster, R.L., Whitney, A.R., Williams, A., Williams, C.L.: Proc. Astron. Soc. Aust. 32, 025 (2015). https://doi.org/10.1017/pasa.2015.26. arXiv:1505.06041

[33] Wilson, W.E., Ferris, R.H., Axtens, P., Brown, A., Davis, E., Hampson, G., Leach, M., Roberts, P., Saunders, S., Koribalski, B.S., Caswell, J.L., Lenc, E., Stevens, J., Voronkov, M.A., Wieringa, M.H., Brooks, K., Edwards, P.G., Ekers, R.D., Emonts, B., Hindson, L., Johnston, S., Maddison, S.T., Mahony, E.K., Malu, S.S., Massardi, M., Mao, M.Y., McConnell, D., Norris, R.P., Schnitzeler, D., Subrahmanyan, R., Urquhart, J.S., Thompson, M.A., Wark, R.M.: Mon. Not. R. Astron. Soc. 416, 832 (2011). https://doi.org/10.1111/j.1365-2966.2011.19054.x .arXiv:1105.3532

[34] Applegate, D.E., von der Linden, A., Kelly, P.L., Allen, M.T., Allen, S.W., Burchat, P.R., Burke, D.L., Ebeling, H., Mantz, A., Morris, R.G.: Mon. Not. R. Astron. Soc. 439, 48 (2014). https://doi.org/10.1093/mnras/stt2129. arXiv:1208.0605

[35] Brunetti, G., Jones, T.W.: Int. J. Mod. Phys. D 23, 30007 (2014). https://doi.org/10.1142/S0218271814300079. arXiv:1401.7519

[36] Brunetti, G., Giacintucci, S., Cassano, R., Lane, W., Dallacasa, D., Venturi, T., Kassim, N., Setti, G., Cotton, W., Markevitch, M.: Nature 455(7215), 944 (2008)

[37] Dwarakanath, K.S., Malu, S., Kale, R.: J. Astrophys. Astron. 32, 529 (2011). https://doi.org/10.1007/s12036-011-9109-1

[38] Ebeling, H., Edge, A.C., Mantz, A., Barrett, E., Henry, J.P., Ma, C.J., van Speybroeck, L.: Mon. Not. R. Astron. Soc. 407, 83 (2010). https://doi.org/10.1111/j.1365-2966.2010.16920.x. arXiv:1004.4683

[39] Brown S., Emerick A., Rudnick L., Brunetti G., 2011, ApJ, 740, L28